To the Graduate Council:

I am submitting herewith a thesis written by Michael Thomas Lugten entitled "An Experimental Investigation of the Jet Damping Effects of a Solid Rocket Motor." I have examined the final copy of this thesis for form and content and recommend that it be accepted in partial fulfillment of the requirements for the degree of Master of Science, with a major in Aerospace engineering.

Dr. Gary Flandro, Major Professor

We have read this thesis
and recommend its acceptance:

Accepted for the Council:

Associate Vice Chancellor
and Dean of The Graduate School

STATEMENT OF PERMISSION TO USE

In presenting this thesis in partial fulfillment of the requirements for a Master's degree at The University of Tennessee, Knoxville, I agree that the Library shall make it available to borrowers under rules of the Library. Brief quotations from this thesis are allowable without special permission, provided that accurate acknowledgment of the source is made.

Permission for extensive quotation from or reproduction of this thesis may be granted by my major professor, or in his absence, by the Head of Interlibrary Services when, in the opinion of either, the proposed use of the material is for scholarly purposes. Any copying or use of the material in this thesis for financial gain shall not be allowed without my written permission.

Signature Michael Layton

Date 7-28-93

AN EXPERIMENTAL INVESTIGATION OF THE JET DAMPING EFFECTS OF A SOLID ROCKET MOTOR

A Thesis

Presented for the

Master of Science

Degree

The University of Tennessee, Knoxville

Michael Thomas Lugten

August 1993

ACKNOWLEDGMENTS

I would like to thank my advisor, Dr. Gary Flandro, for his guidance and encouragement over the past two years. I would also like to thank Dr. Roger Crawford and Dr. Robert Roach for being on my thesis committee. I wish to express special appreciation to Jim Goodman for his valuable assistance in constructing the test apparatus. Ram Sivakumaran provided the theoretical results in this thesis. Finally, I would like to thank all the faculty, staff and fellow students who have made the last two years enjoyable.

ABSTRACT

The purpose of this experiment was to investigate the interaction between the combustion gases of laboratory scale (2.0 inch diameter) solid rocket motors and the rocket motor dynamics. Under normal conditions, this interaction leads to a decrease of a vehicle's lateral angular velocity. This is known as jet damping. But in larger, spin stabilized solid rocket motors, such as the STAR 48 family of motors, the lateral oscillations grow during the motor burn. This phenomenon is known as "coning" or "nutation" of the spacecraft. An experimental apparatus was designed and built to measure the magnitude and direction of the side force generated in small rocket motors. This test stand spins the rocket motor about two axes. One electric motor spins the rocket motor about its longitudinal axis, which simulates the spin of spin stabilized vehicles. The other electric motor spins the rocket about a transverse axis. Strain gages mounted on flexures measure the side force produced by the rocket motor during the motor burn. Both aluminized and nonaluminized rocket motors are utilized to investigate the effects of the accumulation of aluminum oxide slag in the combustion chamber. To date only one rocket motor has been fired, resulting in some damage to the hardware as a result of an O-ring failure. Testing is expected to continue when new parts are made. This test stand promises to provide useful results in the investigation of jet damping and jet driving phenomenon.

TABLE OF CONTENTS

LIST OF FIGURES

I. INTRODUCTION

From the earliest days of modern rocketry it has been known that the flow of combustion gases through the motor chamber and nozzle has a significant effect on the lateral dynamics of the vehicle. This interaction between the gases and the vehicle motion is known as jet damping or thrust damping. It is considered a damping effect because under normal conditions it leads to a decay of any wobbling of the vehicle axis of symmetry from the flight path.

Since it is usually important to accurately know the forces and moments a vehicle is subject to, there is a need to fully understand the interaction between the operation of the rocket motor and the vehicle dynamics. In a rocket operating in the atmosphere, aerodynamic moments are usually more important than jet damping moments; but in a vacuum, jet damping becomes an important torque acting on the vehicle.

In order to predict the magnitude of the jet damping torque, an acceptable analytical model must be acquired that can be applied to various vehicle configurations. Unfortunately, the classical jet damping models are oversimplified and can only be applied to specific motor sizes and shapes. There has been some work in recent years to numerically model the motor internal flow and vehicle interaction, but there has been virtually no experimental research to help verify these models. The purpose of this research is to better understand the interaction between the internal gas flow in the rocket motor and the vehicle dynamics through experimental means.

Classical jet damping theory is less applicable when the size of the rocket motor increases. In fact, the damping effect may become a driving one. Instead of reducing lateral oscillations, the moment generated by the motor about the vehicle center of mass causes the wobbling to grow. This wobbling instability has been commonly referred to as "coning" or "nutation" of the spacecraft. Coning can be visualized by looking at the flight of a football. A wobbling football exhibits a large coning motion, whereas a tight spiral has little coning motion. This phenomenon has appeared in the PAM-D series of spin stabilized upper stage vehicles and has been linked to the operation of the solid rocket motor.

PAM is the acronym for the McDonnell Douglas Payload Assist Module. This module consists of a solid propellant rocket motor, the structure needed to attach a payload and a spin table/separation module. PAM-D upper stage vehicles are used to carry a variety of communication satellites to geosynchronous orbit. They utilize a solid propellant rocket motor of the STAR 48 family manufactured by Thiokol Corporation, Elkton Division, although both smaller and larger motors may be used. These vehicles are spun at between 40 and 80 rpm. Spin stabilization eliminates the need for a gimballed nozzle for trajectory control and minimizes the effects of thrust misalignment or principal axis misalignment. The spacecraft are rotated on a spin table to the desired rpm and are then ejected from the carrier stage, such as the Space Shuttle, by a set of springs. When it is separated from the spin table there is some slight wobble of the vehicle, this is called the tip-off wobble.

The nutation instability was not evident when smaller STAR 37 motors were used. As payload mass increased, the size of the motor increased to the STAR 48 family of motors. Spin stabilized vehicles using the STAR 48 or the larger STAR 63 motors experienced the coning instability. Figures and specifications on these motors can be found in Appendix A. This data was taken from the Thiokol Space Motor Catalog [1]. Since all the spacecraft configurations were essentially the same, this suggests that the size of the motor has something to do with the instability. There is considerable evidence that this nutation phenomenon appears only in spin stabilized vehicles since there has been numerous flights of large solid propelled vehicles that are three-axis attitude controlled in which no wobbling tendencies have been observed during motor operation.

The unexpected wobbling instability in the STAR 48 and larger STAR 63 motors appears during the final half of the motor burn with a growth rate that increases rapidly during the final few seconds of the motor operation. The motion can be described as a growing oscillation of the pitch and yaw angular rates as shown in Figure 1 from reference [2]. During the first part of the motor burn, initial tip-off wobble is reduced as expected according to classical jet damping analysis, but then something unexpected happens and the wobble begins to increase rapidly until the motor burns out, at which time the growth either ceases or abruptly decreases. Figure 2 adapted from reference [2] shows the development of the coning instability. The final cone angle, θ, has averaged about 10 degrees and has reached values as high as 17 degrees. It has been the common approach of designers to use a strap-on attitude control system to counteract the disturbing torques that cause the coning to grow. This approach is costly and it reduces the available payload of the spacecraft.

The exact source of this instability has yet to be uncovered, but most researchers seem to agree that the underlying physical mechanism is either a slag sloshing effect or a gas dynamic effect. These two mechanisms are what remain from an original list of about 20 potential sources of the instability. The slag sloshing model assumes that molten aluminum oxide produced in the combustion process accumulates around the nozzle during motor burn in a liquid pool and sloshes in response to the wobbling spacecraft. When this pool is in resonance with the wobble it can drive the oscillation to increase. The gas dynamic effect is a variation of the jet damping effect in which unsymmetrical internal pressure forces produce a torque about the vehicle center of mass which acts to amplify rather than decrease vehicle wobble. Figure 3 taken from [3]

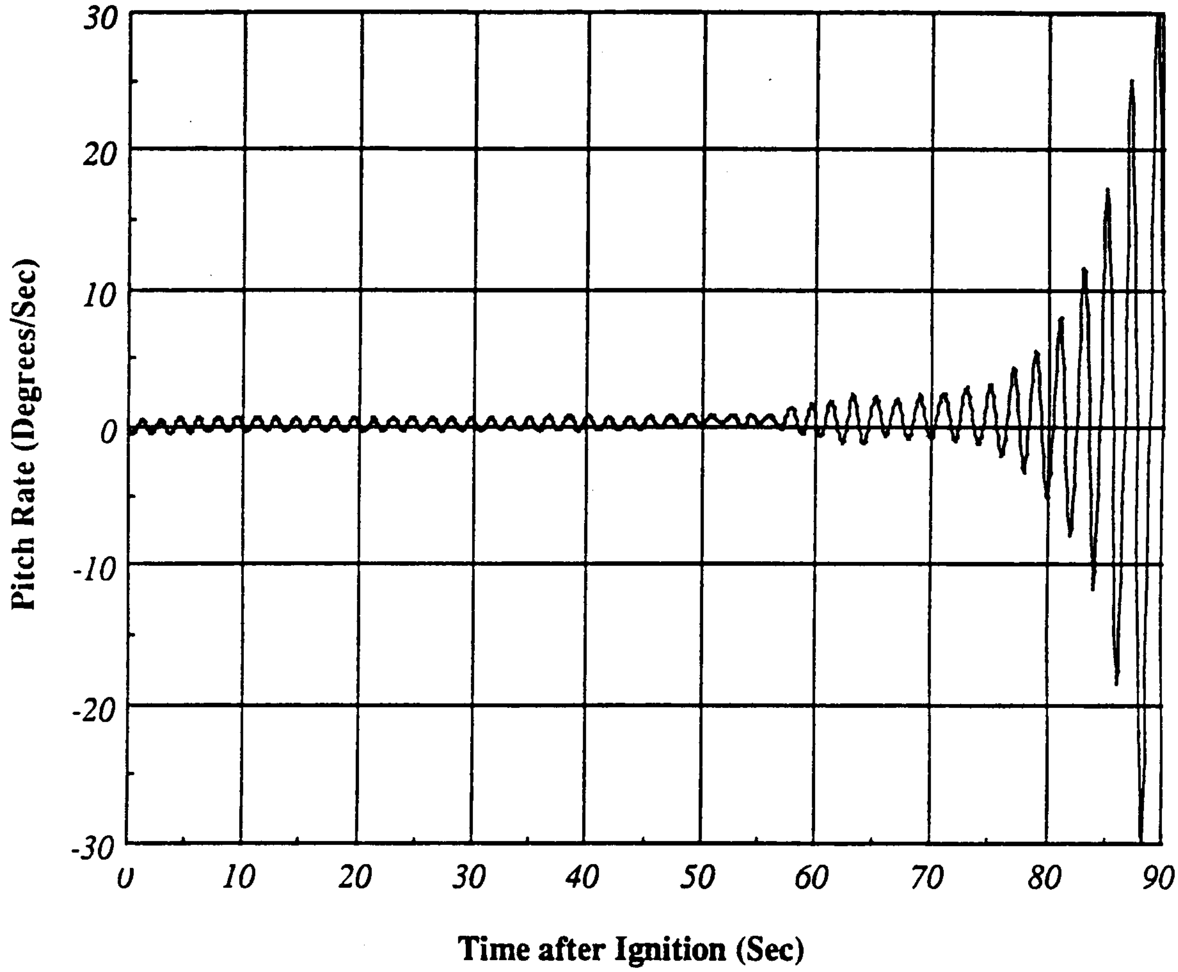

Figure 1. Body-Fixed Pitch Angular Rate vs. Time for Typical PAM-D, Taken from Flandro, et al. [2]

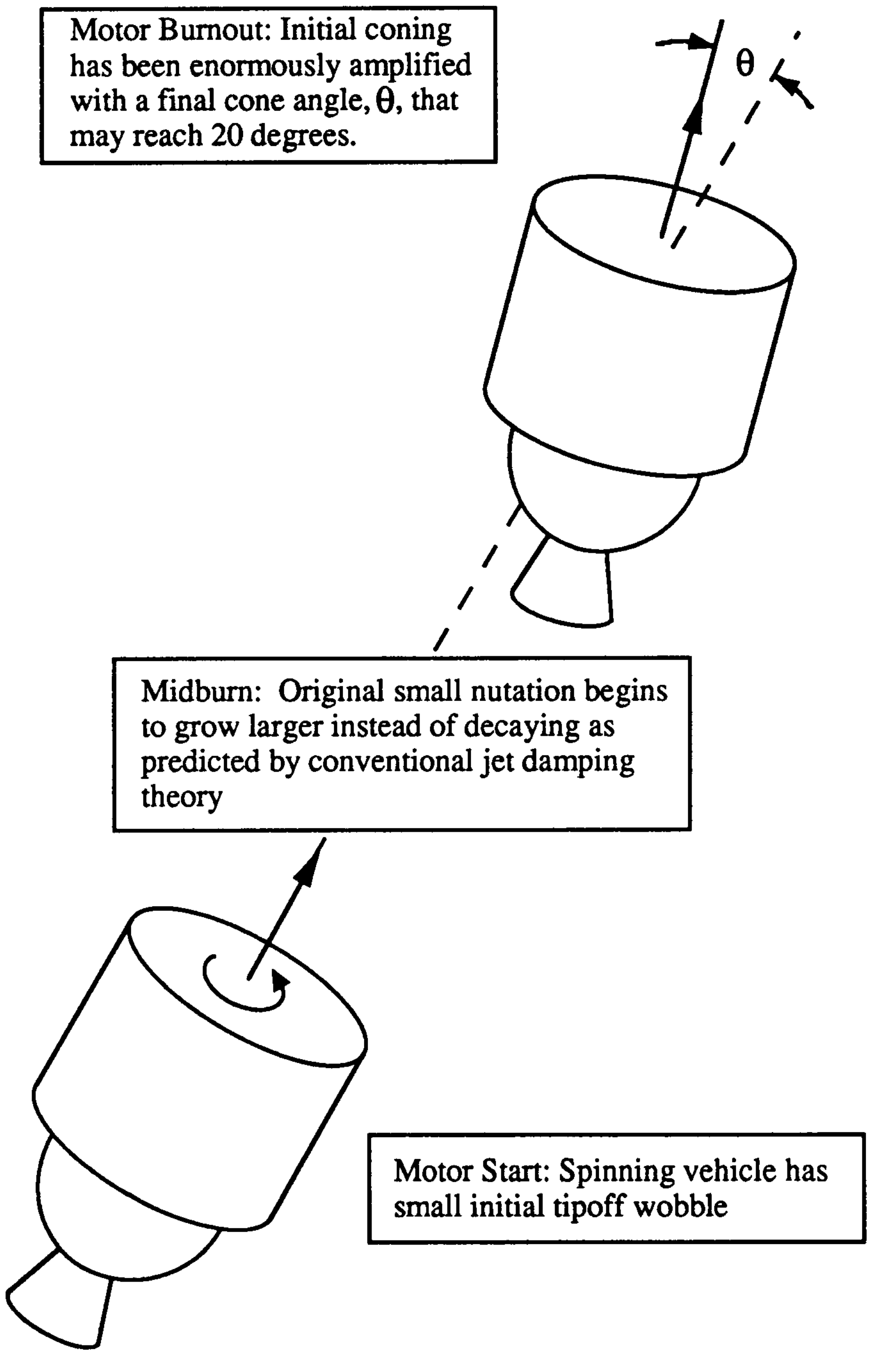

Figure 2. Development of the Coning Instability of a PAM-D Vehicle Adapted from Flandro, et al. [2]

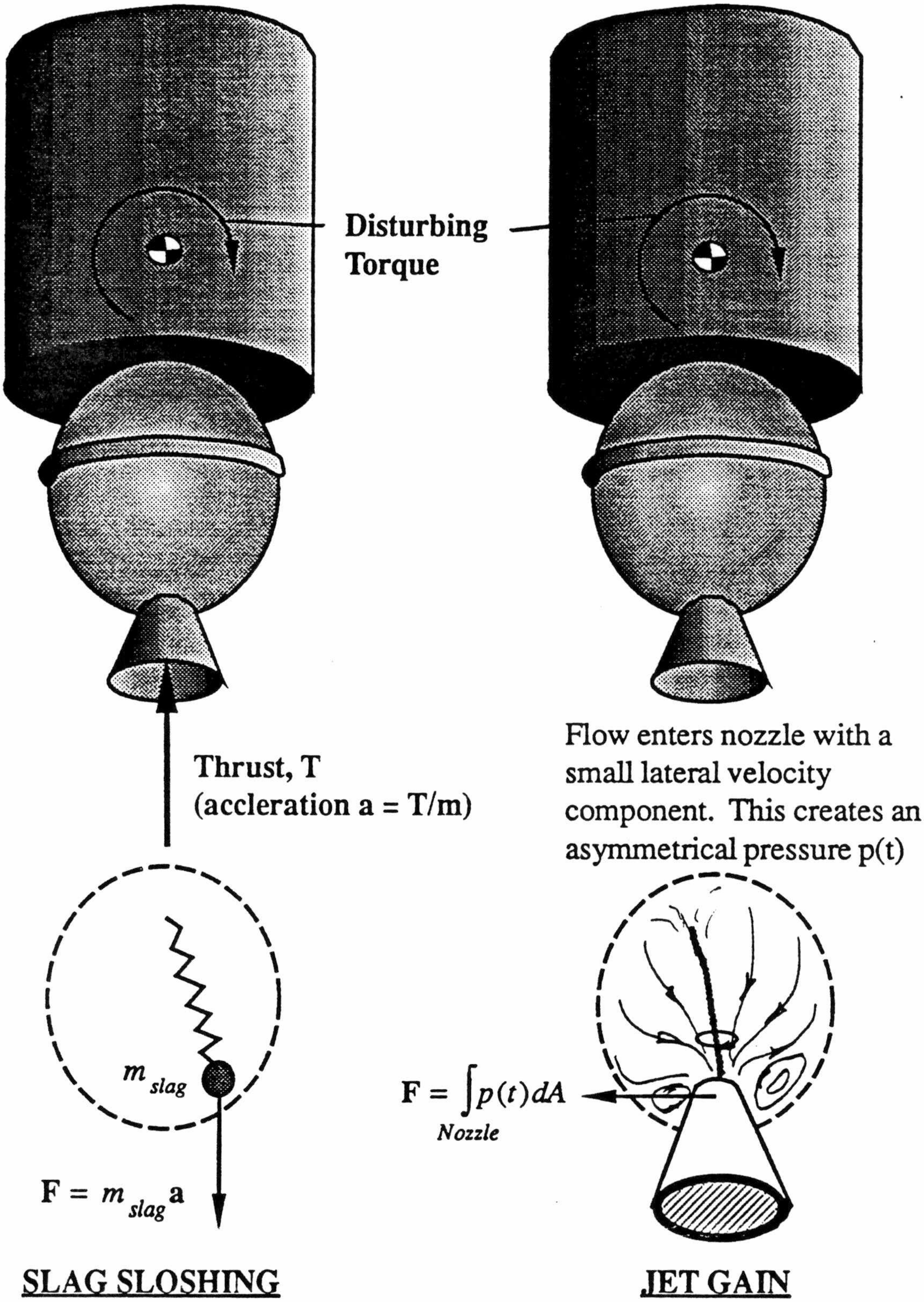

Figure 3. Differences Between the Two Basic Nutation Mechanisms, Taken from Flandro [3]

illustrates the difference between these two mechanisms. There is much debate over which model is correct, or whether it may be a combination of the two.

SCOPE OF CURRENT RESEARCH

Since this coning instability can seriously jeopardize a spacecraft's mission, and since there is still no acceptable explanation for its cause, there is a need for more research on the interaction between the motor internal flow and the vehicle dynamics. A test stand has been constructed to measure the side forces generated in small, spinning solid propellant rocket motors. This data should be useful in predicting the forces generated in full size motors and help to uncover the underlying physical mechanism of the nutation phenomenon.

The test stand constructed at The University of Tennessee Space Institute spins the solid rocket motors about two axes. One electric motor spins the rocket motor about the longitudinal axis, which reproduces the spin of spin stabilized spacecraft. The other electric motor, which is mounted to the floor, spins the rocket motor about a transverse axis. Strain gages are mounted on flexures to measure both thrust and the side forces generated by the solid rocket motor. This apparatus can be seen in Figure 4. Details of the test stand will be described fully later in the report.

The solid rocket motors used in this investigation are cylindrical propellant grains cast from actual STAR 48 propellant mixes. The grains are two inches in outside diameter, have a web thickness of 0.5 inches and have a burn time of about two seconds. Three different grain lengths (2.5, 3.0 and 3.5 inches) are used to examine the effects of the chamber length to diameter ratio. The STAR 48 propellant contains aluminum, which when burned produces aluminum oxide slag. The accumulation of this slag around the

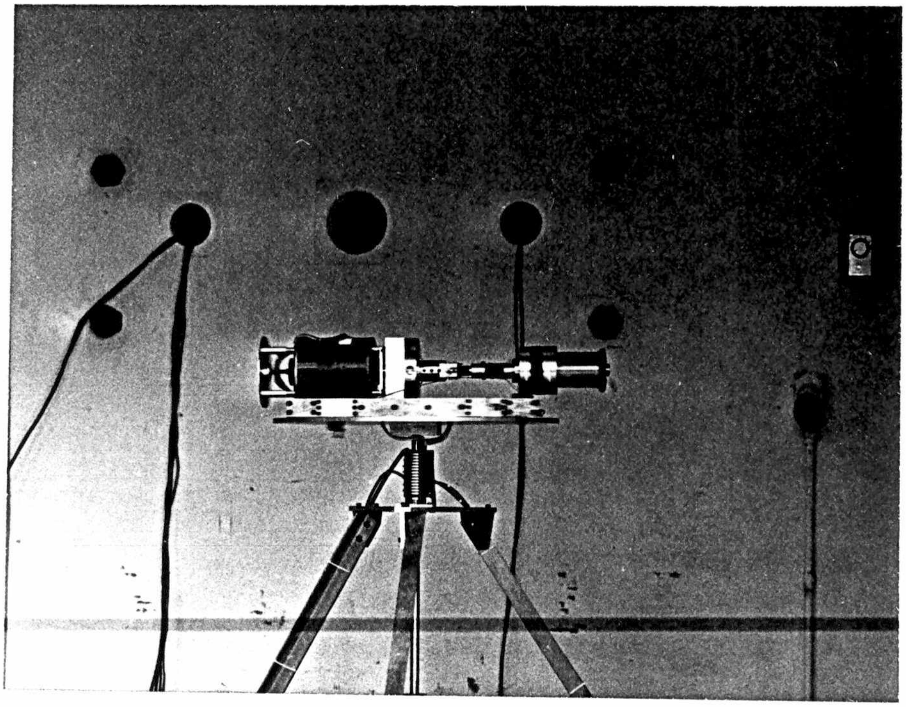

Figure 4. Two Spin-Axis Test Stand for Laboratory Scale Solid Rocket Motors

submerged nozzle will be carefully examined to give insight into whether slag sloshing is the source of the nutation instability. Nonaluminized propellant grains have also been acquired to compare with the aluminized propellant motors. This comparison will be valuable in uncovering the instability source.

RELATED PREVIOUS WORK

Little previous work has been done experimentally in the area of jet damping or in the investigation of the PAM-D coning anomaly. Until the stability problems with the PAM-D vehicles surfaced, analytical models worked sufficiently well that experimental studies were not needed. When the coning phenomenon could not be explained, various groups performed studies to try and uncover what is happening.

Flandro et al. [2,4] has done extensive research on the internal fluid dynamics of a spinning, nutating rocket motor. He proposes that wobbling induces an unsymmetrical traveling vorticity wave that drastically alters the internal pressure distribution and causes a destabilizing effect when the waves are in resonance with the vehicle precession frequency. This theory is known as the "jet gain" model. This is one of two current theories mentioned earlier. Flandro et al. [2] has verified the traveling wave motion using cold flow simulations. The angular velocity environment in a spinning, nutating chamber was reproduced in a laboratory and the resulting wave motion in the chamber was observed. The traveling vorticity waves agree closely with the pattern predicted by analytical results.

Roach et al. [5] developed a full three-dimensional compressible Navier-Stokes numerical algorithm for study of the induced wave motions. So far only axisymmetric flows have been computed, but they indicate that they plan on computing the spinning case with nutation. Although their work represents the preliminary efforts to numerically model the three-dimensional flow, it verified many of the physical features of the jet gain mechanism displayed in the theory.

Flandro et al. [2] also developed a way to measure the nutation interactions using laboratory scale spinning rocket motors. This method is based on the Froude pendulum concept as shown in Figure 5. The rocket motor and an electric spin motor are suspended as a physical pendulum in a double gimbal arrangement free to swing in any direction. This device is used to simulate the angular velocity environment of a spinning, nutating vehicle. The pendulum motion is recorded and any interaction torques can be deduced from this motion. The nutation torques in such a system are very small, making them difficult to measure accurately. The results from these tests were inconclusive but demonstrated a new technique for practical study of nutation characteristics of a spinning rocket motor. This test stand was modified for the tests conducted in the present research.

Other investigators such as Misterek, Murdock and Koshigoe from The Aerospace Corporation [6] have done numerical studies to calculate the moment induced by gas dynamic flow through a spinning, coning vehicle. Rather than numerically solving the full three-dimensional flow equations, they solved two sets of two-dimensional equations. They first looked at inviscid, single-phase flow for different grain configurations at different times during the motor burn. Their study predicted a stabilizing moment for all times during the motor burn, but the moment produced is only 40-80% of the value that is predicted using classical jet damping theory. They then looked at the effects of viscosity and two-phase flow and again only a stabilizing moment was predicted. They conclude that gas dynamic flow is not the cause of the nutation instability experienced by PAM-D vehicles.

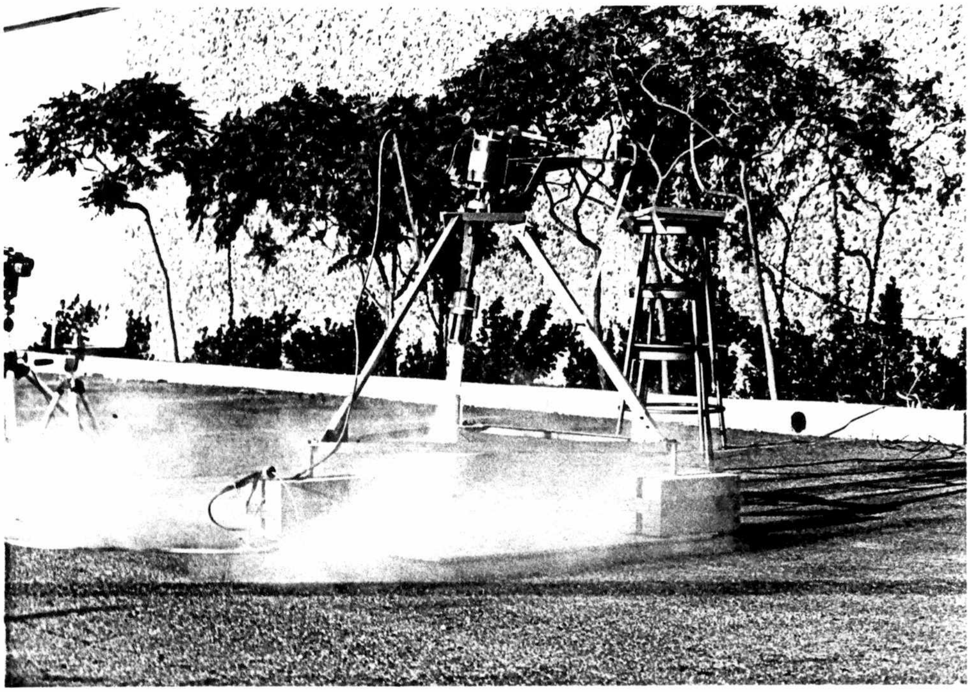

Figure 5. Froude Pendulum Nutation Instability Simulation

Mingori and Yam [7] have investigated the slag sloshing theory. This theory assumes that molten aluminum oxide collects in a pool within the motor chamber and sloshes in response to the wobbling spacecraft. When this pool moves in resonance with the vehicle, a torque is produced because of the mass offset relative to the thrust line. This suggests that the torque should be dependent on vehicle acceleration, but the flight data does not support this relationship. The Mingori model is based on a mass-pendulum model that simulates a spinning slag puddle. This simple model is unsatisfactory in describing the PAM coning because it introduces unknown parameters that cannot be determined from flight data.

The Aerospace Corporation looked at some modified Mingori models in their analysis of the potential coning problem of the Ulysses spacecraft [8]. They had limited success in reproducing the instability using the modified models. This report also summarized the efforts of others in their study of slag motion in laboratory experiments. McDonnell Douglas found that no instability occurs in a coning, PAM shaped chamber unless very large amounts of liquid are used. Hughes also looked at the fluid motion in a spinning bowl but found no instability. Applied Dynamics Laboratories (ADL) did some free-flight experiments with fluid in a motor chamber, but their results were inconclusive. The Aerospace Corporation also indicated they planned on doing some more ambitious experiments on the slag-sloshing theory. As an aside, the Ulysses spacecraft was launched on October 6, 1990 and the nutation control system was able to handle any coning instability.

Kang and Cochran [9] also investigated the slag sloshing theory. Their model consists of a two-body system having a rigid main body, which is the spacecraft, and a spherical pendulum, representing the slag pool. Their simplified equations of motion for the system reveal that the sloshing of the slag is influenced by the main body motion and that the motion of the slag pool affects the motion of the main body. They obtained approximate near-resonance solutions for the equations of motion and determined that under certain conditions an internal near resonance between the rigid body and the pendulum frequencies may exist.

Or [10] modeled the nutational stability of a spacecraft as a rotor-pendulum system. He does not discredit either the gas dynamic or slag sloshing mechanisms. Both mechanisms are similar in that they address a type of resonance interaction and they both can be crudely thought of a point mass attached to the spacecraft that simulates an asymmetric motion of the bulk fluid. Or attempts to reproduce the PAM coning anomaly using a three-degree-of-freedom rotor-pendulum model. He shows that the simple mechanical model is capable of matching telemetric angular rates satisfactorily by adjusting a small number of parameters and concludes that the theory of resonance interaction is the cause for the PAM coning instability.

Flandro et al. [2] also developed a set of scaling laws for the jet gain model. These scaling laws are needed to properly account for the effects of size and dynamical factors so that estimates can be made of the expected coning in new spacecraft configurations. These scaling laws also are useful in developing experiments using laboratory scale rocket motors. One of the features of the coning phenomenon is that the driving torque is linearly proportional to the wobbling angular velocity. This factor of proportionality is called Rgain. Rgain is required to size the attitude control systems that counter the coning growth. Flandro identified the scaling variables that are needed to determine Rgain:

$\dot{m}$ Motor Mass Flow Rate

R Combustion Chamber Radius

Ω Axial Spin Rate

ω Nutation Angular Velocity (1)

L_{cg} Location of Center of Mass Relative to Motor

V_b Gas Speed at the Burning Surface

ρ_o Average Density of Combustion Gas

Since the size of the rocket motor appears to be a factor in the instability, the amount of time a gas particle spends in the motor may be of interest. This time can be expressed as

$$t^* = \frac{R}{V_b} \tag{2}$$

If this residence time is made dimensionless by dividing by a characteristic time such as Ω^{-1}, one gets

$$T = \frac{t^*}{\Omega^{-1}} = \frac{R\Omega}{V_b} \tag{3}$$

This quantity is the inverse of the Rossby number familiar to investigators in rotating fluid theory [11]:

$$Ro = \frac{V_b}{R\Omega} \tag{4}$$

The Rossby number is a measure of the importance Coriolis forces play in modifying the internal flow. Notice that for large chamber radius and spin rate the Rossby number is small. This importance will be discussed later in the report.

Flandro applied dimensional analysis on the above scaling variables and found for the disturbing moment

$$M_{flow} = Rgain\omega = (\dot{m}L_{cg}^2C_t)\omega \tag{5}$$

where C_t is a coefficient that must be determined experimentally;

$$C_t = C_t\left(\mathrm{Ro}, \frac{R}{L_{cg}}, \frac{\omega}{\Omega}\right) \tag{6}$$

This gives

$$\mathrm{Rgain} = \dot{m}L_{cg}^2 C_t\left(\mathrm{Ro}, \frac{R}{L_{cg}}, \frac{\omega}{\Omega}\right) \tag{7}$$

Notice that this factor of proportionality between the disturbing moment and the nutation angular velocity is dependent on physical parameters of the motor. This dimensional analysis shows which parameters are of interest so that laboratory scale tests can be dynamically similar to full size motors. Using equation 7 Flandro was able to predict fairly accurately the value of Rgain that was exhibited by flight data.

There are several references [12-18] that have addressed classical jet damping theory. These models are based on an exceedingly simplified treatment of the internal gas flow of a rocket motor. Specifically, the flow is assumed to be one dimensional and uniform and acts as a rigid body. This model works in some cases but does not apply to large, spinning rocket motors. The next section of this report will address jet damping in detail.

Even though there has been considerable work analytically and numerically, and some basic experimentation has been done, there is still no conclusion as to the exact physical mechanism that is responsible for the coning instability. Since no specific model, either the slag or gas dynamic theory, can be isolated as the culprit, it is very likely that the real environment inside a spinning rocket motor is a complex combination of gas flow effects and slag motion. In fact, X-ray cinematography tests at the Arnold Engineering Development Center (AEDC), where these motors are qualified, suggest that the slag material behaves more like a gas than a liquid. When these motors are tested they are spun on a fixed axis. Facilities do not exist to simulate the coning motion on the ground and may never be built due to the high cost of modifying existing hardware. A fully instrumented spacecraft may be the best source of discovering what causes the coning anomaly. Since testing full size motors is not a viable option, testing laboratory size motors and then scaling the results to apply to larger motors seems the best approach.

II. JET DAMPING

Jet damping is the term that refers to the decrease of a vehicle's lateral angular velocity as a result of gases flowing through the motor chamber and nozzle. It was noticed during the early years of rocketry that there was an interaction between the angular motion of the rocket and the internal gas flow. This effect was analogous to the aerodynamic restoring forces from the external air flow over the fins on the rear of the vehicle; the result of which is to restore the vehicle to head-on flight. Jet damping can be thought of as an internal aerodynamic restoring force that results when the walls of the combustion chamber change their angle with respect to the uniform gas flow. A simple model evolved that is referred to as the "classical jet damping theory."

Classical jet damping theory assumes that the internal gas flow is uniform and parallel to the motor axis. It is also assumed that the flow stream changes in direction only, without being affected any other way. This is saying that the gas acts as a rigid body. This is not a realistic treatment of the fluid mechanics since gas is a deformable medium. When the chamber moves laterally, the gas stream is forced to move with it and this requires that there is a net force applied to the gas. The interaction between the gas flow and the chamber wall results in an asymmetrical pressure pattern. This pressure distribution creates the damping moment. Figure 6 adapted from reference [2] shows this situation graphically. Simple jet damping theory does not depend on axial spin. It is simply the response of the system to changes in direction of the gas stream leaving the system.

Using a body fixed coordinate system, it is useful to identify the inertial forces acting on the gas particles. The most important of these forces is the Coriolis force. The Coriolis force on a particle dm is,

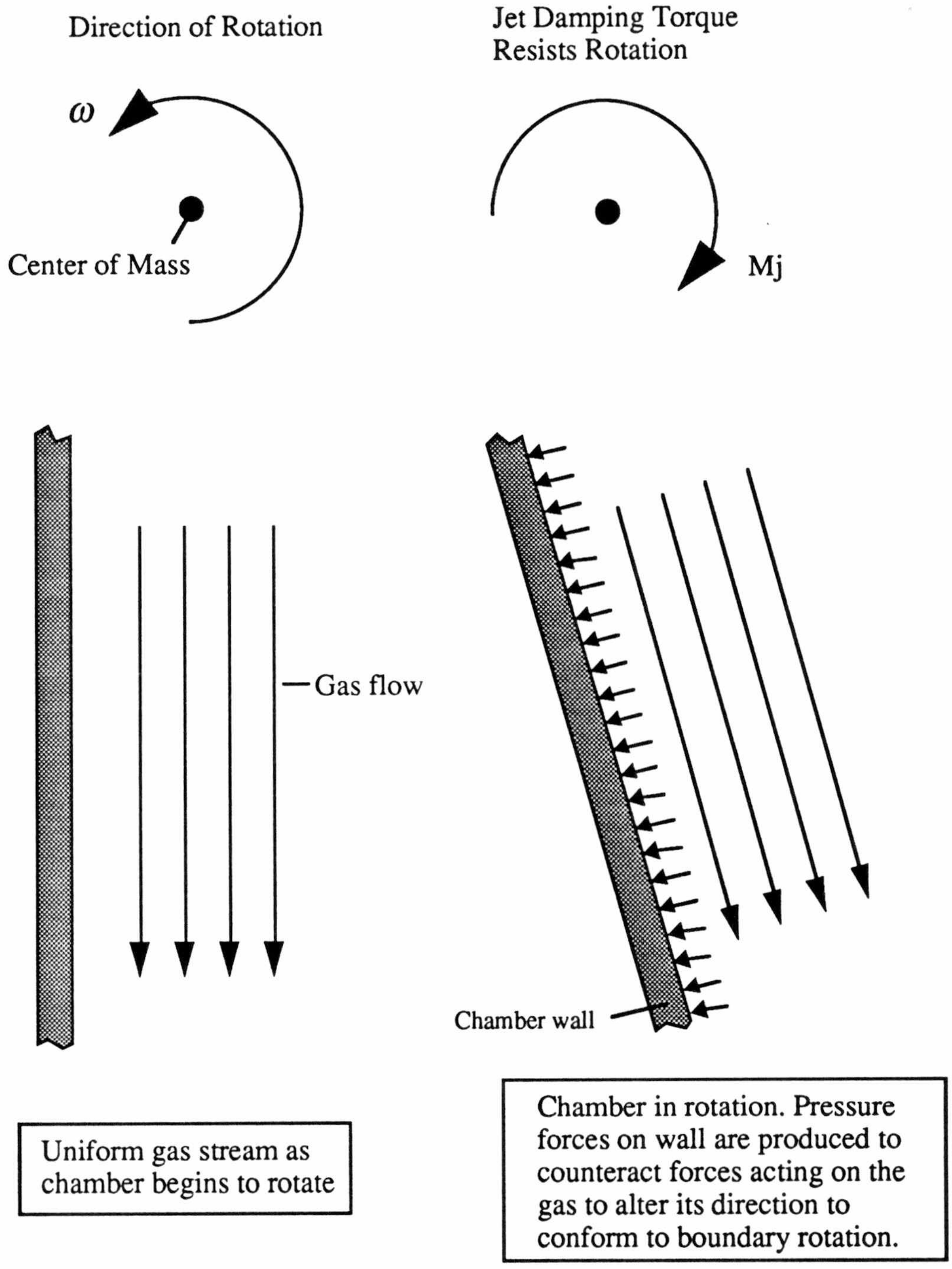

Figure 6. Origin of the Jet Damping Torque
Adapted from Flandro, et al. [2]

$$F_{Coriolis} = (2\omega \times U)dm \tag{8}$$

where ω is the lateral angular velocity and U is the relative velocity of the particle. Flandro et al. [2] has shown, using the classical jet damping assumptions, that the Coriolis force on the gas is equivalent to a nonuniform pressure distribution acting on the internal surfaces of the chamber, which is always a damping effect. Figure 7 adapted from [3] shows this situation graphically. Recall that one of the assumptions of jet damping is that the gas particles are not allowed any relative motion. Here we have just identified a force that acts on the gas particles, but classical jet damping theory assumes that the gas particles are not allowed to change direction or velocity in response to this force. This is clearly an inadequacy of the theory.

Other inertial forces, such as those caused by centripetal and axial acceleration do not cause any net lateral forces on the system because of the symmetry of these influences. The Coriolis force, on the other hand, is asymmetrical. Its force contributions add instead of canceling. The Coriolis effect is the main contributor in the classical jet damping phenomenon.

If classical jet damping theory is overly simplistic then why does it provide reasonable estimates in certain cases, specifically for small slender rockets? If the gas particles move quickly through the system then the deviation in the streamlines caused by Coriolis forces is negligible, so the assumption of parallel, uniform flow is reasonable. But for large rotating motors such as the STAR 48, the particles remain longer within the system, giving them a better opportunity to interact with the vehicle. Recall that the Rossby number is

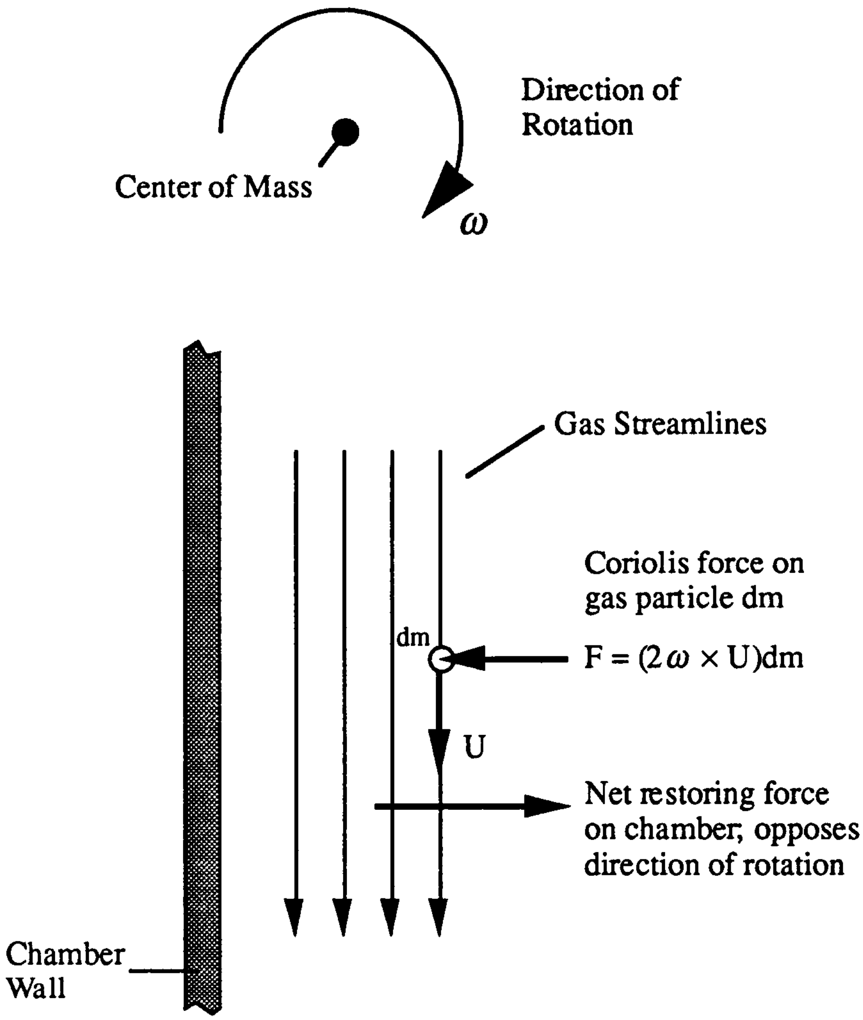

Figure 7. Effect of Coriolis Force Acting on Gas Volume
Adapted from Flandro [3]

$$Ro = \frac{V_b}{R\Omega} \tag{9}$$

where V_b is the gas speed at the burning surface, R is the combustion chamber radius and Ω is the axial spin rate. The Rossby number is a measure of the importance of Coriolis forces in shaping the internal flow field. A small Rossby number indicates that Coriolis effects play a strong role in modifying the internal flow field.

Notice that for small vehicles the Rossby number is large, and the assumption of uniform flow unaffected by vehicle wobble is reasonable. But for larger motors, such as the STAR 48 and STAR 63, the Rossby number is much smaller. Figure 8 from reference [2] illustrates the variation of Rossby number with time for PAM D (STAR 48), D II (STAR 63) and the smaller STAR 37 propelled vehicles. Rossby number decreases with time because chamber radius, R, increases as propellant is consumed. The STAR 37 propelled vehicles did not exhibit the coning instability, the other two vehicles did. Comparing flight data with Rossby number shows that coning occurs when the Rossby number approaches unity or smaller. Since the internal gas flow speeds and spin rates are similar among the three different sized motors in Figure 8, it is clearly the size of the chamber that distinguishes the three.

To reiterate, the larger the motor size, the longer the residence time of the gas particles. The longer the gas particles are in the system, the more opportunity for Coriolis forces to modify the internal flow. The more Coriolis forces modify the flow, the assumption of uniform, parallel flow is incorrect and jet damping theory fails. Clearly the internal flow field of larger spin stabilized motors, such as the STAR 48, becomes very complex and some interesting things happen that cause the coning anomaly. In other words, the jet damping becomes a jet driving. It is interesting to note that reducing

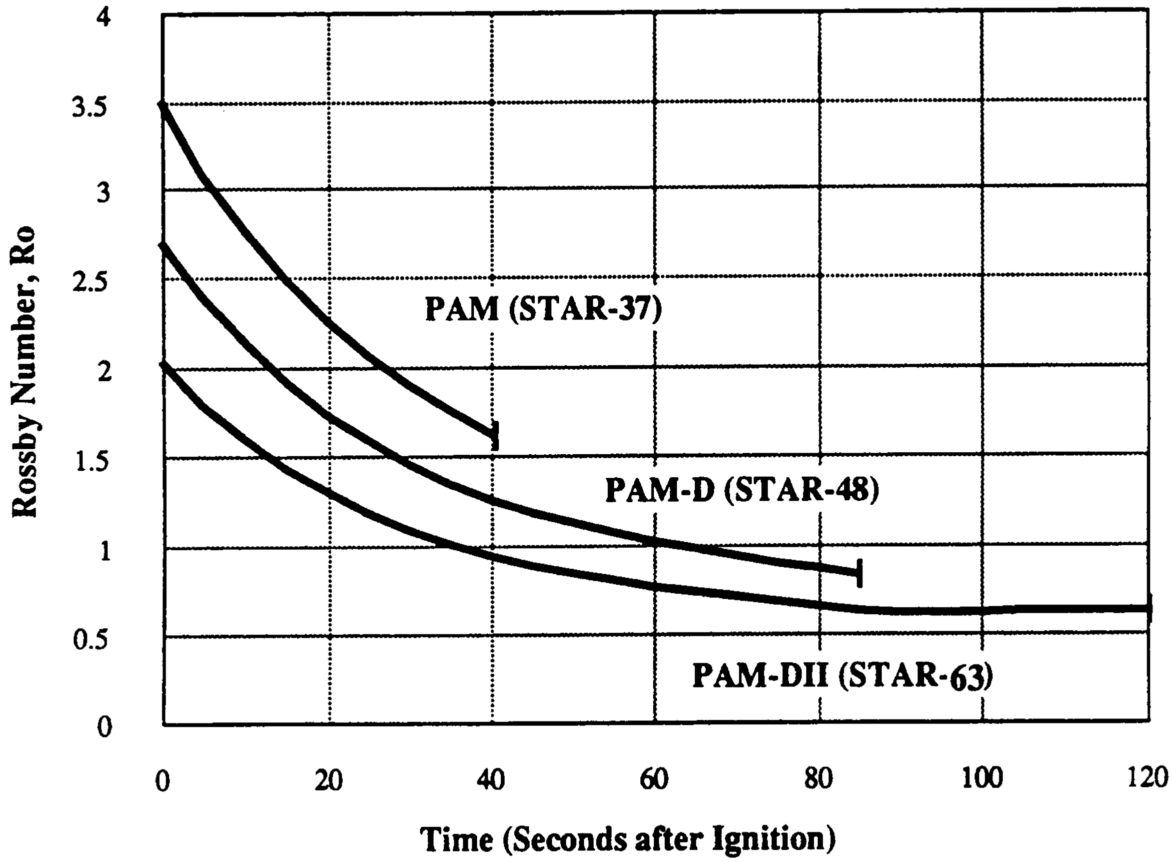

Figure 8. Variation of Rossby Number with Time for Typical Spinning Stages Taken from Flandro et al. [2]

the spin rate, Ω, increases the Rossby number and should lessen the coning instability, but these spacecraft are still being spun at the same typical rates.

JET DAMPING EQUATIONS

The first formal mention of jet damping in the literature was in the text on the theory of rocket flight by Rosser, Newton and Gross [12]. Their approach to model the jet damping effect is based on a simple momentum balance of the system to estimate the effect on lateral motion of the vehicle. This is the classical treatment of jet damping that is used by other investigators later on [13-18]. Axial spin was not accounted for by Rosser et al. [12] in their analysis.

The system considered by Rosser et al. [12] consists of a rocket that is rotating about a transverse axis at an angular velocity ω. The moment of inertia about this axis is

$$I = mk^2 \tag{10}$$

where m is the instantaneous mass and k is the radius of gyration about the transverse axis. Let r_e be the distance from the vehicle mass center to the nozzle exit. Assuming uniform flow across the nozzle exit, the sideways velocity of the gas particle leaving the system is $r_e \omega$. This can be seen in Figure 9. The rate at which the gas particles are removing angular momentum is then $\dot{m} r_e \omega$. The angular momentum of the rocket is

$$H_{rocket} = I_{rocket}\omega = m_{rocket}k^2\omega \tag{11}$$

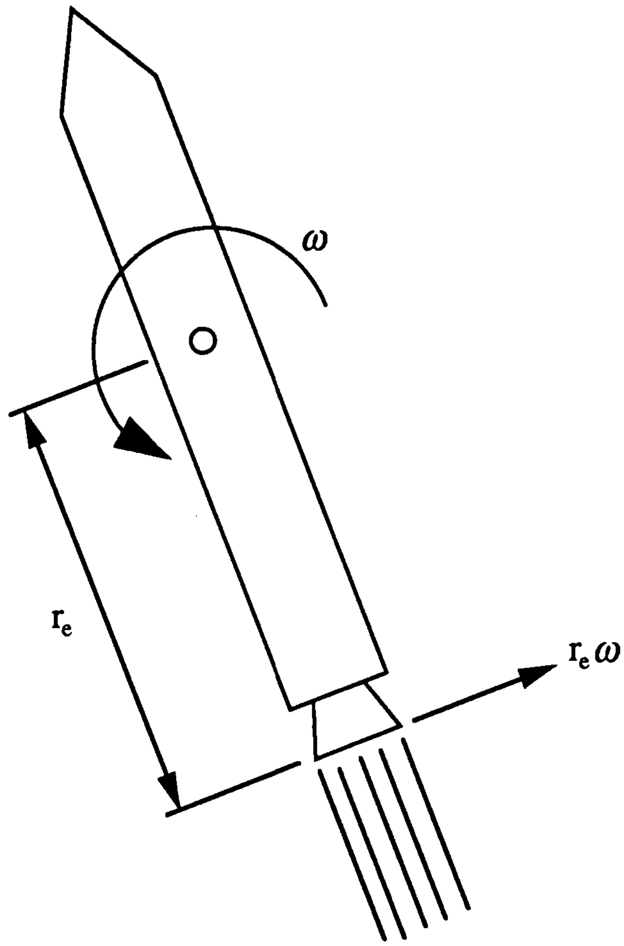

Figure 9. Nonspinning Rocket Rotating About a Transverse Axis

The rate of change of this angular momentum is then:

$$\frac{dH}{dt} = \frac{d}{dt}\left(mk^2\omega\right) \tag{12}$$

Adding the angular momentum rates of the rocket and the gas particles gives:

$$\frac{d}{dt}\left(mk^2\omega\right) + \dot{m}r_e\omega = \text{Externally applied torques} \tag{13}$$

Assuming no external applied moments and rearranging,

$$\frac{d}{dt}\left(mk^2\omega\right) = -\dot{m}r_e\omega \tag{14}$$

which states that the rate of change of system angular momentum equals the rate of flux of lateral angular momentum. Carrying out the derivative on the left side gives:

$$\frac{d}{dt}\left(mk^2\omega\right) = mk^2\dot{\omega} + m\omega\frac{dk^2}{dt} + \omega k^2\frac{dm}{dt} \tag{15}$$

Since mass is lost as fuel is being burnt,

$$\frac{dm}{dt} = -\dot{m} \tag{16}$$

The rate of change of the radius of gyration is small so we can neglect that term. Putting this all together gives:

$$mk^2\dot{\omega} - \dot{m}\omega k^2 = -\dot{m}r_e\omega \tag{17}$$

Rearranging,

$$mk^2\dot{\omega} = -\dot{m}\omega\left(r_e^2 - k^2\right) \tag{18}$$

The term on the right is the classical definition of the apparent jet damping moment,

$$M_J = -\dot{m}\omega\left(r_e^2 - k^2\right) \tag{19}$$

Rosser et al. [12] were concerned about their assumptions in their analysis. They questioned whether or not the sideways velocity of the gas at the nozzle exit is $r_e\omega$ or if a better estimate is $r_t\omega$, where r_t is the distance from the vehicle center of mass to the nozzle throat. After the throat the gas stream is supersonic and probably does not acquire any additional lateral motion.

Thomson [14] developed the jet damping equation the same way as Rosser et al. [12] for a nonspinning rocket and then he integrated the equation to get,

$$\frac{\omega}{\omega_o} = \left(\frac{m}{m_o}\right)^{\frac{r_e^2}{k^2} - 1} \tag{20}$$

where ω_o and m_o are the initial angular velocity and mass. When r_e/k is greater than unity, which is usually the case for typical slender vehicles, ω decreases and the action of the jet is that of a damper. Thomson then addressed the case of a spinning rocket with a cluster of nozzles. For the case of a spinning rocket rotating about a transverse axis with a single nozzle, the jet damping equation about the transverse axis is the same as for the nonspinning case. This means that according to the classical treatment of jet damping, spin has no effect on the internal flow.

Kolk [15] also addressed jet damping in his text on flight dynamics. He too took the angular momentum approach to describe the jet damping effect and gives a description of the process that is easy to understand:

> "Consider a rocket that is only yawing. As the propellant burns it is shoved toward the exit. This gives an increase in yaw inertia and, since angular momentum is conserved, the yaw rate must decrease. The analogy is to be found in a spinning figure skater. Drawing the arms inward decreases the inertia and increases the spin rate, while extending the arms has the opposite effect. Whenever the propellant in a rocket burns at a location closer to the center of gravity than the exhaust exit , the thrust damping will be positive. On the other hand, whenever it burns at a location more remote from the center of gravity than the exit the thrust damping will be negative."

Rott and Pottsepp [16] analyzed jet damping from the fluid dynamic viewpoint and showed that jet damping is a result of Coriolis forces. For a rocket with a liquid fuel system they give an equation for the jet damping moment as,

$$N_z = -\omega_z \dot{m}\left(x_e^2 - x_o^2\right) \tag{21}$$

where ω_z is the angular velocity about the z-axis, $\dot{m}$ is the mass flow rate, x_e is the distance from the vehicle center of mass to the nozzle exit and x_o is the distance to the liquid-free surface in the tank. They also consider the case of a solid fuel rocket engine. The equation for the jet damping moment for a solid propellant rocket is,

$$N_z = -\omega_z \dot{m}\left[x_e^2 - \frac{1}{3}\left(x_n^2 + x_n x_\circ + x_\circ^2\right)\right] \quad (22)$$

where x_n is the coordinate of the nozzle entrance. As with other investigators, Rott and Pottsepp make some simplifications; namely that the fluid flow is inviscid, no angular acceleration, that the flow field is parallel to the longitudinal axis and the vehicle is not spinning about the longitudinal axis.

Misterek, Murdock and Koshigoe [6] compared their numerical results with the jet damping value obtained from one-dimensional flow theory. The equation they used for the jet damping moment is,

$$M_y = -\omega_y \dot{m}\left(Z_2^2 - Z_1^2\right) \quad (23)$$

where ω_y is the transverse angular velocity, $\dot{m}$ is the total mass flow rate, Z_2 is the nozzle exit coordinate and Z_1 is the propellant location relative to the center of mass. Since the propellant surface is curved (PAM motor), they used the smallest and largest possible values for the propellant location, Z_1, to bound the jet damping moment. As mentioned before, their numerical results predict a moment that is only 40-80% of the moment given by equation 23.

Flandro et al. [4] gives an equation for the jet damping moment for a cylindrical combustion chamber,

$$M_J = -\dot{m}\omega\left(L_{cg} - \frac{2b}{3}\right)\left(L_n + 2b\right) \quad (24)$$

where $\dot{m}$ is mass flow rate, ω is the angular velocity, L_{cg} is the position of the nozzle exit with respect to the spacecraft center of mass, L_n is the length of the nozzle and 2b is the length of the combustion chamber. This equation assumes that mass flow rate increases linearly along the combustion chamber and that combustion occurs at both the sidewalls and the forward wall of the cylindrical chamber.

One can see that each investigator has come up with their own form of the classical jet damping equation, but they are all similar in that the moment is the product of mass flow rate, angular velocity and a term that depends on vehicle geometry. Which of these equations gives the best estimate for jet damping has yet to be proven.

Flandro et al. [2] also examined the classical jet damping effect from an Eulerian fluid mechanics point of view, as opposed to the Lagrangian approach used by most investigators. This resulted in the following equation,

$$\mathbf{M}_J = -\int_V \mathbf{r} \times (2\boldsymbol{\omega} \times \mathbf{u})dV = -\int_S \mathbf{r} \times (p'\,\mathbf{n})dS \qquad (25)$$

where **r** is the position vector for the body-fixed coordinate system, **ω** is the angular velocity vector, **u** is the propellant velocity vector and p' is the time dependent pressure. The integral on the left is the volume integral of the Coriolis forces over the gas volume contained within the motor chamber. The integral on the right is the integrated pressure forces acting on the internal surfaces of the chamber. The equivalence of these two integrals says that in the case of the classical jet damping assumption of a uniform, steady flow that always adjusts to the chamber motion without dynamic interaction forces, the pressure balances the Coriolis forces and a damping torque results [2].

It should be reemphasized that all the estimates for the jet damping moment in this section are based on classical jet damping assumptions. They do not address the actual fluid dynamics inside the combustion chamber. They are crude estimates that apply for some rocket geometries, but are inadequate for larger, spinning motors, such as the STAR 48.

III. EXPERIMENTAL SETUP

The test apparatus used in this investigation is an extension of experimental work performed by Flandro et al. [2]. Flandro developed a way to measure the nutation interactions using laboratory scale spinning rocket motors. This method is based on the Froude pendulum concept as shown in Figure 5. The rocket motor and a 1/4 hp electric motor are suspended as a physical pendulum in a double gimbal arrangement free to swing in any direction. This device is used to simulate the angular velocity environment of a spinning, nutating vehicle. Tests were conducted with the pendulum motion simulating a 30° cone angle at the beginning of the motor burn. The pendulum motion was recorded by means of a mechanical linkage moving an encoding device and any interaction torques can be determined in principle by observing the pendulum motion. The angular velocity of the pendulum is set by the natural frequency of the pendulum swing. This was lower than desired due to the heavy mass of the 1/4 hp electric motor that was used to spin the rocket motor at 1725 rpm. As a result, the interaction torques were too small to detect by means of changes in the free motion. The results from these tests were inconclusive but demonstrated a new technique for practical study of the characteristics of a spinning rocket motor. Most of this original hardware is used in the present study. The main modifications are that the pendulum assembly is now mounted horizontally on a spin table to increase the angular velocity and improvements in the data acquisition system have been made.

The 1/4 hp electric motor, referred to as the secondary electric motor, and the solid propellant rocket motor are mounted horizontally on a circular spin table. This spin table sits on a 3/4 inch shaft that is driven by a 1 hp DC electric motor, referred to as the primary electric motor, attached to the concrete floor. The shaft passes through a pilot bearing at the top of the tripod structure. The tripod legs are also attached to the floor to keep the structure from moving. Strain gages are mounted on flexures on the spin table assembly. These strain gages measure both the sideforce generated by the rocket motor and thrust of the rocket. Power for the 1/4 hp electric motor, the igniter and signals to and from the strain gages pass through a 14 channel slip ring assembly on the 3/4" shaft. The 1/4 hp electric motor spins the rocket motor about its axis of symmetry at a constant 1725 rpm. The 1 hp electric motor that spins the table is controllable and is capable of turning the table from 140 rpm up to its maximum speed of 1725 rpm. This arrangement creates an angular velocity environment that is of interest in investigating jet damping phenomenon. It spins the solid propellant rocket motor about its longitudinal axis, simulating the spin of spin stabilized vehicles, and it also spins the rocket motor about a transverse axis. These angular velocities and body fixed coordinate system are shown in Figure 10. Details of the test apparatus components will be given in subsequent sections.

The experiments were conducted in a test bay in The University of Tennessee Space Institute's propulsion laboratory. A schematic layout of the test facility is shown in Figure 11. The test stand is located in the test bay while the data acquisition hardware and TV monitor are located on the other side of a reinforced concrete wall. There are ports in this wall to run cables through. One wall of the test cell has a large retractable door that is opened during the tests. A video camera is placed outside looking into the test bay so that the testing can be monitored in the control room.

DESIGN REQUIREMENTS

The design requirements for the test stand is to be able to spin the solid rocket motor about at least two axes and be able to accurately measure the moment generated by the solid rocket motor, whether it is in the damping direction (moment opposes angular

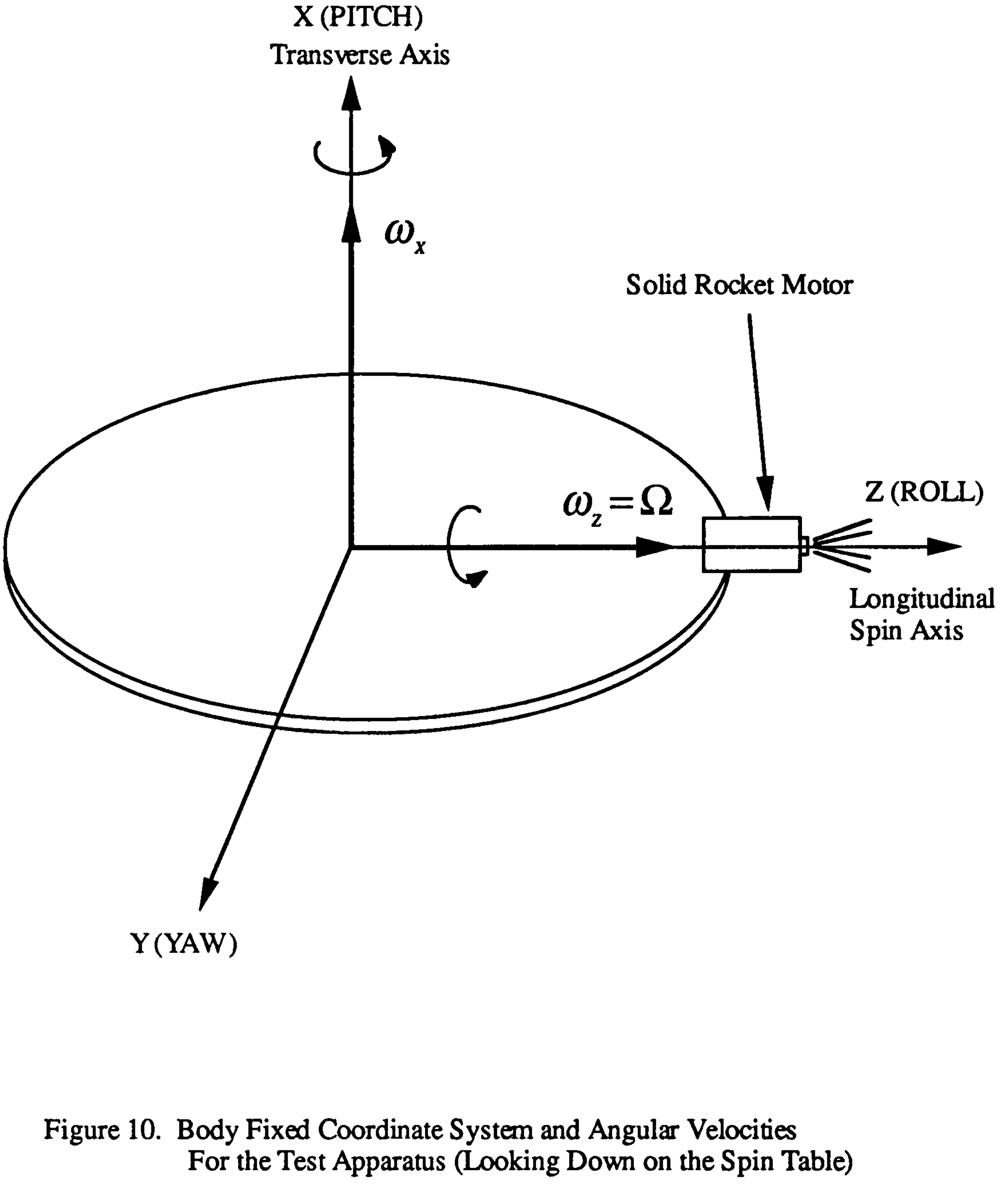

Figure 10. Body Fixed Coordinate System and Angular Velocities
For the Test Apparatus (Looking Down on the Spin Table)

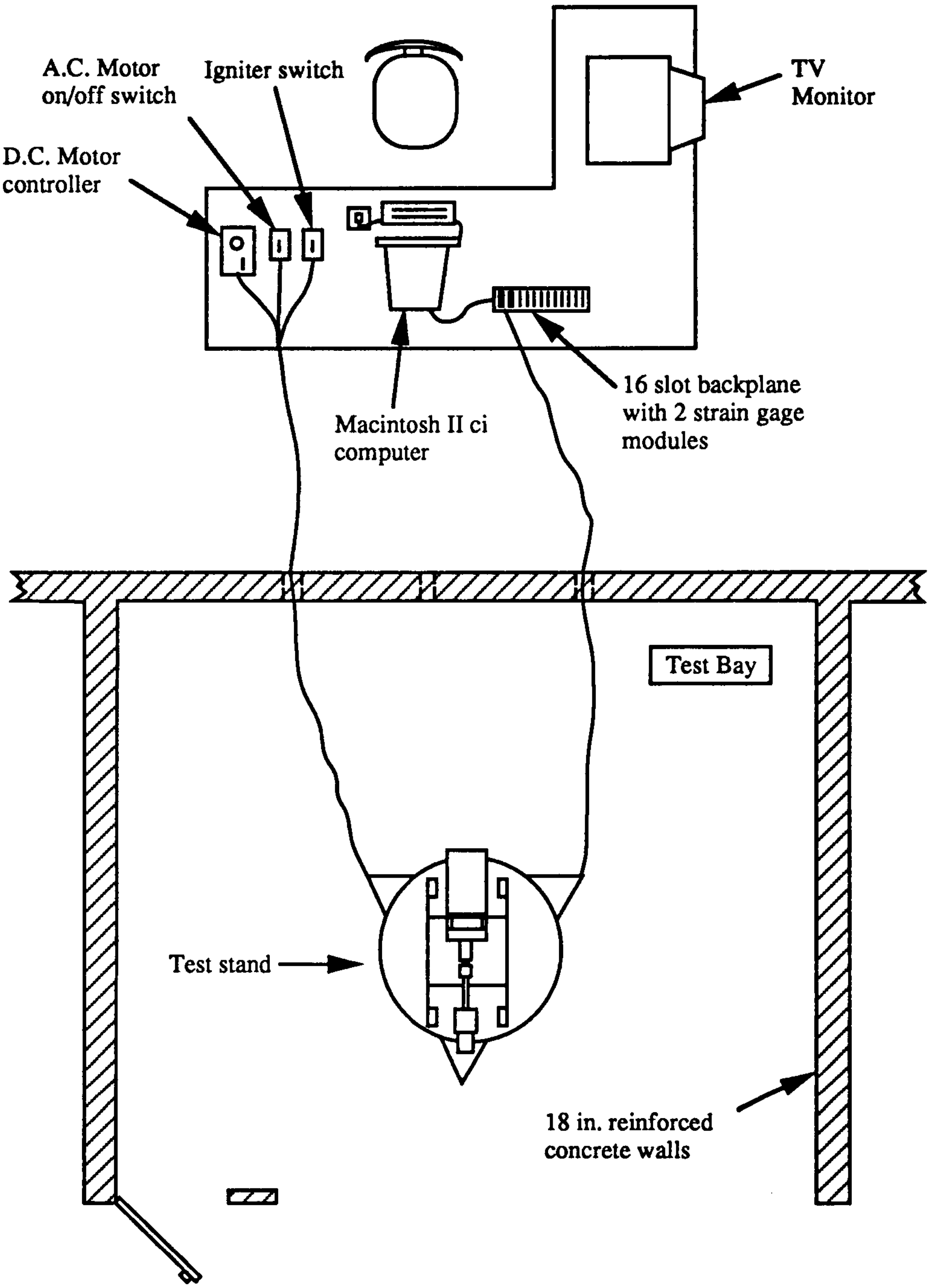

Figure 11. Schematic of Test Facility

velocity about the transverse axis) or in the driving direction (moment is in the same direction as angular velocity). Since jet damping and jet driving moments are related phenomenon, both are proportional to the transverse angular velocity and have similar magnitude, the test stand is designed to be capable of measuring either moment. The jet damping moment is known to exist in rockets rotating about a transverse axis, whether it is spinning or not. By being able to spin the rocket motor about its longitudinal axis, it is hoped that the jet driving mechanism will be activated and can accurately be measured. Since little experimental study has been done on either jet damping or jet driving, any results from the tests should be useful.

One of the problems was deciding on the best way of modifying the existing pendulum arrangement. As it existed, the solid rocket motor could swing in any direction on its gimbals. One idea was to fix one of the gimbals so that the pendulum could only swing in a plane, thus simplifying the movement. But the pendulum swing frequency was still too low to generate any appreciable moments from the rocket motor. Driving the pendulum motion with an electric motor was also considered but presented some more problems. The angular velocity vector of the pendulum changes direction every half period of the pendulum swing. A constantly changing angular velocity environment is not ideal for trying to isolate small forces generated by the rocket motor. Finally it was decided to mount the pendulum arrangement horizontally on a spin table so that its angular velocity was always in the same direction.

Once this was decided, the best way to measure the jet damping effects had to be resolved. One idea was to spin the table up to the desired speed and then let it coast. The rocket motor would then be fired and accelerometers would be used to determine if the table was rotating faster or slower than if the motor was not firing. From this, the direction and magnitude of the moment generated by the rocket motor could be determined.

It was decided that strain gages would be more sensitive for data acquisition. The spin table is rotated at a constant rpm by the primary electric motor. The pendulum assembly (1/4 hp electric motor on one end and the solid rocket motor at the other) sits on a flat square piece of aluminum raised above the spin table. Each corner of this piece of aluminum is attached to flexures. The other end of each flexure is then attached to the spin table. Strain gages are affixed to two of these flexures. Once the entire structure is brought up to speed, any side force in the rocket motor will cause relative motion of the flexures and the strain gages will pick up this motion. Figure 12 shows this arrangement and location of the strain gages.

Recall that Rossby number is an important parameter in investigating the jet gain theory. It is when the Rossby number falls below unity that the nutation growth occurs in the PAM-D vehicles. Therefore, to make laboratory scale testing dynamically similar, the Rossby number should match the flight Rossby number. Rossby number is given by

$$Ro = \frac{V_b}{R\Omega} \tag{26}$$

The gas speed at the burning surface, V_b, for the 2 inch rocket motors is about 8 ft/sec. The combustion chamber radius, R, begins at about 0.5 inch and ends at 1 inch. The spin rate, Ω, of the secondary electric motor is 1725 rpm. Figure 13 shows how Rossby number varies with time during the motor burn. Notice that the Rossby number falls below unity approximately 0.4 sec into the 2 sec burn. The only controllable variable in equation 26 is the spin rate, Ω, and this was chosen to be 1725 rpm to put the Rossby number into the range of interest.

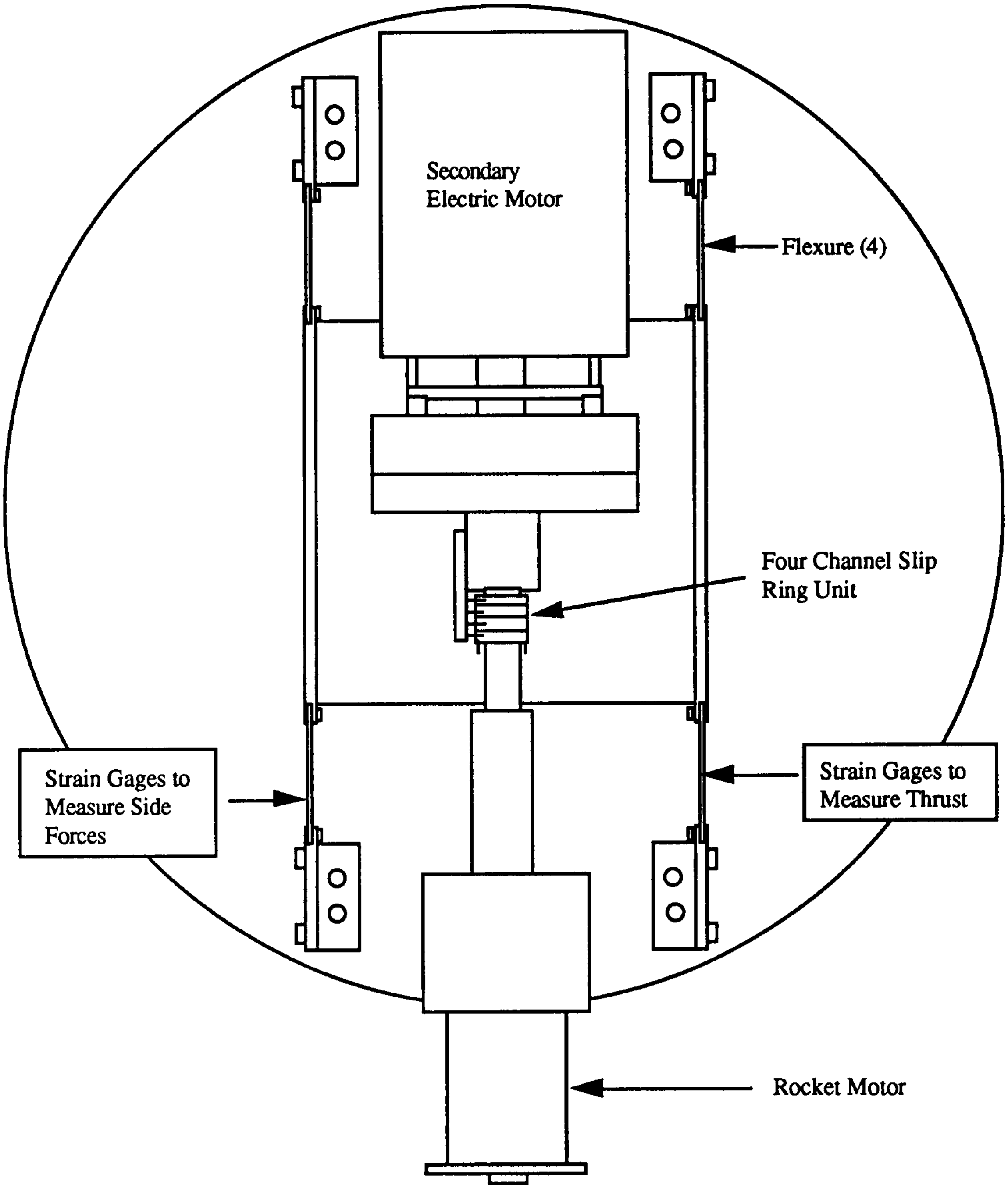

Figure 12. Top View of Test Apparatus Showing Location of Strain Gages

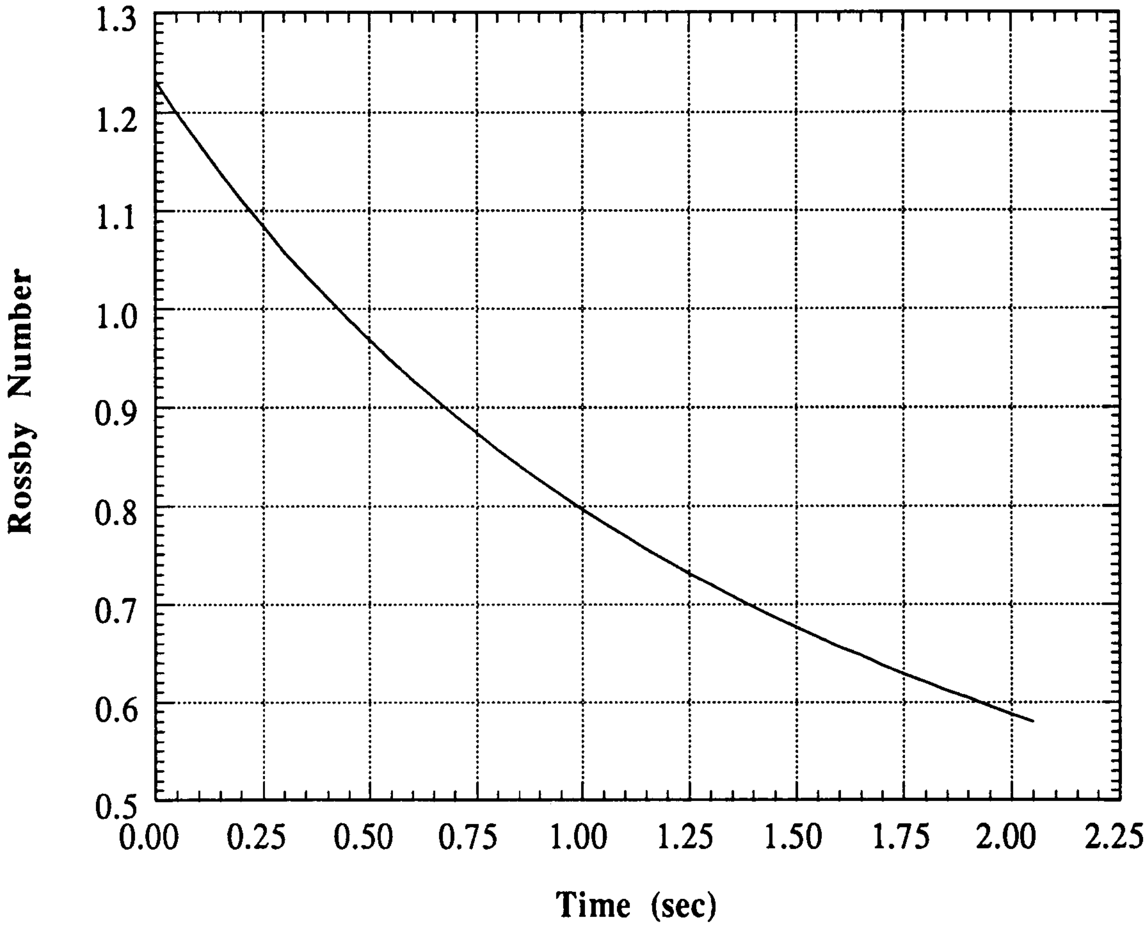

Figure 13. Rossby Number vs. Time for 2.0 Inch Rocket Motors

SOLID PROPELLANT ROCKET MOTORS

The aluminized solid rocket motors used in this investigation are cylindrical propellant grains cast from actual STAR 48 propellant mixes. The composition of this mix is 71% AP, 18% Al and 11% HTPB Binder [1]. The grains are two inches in outside diameter, have a web thickness of 0.5 inches and have a burn time of about two seconds. Three different grain lengths (2.5, 3.0 and 3.5 inches) are used to examine the effects of the chamber length to diameter ratio. Eleven of these motors were obtained for the experiments; three of the 2.5 inch motors, five of the 3.0 inch motors and three of the 3.5 inch length. The 2.5 inch motors weigh 0.38 lb before burn (propellant plus casing), the 3.0 motors weigh 0.46 lb and the 3.5 inch motors weigh 0.54 lb. These grains are inhibited at each end so that they produce a moderately progressive pressure trace.

The rocket motors are slipped into a stainless steel cylinder. The 2.5 inch and 3.0 inch motors require spacers at the head end of this cylinder but the 3.5 inch motors do not. Both ends of this cylinder mate to O-rings to provide combustion chamber sealing. The aft enclosure is equipped with a replaceable converging-diverging submerged nozzle with a graphite nozzle entrance section. The nozzle throat size was determined to give an average combustion chamber pressure similar to conditions in a STAR 48, about 600 psi. These nozzles have an area ratio (exit area / throat area) of 6.3. The head end of the combustion chamber is equipped with a spring loaded closure system. So if the pressure becomes too great, the springs compress and the pressure is released.

Ten of the nonaluminized propellant grains were obtained, unfortunately their outer diameter was slightly larger than the aluminized grains so they could not fit into the metal cylinder. The nonaluminized rockets are 3.75 inches long, have an outer diameter of 2.5 inches, have a web thickness of 0.5 inches and weigh 1.0 lb (propellant plus casing). New hardware to accommodate these grains was manufactured, but time did not allow the firing of the nonaluminized propellants.

The solid rocket motors are ignited with 1 gram of $BKNO_3$ "baggie" igniters and an electric match. The $BKNO_3$ powder is wrapped up in a piece of thin cellophane and the electric match (like those used to ignite model solid rocket motors) is inserted into one end of the baggie. This baggie is placed inside the combustion chamber with the electric match's leads sticking out of the nozzle. A 12 V car battery provides power for the ignition. The 12 V passes through two sets of slip rings to get to the igniter. The first slip ring assembly is the 14 ring unit on the 3/4 inch shaft and the other assembly has four rings and is on the shaft between the 1/4 hp secondary electric motor and the solid rocket motor. The switch for the igniter is in the control room and is operated manually.

TEST STAND HARDWARE

This section describes the various components that make up the test stand in more detail. The tripod legs of the test stand are made from 3/16 inch thick angle aluminum. The bottom of each leg is attached to the corner of a triangular base also made of 3/16 inch thick angle aluminum. Each corner of the base is height adjustable for leveling purposes. Another piece of angle aluminum is laid across each corner of the base and is used to hold each corner down. A 3/8 inch bolt passes through each piece to an anchor embedded in the concrete floor. The top of each tripod leg is attached to a triangular shaped 3/8 inch thick piece of aluminum. A pilot bearing for the 3/4 inch stainless steel shaft is pressed into the center of this piece of aluminum. The 3/4 inch shaft is also a press fit into the bearing.

In the center of the triangular base on the floor is the primary electric motor that spins the table. This is a 1 hp DC electric motor manufactured by MagneTek Indiana

General, Catalog number DO62. The maximum rpm of this motor is 1725 rpm. The rpm of this motor is controlled by a K-Line DC motor controller made by Electrol Co., Inc. located in the control room. This controller takes 230 V AC from a wall socket and converts it to DC. The controller box has an on/off switch and a dial that reads from 0 to 100%. The percentage on the knob corresponds to the percent of maximum rpm of the electric motor that it is controlling. Used "as is" from the manufacturer, the controller knob had to be turned to 20% to start the table spinning, this corresponds to a table rpm of about 140 rpm. The controller knob was increased and the table rpm was found using a strobe light. The controller was taken up to 29% which corresponded to a table speed of 400 rpm. Figure 14 shows the relationship between table rpm and controller setting. The data points at a controller setting of 35% and 40% are points that lie on the curve fit of the measured lower rpm points. Since it was necessary to stand next to the table with the strobe light to measure the table rpm, it was decided to stop at 400 rpm for safety reasons. If something were to break rotating at these high rpms, it could result in serious injury.

The 1 hp electric motor is mounted vertically to some thick aluminum stock. These pieces of aluminum are attached to a piece of angle aluminum that sits on the floor. Two 3/8 inch bolts hold this piece of angle aluminum, and thus the electric motor, to the floor by screwing into anchors in the concrete. The 3/8 inch motor shaft is attached to the 3/4 inch stainless steel shaft by a flexible jaw type coupling. The 3/4 inch shaft passes through the pilot bearing, through the 14 channel slip rings and into a 4 x 4 x 1 inch thick piece of aluminum bolted to the bottom of the circular spin table. This square piece of 1 inch thick aluminum has a 3/4 inch hole drilled through its center. The shaft fits into this hole and butts up against the bottom of the table. Two set screws 90° apart keep the shaft from turning inside the hole.

The 14 channel slip ring assembly is manufactured by Superior Carbon Products,

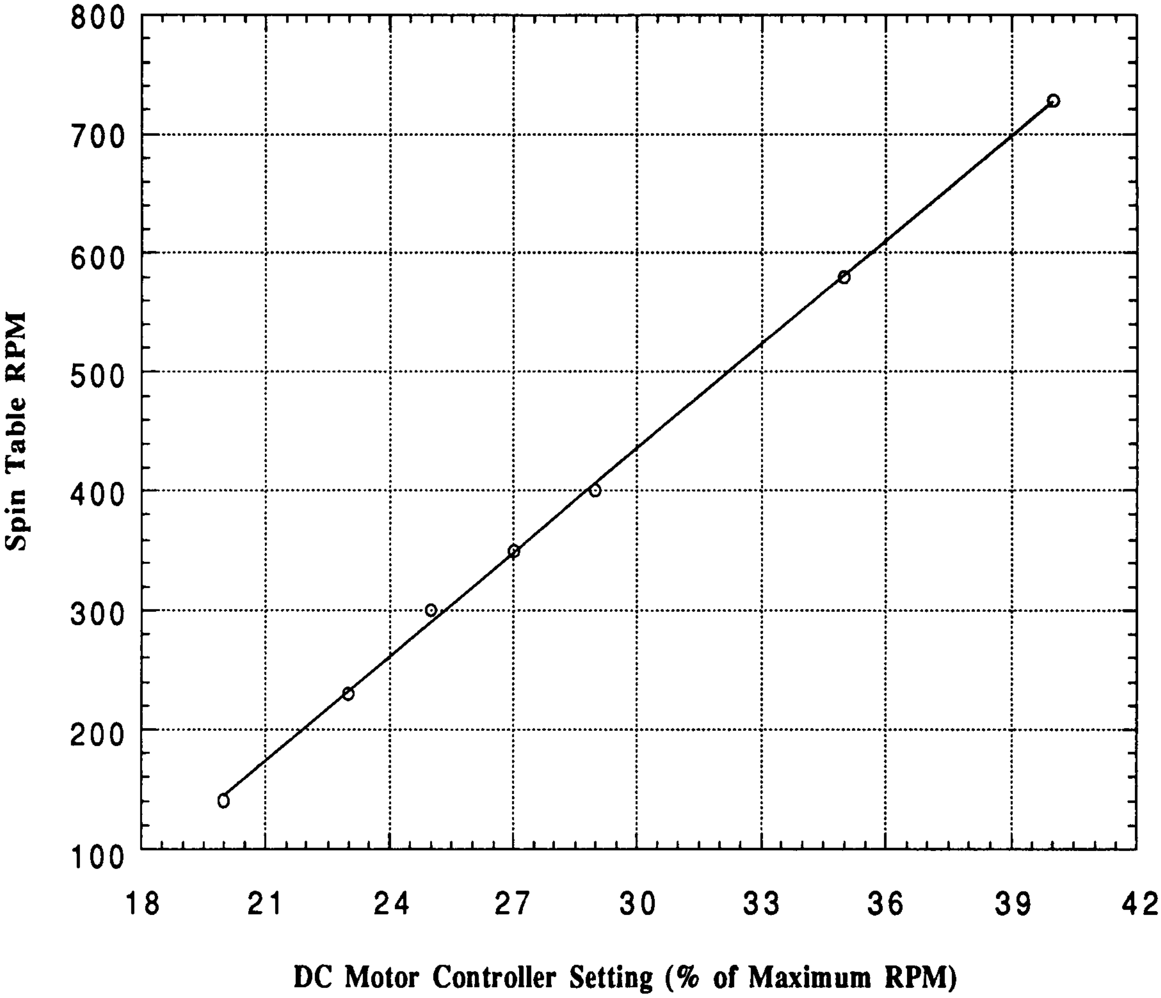

Figure 14. Spin Table RPM vs. DC Motor Controller Setting

Inc. , part number SK-2536-14. It has a 2.0 inch outside diameter and is 4.06 inches in overall length. It came with an insert to fit snugly on the 3/4 inch shaft. The rings are made of coin silver and have silver graphite brushes (2 per ring). The unit is rated at up to five amps and 220 volts with a 5000 rpm maximum speed. The rings are held to the shaft by two set screws 90° apart. Parts had to be made to hold the brushes at the right height , to line up with the rings, and at the right distance from the rings.

The spin table is 3/8 inch thick, 24 inches in diameter and is made of aluminum. On top of this table is the 1/4 hp electric motor, the solid rocket motor assembly and the flexure assembly. The rocket motor is spun about its axis of symmetry by a 1/4 hp electric motor manufactured by Marathon Electric, Catalog number S126. This motor rotates at 1725 rpm and is not speed controllable. Power for this motor passes through the 14 channel slip ring unit. The electric motor shaft is connected to the rocket motor assembly by a flexible jaw type coupling. On the connecting shaft is a four channel slip ring unit. Two of these channels are used for the 12 V power supply to the igniter. The other two channels were used in previous experiments for measuring the combustion chamber pressure with a Kistler transducer. There is a port at the head end of the combustion chamber for the transducer. Pressure was not measured during the current tests and so the port was sealed off.

The horizontal electric motor and rocket motor assembly sit on a 9 x 9 x 3/8 inch thick piece of aluminum. This piece sits about 3/4 inch above the spin table. Two sides of this square plate are each attached to a 9 3/4 inch long by 1/4 inch thick by 1 1/2 inch tall piece of aluminum. The four corners of these two pieces are attached to one end of the four flexures. The 0.05 inch thick flexures fit into 3/8 inch deep slots at each end and are held in place by six 10-32 screws per flexure. The outside end of the flexures (outside referring to the outer radius from the table center) are attached to another piece of 1/4 inch thick aluminum. This piece is attached to a larger block of aluminum that has two

3/8 inch screws per corner that go into the spin table. So the only part that touches the top of the table are the four corner blocks. The flexures are 1/8 inch above the table. The moment caused by the side force in the rocket motor will cause the 9 x 9 x 3/8 inch piece of aluminum to move, causing the four flexures to move. Strain gages mounted on the flexures can pick up this movement and the magnitude and direction of the side force can be determined. Detailed drawings of the flexure assembly can be found in Appendix B.

The flexures were sized so that they are responsive to the magnitude of the side forces anticipated to be generated by the rocket motor, and are also strong enough to handle the thrust of the rocket. In analyzing the amount of strain anticipated in the flexures, they were treated as cantilever beams, one side fixed and the other side moving.

DATA ACQUISITION SYSTEM

The main components of the data acquisition system consist of strain gages, strain gage input modules, an analog to digital (A/D) board and a Macintosh II ci computer with data acquisition software. A video camera, VCR and TV monitor are also used. The data acquisition system was put together specifically for the current tests but can be used for a wide variety of experimental research.

Strain gages are mounted on two of the four flexures. The gages on one of the flexures is used to measure the thrust of the rocket motor, and the strain gages on the other flexure is to measure the side force produced by the rocket motor. Four strain gages are affixed to each flexure in a full Wheatstone bridge arrangement. The benefit of a full bridge is that it provides the maximum sensitivity and resolution (compared to 1/4 or 1/2 bridges) and it is temperature compensated. For both axial and bending strain, two of the four gages are attached to each side of the flexure. To measure bending strain only, all four gages are aligned in the same direction, whereas to measure axial strain, on each side of the flexure the two gages are perpendicular to each other. It is important to be sure that the four gages are wired to each other properly.

All the strain gages used were purchased from the Micro-Measurements Division of Measurements Group, Inc. The gages used to measure bending are part number CEA-13-125UW-350. These are general purpose gages with large solder tabs for easy wiring. They have a resistance of 350.0 ± 0.3% ohms and a gage factor of 2.15 ± 0.5%. The gages used to measure thrust are part number CEA-13-125UT-350. These come as a 2-element 90° "tee" rosette. One of these rosettes is on each side of the flexure. They have a resistance of 350.0 ± 0.4% ohms and a gage factor of 2.15 ± 1.0%.

Each strain gage bridge circuit needs to have a power supply. This is accomplished using Analog Devices Inc. 5B38-02 strain gage input module. There is one of these modules for each full bridge. The strain gage module provides +10 V excitation to the bridge and then accepts the output signals from the strain gages. It takes the output signal, filters it and then amplifies it to ±5 V. Each strain gage bridge uses four channels of the 14 channel slip ring unit; two channels for the ± excitation voltage and two channels for the ± output signal. Specifications for the strain gage modules can be found in Appendix C.

The strain gage modules plug into a 16 channel 5B01 backplane also by Analog Devices Inc. This backplane can accept a wide variety of plug-in input and output modules. Each channel has four screw terminals for connecting to the sensors. This backplane requires an external +5 V power supply. The backplane connects to a compatible data acquisition A/D board. Details and specifications for the 5B01 backplane can also be found in Appendix C.

The 5B01 backplane plugs into a GW Instruments, Inc. MacADIOS II 5 µs A/D board. The MacADIOS II card is installed in one of the Macintosh II ci's expansion slots. This 12-bit A/D board provides 16 analog input channels, two analog output channels, eight digital input channels, eight digital output channels and three counter/timer channels. For our application only two of the 16 analog input channels are used. Full details and specifications for the MacADIOS A/D board can also be found in Appendix C.

Although the MacADIOS II includes some basic software to view and record data, a separate software package was used. The data acquisition software used is GW Instrument's SuperScope. SuperScope controls the data acquisition mode, creates and displays waveforms and essentially runs the experiment. SuperScope displays and records the strain gage's output voltages.

STRAIN GAGE CALIBRATION

Since the data acquisition system only records the voltage output of the strain gages, it is necessary to know the corresponding force that goes with the voltage. With the test stand still, the strain gages give an initial "baseline" output voltage. Forces can then be applied to the structure, such as by pushing with your hand, and after the load is lifted the strain gages return to the baseline voltage. By applying known weights in the proper direction (bending or axial) a curve can be constructed giving the strain gage output voltage for the corresponding applied force.

To simulate the side forces that are caused by the rocket motor, weights were applied to the motor in a pulley-type arrangement. This was done in both the damping and driving directions. Figure 15 shows these directions. Figure 16 shows schematically how the weights were applied. A round rod was fixed to the spin table so that the top of the rod was even with the middle of the rocket motor. Fishing line was tied around the motor, hung over the rod and weights were tied to the line. Weight was added in 0.1 lb increments from zero to 2.1 lbs. This was done in both the damping and driving

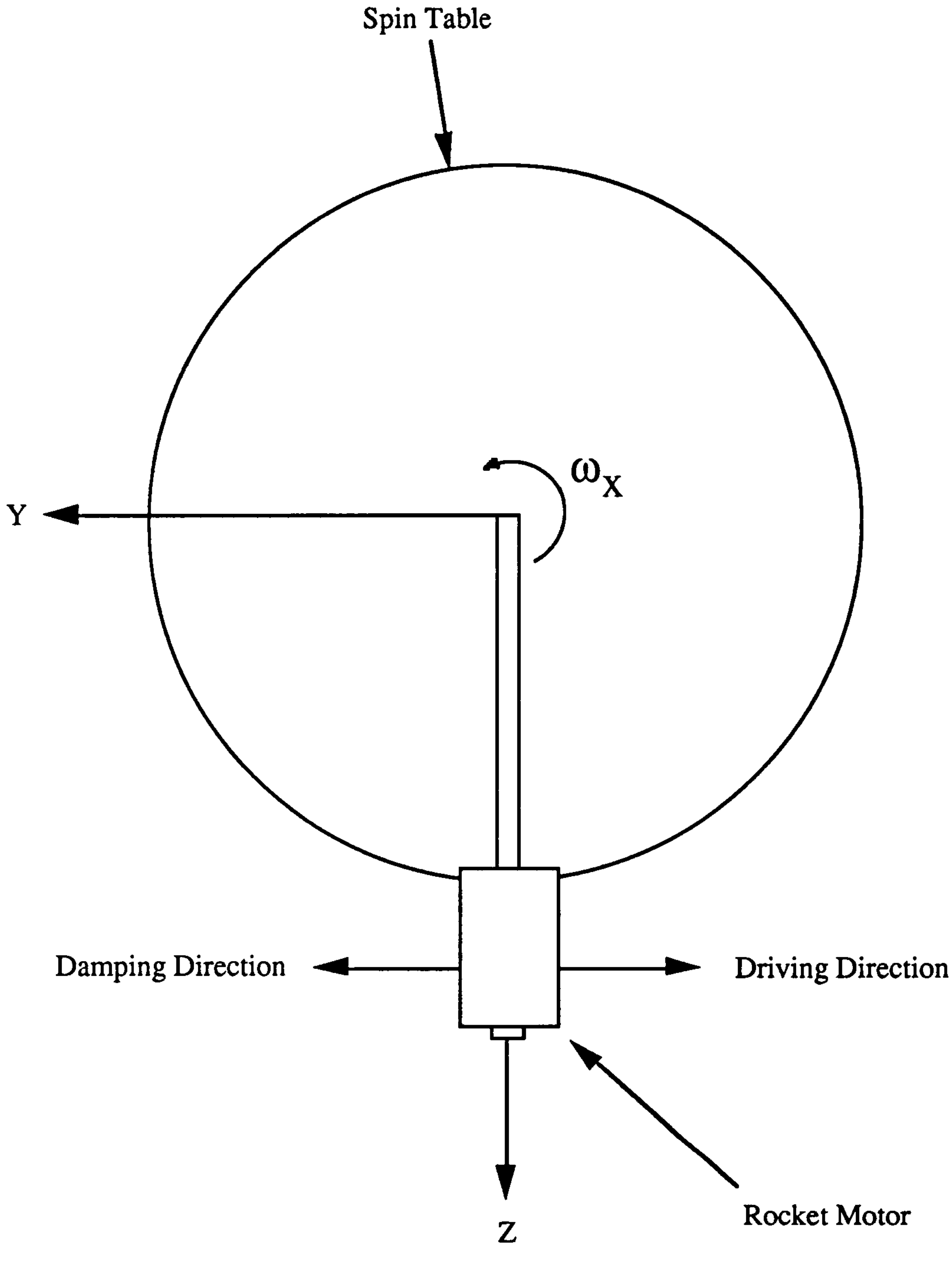

Figure 15. Schematic Showing Damping and Driving Directions
(Top View of the Spin Table)

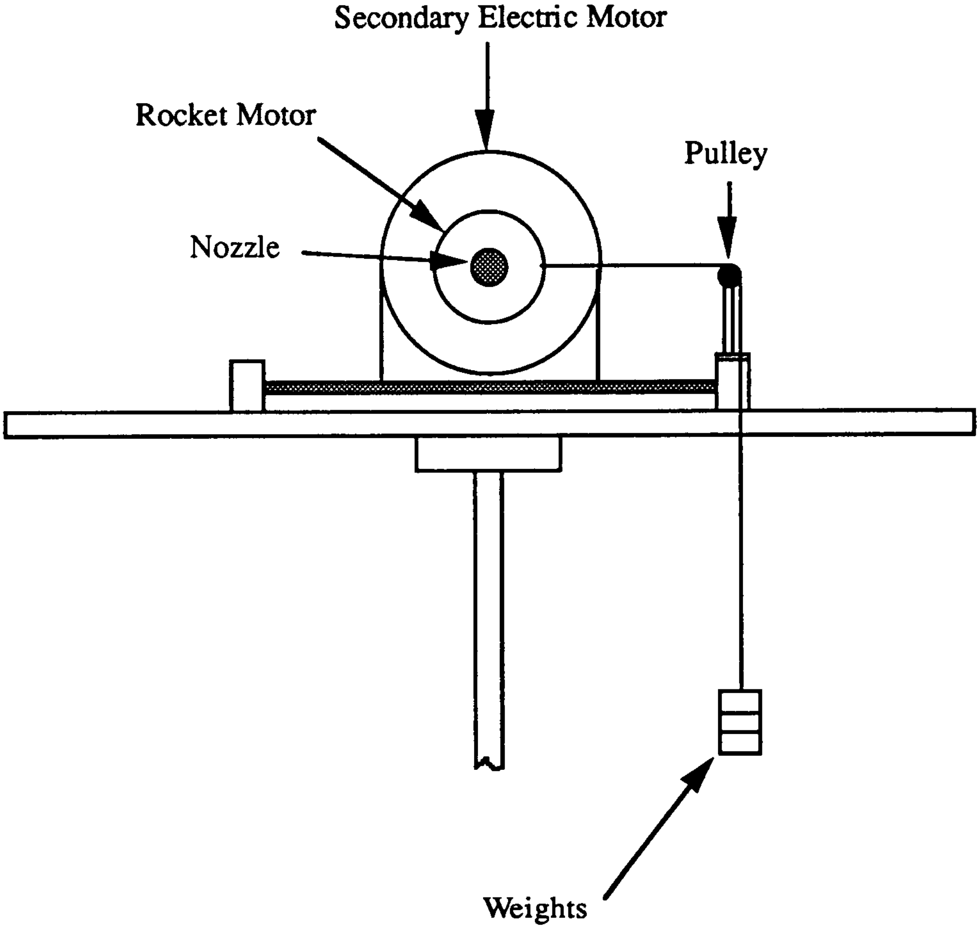

Figure 16. Calibration Set-Up for Bending Direction
(Driving Direction Shown)

directions. Figure 17 shows the calibration curves for the bending direction. No weight corresponds to zero voltage. Actually, zero weight has some baseline voltage associated with it, but this was subtracted from all the voltages so that zero weight applied corresponds to zero volts. The curves show a linear relationship between sideforce and output voltage.

The strain gages were also calibrated in the axial direction (thrust) in a similar manner. A pulley was fixed to a table at the same height as the rocket motor centerline. A nylon rope was tied to the motor assembly, hung over the pulley and weights were tied to the rope. A schematic of this arrangement can be found in Figure 18. Weight was added from zero up to 55 lbs. This calibration curve can be found in Figure 19. The data points are a little more scattered than in the bending direction, but are still fairly linear.

With this information it should be possible to determine the direction and magnitude of the sideforce in the rocket motor, as well as the thrust. The shown calibration curves were done before the first motor firing. The calibration process should probably be done after each motor firing to get the best possible results.

TEST PROCEDURE

Running a test is a relatively straightforward process and will be described later in this section, but first some of the problems encountered in readying the test stand for actual firing will be discussed.

The data acquisition system was initially checked out with neither of the electric motors running. Then the secondary motor was turned on and then the primary motor was turned on, although very slowly at first. With no electric motors on, the strain gages show a smooth trace on the computer screen. When the secondary electric motor is turned on, the output becomes a sine wave-like trace. This only occurs in the bending

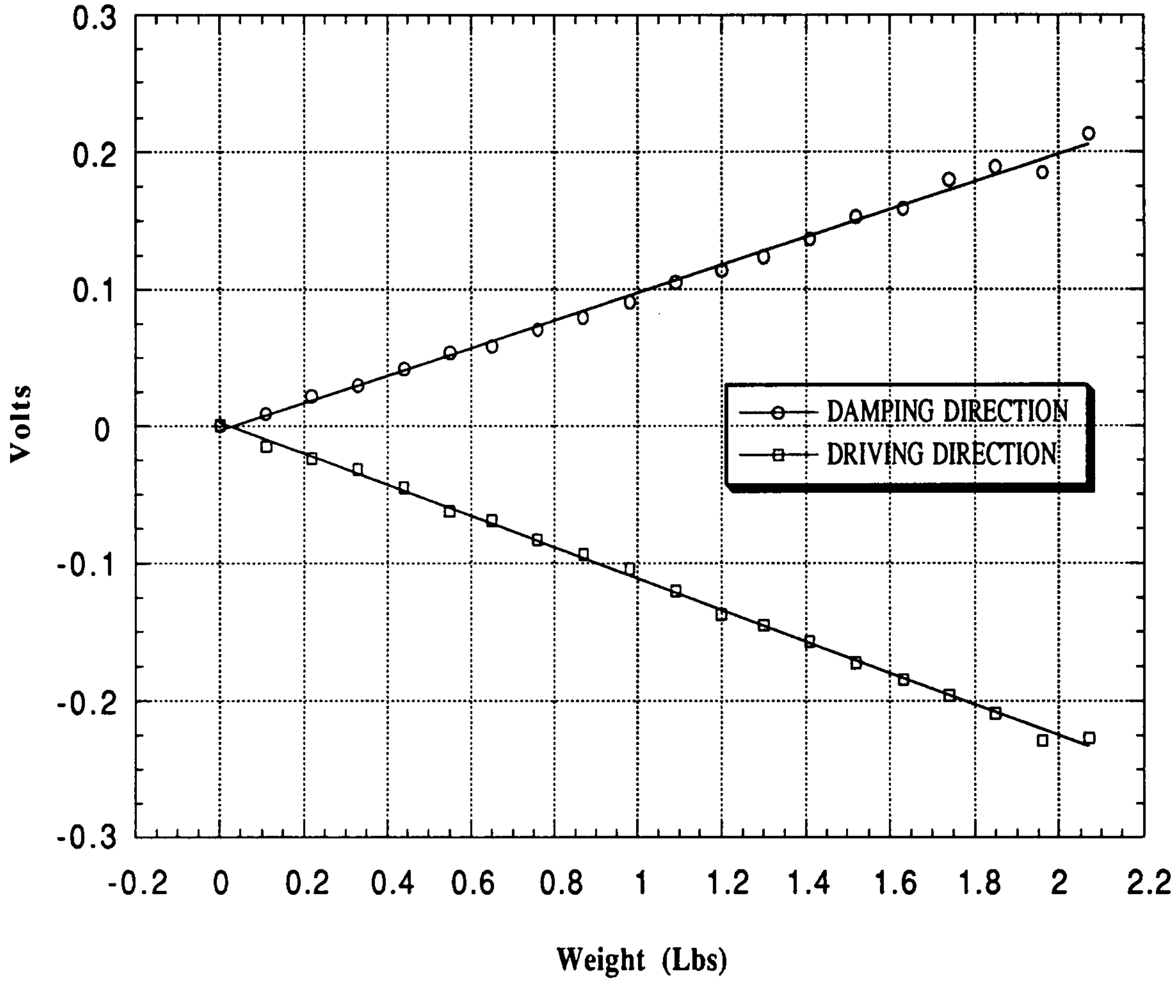

Figure 17. Strain Gage Output Voltage vs. Calibration Weight (Bending)

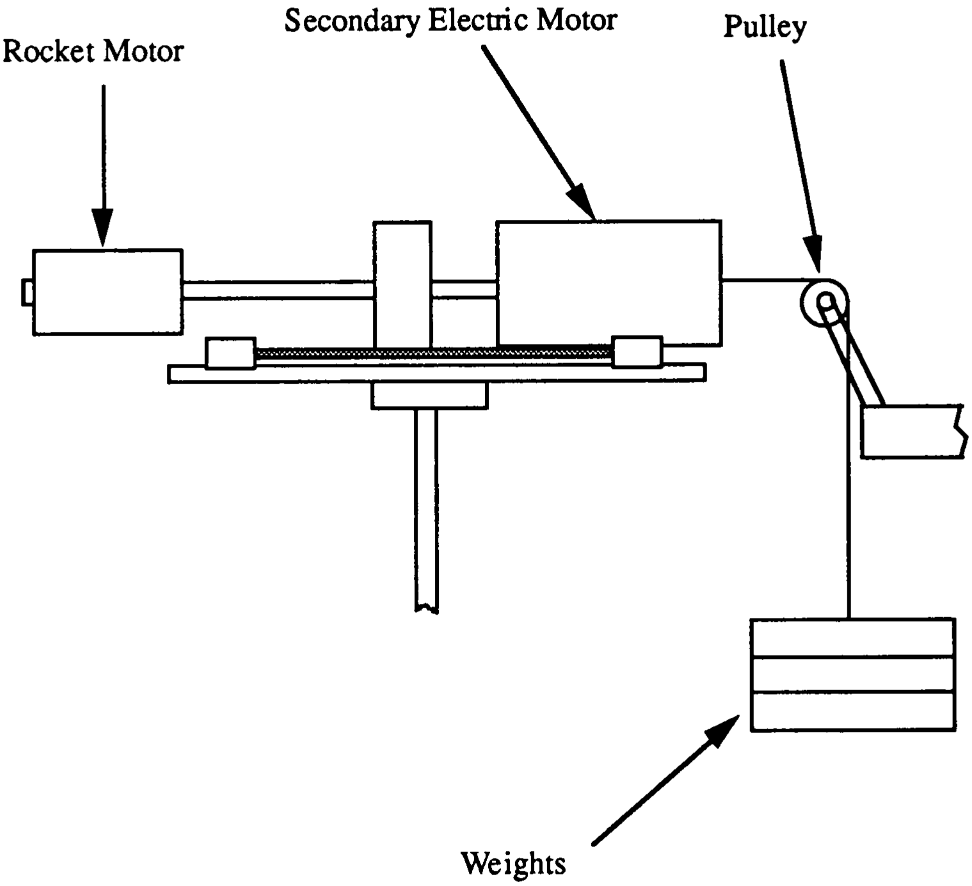

Figure 18. Calibration Set-Up for Axial Direction

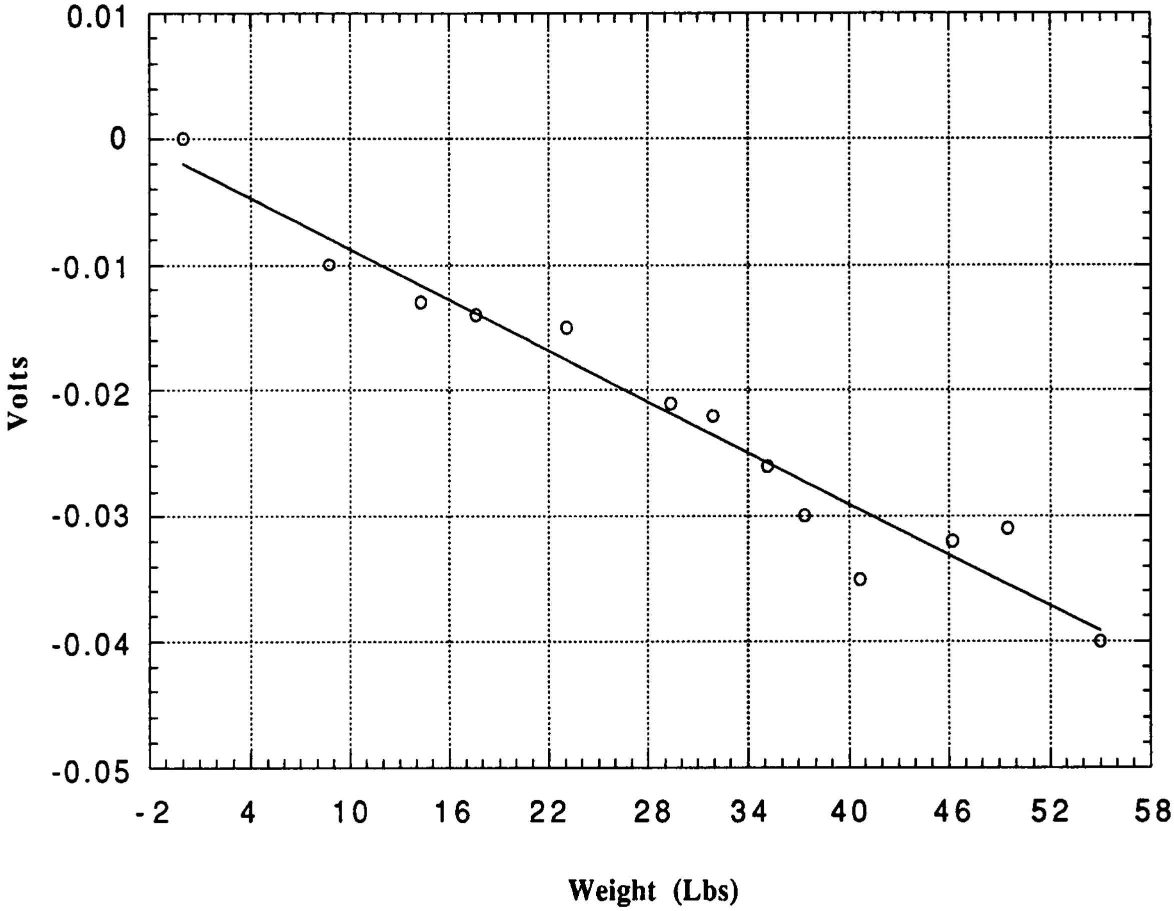

Figure 19. Strain Gage Output Voltage vs. Calibration Weight (Thrust)

channel so it is probably due to an unbalance in the spinning parts, as opposed to electrical noise. When the primary motor is turned on and the table is spinning, the output in the bending channel becomes even more chaotic, and becomes worse as the table rpm is increased. In fact, when the table rpm was brought up to about 300 rpm the legs of the test stand could be seen to shake. Obviously the table was out of balance. All of this occurred without the rocket motor firing. If nothing was done to balance the table, the forces that are trying to be isolated will be "drowned out" in the vibrational noise.

The table was then professionally balanced at 400 rpm. This was done with a 3.0 inch motor installed as if it were ready to fire. The table balance is very sensitive to small changes in mass at this rpm range. This brings up the problem of the mass loss during the rocket motor burn. Even thought the table is balanced at the beginning of the burn, it will be getting more and more unbalanced as the motor burns. The more unbalanced it gets, the more vibration will appear and the strain gages will pick up this unwanted movement. One idea to alleviate this problem is to have a weight on the spin table that moves during the burn to compensate for the mass being lost, but nothing has been done yet to address this problem.

During the balancing process it was noticed that the secondary electric motor (the 1/4 hp horizontal motor on the spin table) was smoking and making unusual noises. The first problem identified was that the internal cooling fan was being pushed into the motor windings. This was apparently due to the centrifugal forces on the motor as a result of it being spun around on the spin table. The rotor assembly was wanting to push out of the top of the motor. This was fixed by tightening a homemade screw device up against the top of the motor to keep the parts from moving outward. But this was only one of the problems. The other problem was that the motor was trying to run on both its starter windings and its main windings. It seems that a centrifugal switch inside the motor was staying closed when it should be open. This too is due to the centrifugal forces on the motor. This problem was fixed by disconnecting the starter windings. So now to start the motor, the power switch has to be turned on and the motor spun by hand fast enough so that it will run off of the main windings. Looking at the nozzle exit, the assembly is spun counterclockwise to start the motor. The motor can be spun in either direction and it will run in that direction, but the table was balanced with this motor spinning counterclockwise. A new electric motor was considered, but the same problems were likely to arise. Also, a new motor would require the table to be rebalanced.

The actual test procedure will now be discussed. SuperScope can be configured and saved so that all that is required to begin data acquisition is to click on the start button. The user opens the appropriate channels, creates waves, indicates what waves are to be displayed and how to save the information. There are four modes of data collection: oscilloscope, chart, scan and scroll. Scan mode is used for the tests. In scan mode, SuperScope can sample at a maximum rate of 14k samples/sec for one channel, and 14/n k samples/sec for n channels. For our tests data was sampled at 100 points/sec. In scan mode the input channels are displayed during data acquisition and an experiment is typically collected in one trace.

Each test is carried out in two steps. The first step is to install a rocket motor (minus the igniter) and do a "dry" run. With both motors spinning at the speeds the actual test will be run, data is recorded, typically for six seconds (600 data points). This data will be used to compare when the motor is actually firing.

To fire a rocket motor the procedure is as follows. Just before a rocket motor is to be fired, the exposed propellant surface should be carefully scraped away. This surface is aluminum oxide that forms when the propellant is exposed to air and may hinder the propellant from igniting. A baggie igniter is then placed inside the combustion chamber and the rocket motor assembly is put together. The igniter leads stick out of the nozzle. Making sure that the 12 V battery is disconnected, the igniter leads are wired. The only other thing needed to be done inside the test bay is to manually start the secondary electric motor. This requires two people. One person to turn on the power switch and the other to hold on to the rocket motor assembly and give it a spin to start the electric motor. The video camera and VCR are also turned on so that the test can be monitored in the control room and viewed later.

In the control room the 12 V battery is connected, making sure the ignition switch is in the off position. Now the other electric motor is turned on and brought up to the desired speed. With the data acquisition software already set up ahead of time, the only thing left is to start the data acquisition and hit the ignition switch to fire the rocket. The data acquisition begins by clicking the cursor on the start button on the screen. After making sure the data is being recorded, the rocket motor is ignited. When the ignition switch is turned on the baggie igniter essentially vaporizes and is blown out of the nozzle. After the rocket fires, the electric motors are turned off and the assembly is allowed to cool. The rocket motor casing can then be removed and the accumulation of any aluminum oxide slag can be examined.

Since both the jet damping moment and the moment that drives the coning instability are proportional to the transverse angular velocity, it would be beneficial to rotate the spin table as fast as possible. The faster the table is spinning, the larger the forces are that will be measured by the strain gages. The primary electric motor has the capability to rotate the table from 140 rpm up to around 1700 rpm. Unfortunately it is doubtful if the test stand, as it exists, will be allowed to go faster than around 600 rpm. Even though the table was professionally balanced, there is still enough imbalance and structure flexibility in the system to cause vibrational problems at higher rpms. These vibrations are picked up by the sensitive strain gages and any useful data would be lost. The plan for the testing program is to begin at lower rpms (say 300 rpm) and slowly increase the table speed with each firing.

IV. RESULTS AND DISCUSSION

The first rocket motor firing occurred on May 19, 1993. Unfortunately, due to a mishap, some of the hardware was damaged and could not be repaired in time to perform more firings during the time constraints of this thesis. As soon as the hardware is repaired, the testing program is expected to continue. The data and description of the malfunction of the first firing will be discussed later in this section. But first some theoretical results on the characteristics of the aluminized solid rocket motors will be given.

THEORETICAL RESULTS

To aid in the design of the test stand and to compare to the experimental results, some theoretical results were computed for the three different length aluminized rockets. Motor characteristics such as mass flow rate, thrust, chamber pressure and specific impulse were calculated. Mass flow rate is given by,

$$\dot{m} = r_b \rho_p A_b \tag{27}$$

where r_b is the propellant burn rate, ρ_p is the propellant density and A_b is the propellant burn area. The burn rate is assumed to be a constant 0.24 in/sec (0.02 ft/sec). The propellant density is 3.36 slug/ft^3 and the burn area changes with time as the propellant is consumed. Figure 20 show mass flow rate vs. time for the three motor lengths.

Also calculated is combustion chamber pressure. Chamber pressure can be found using,

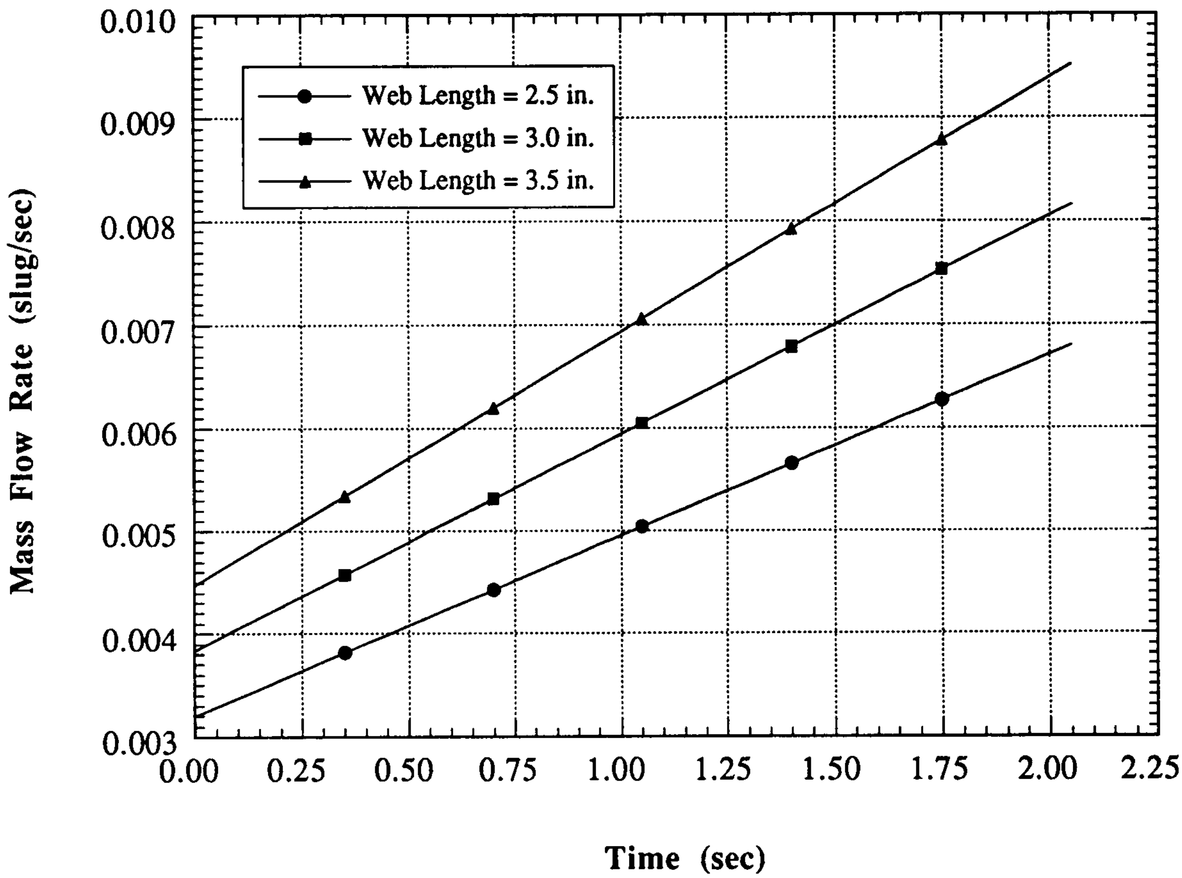

Figure 20. Mass Flow Rate vs. Time for 2.0 Inch Rocket Motors

$$P_o = \frac{A_b}{A_t} \frac{\rho_p r_b \sqrt{R T_o}}{\sqrt{\gamma \left[\frac{2}{\gamma + 1}\right]^{\frac{\gamma+1}{\gamma-1}}}} \tag{28}$$

where A_b is the burn area, A_t is the throat area, ρ_p is propellant density, r_b is burn rate, R is the gas constant, T_o is chamber temperature and γ is the specific heat ratio of the combustion gases. T_o is taken to be 3460 °R, γ is 1.18 and R is 2264 ft lbf/slug °R. Figure 21 shows chamber pressure vs. time for the three motor lengths. Thrust is found using,

$$T = \dot{m} V_e + (P_e - P_a) A_e \tag{29}$$

where V_e is the nozzle exit velocity, P_e is exit pressure, P_a is ambient pressure and A_e is exit area. Assuming isentropic flow relations, Figure 22 shows theoretical thrust vs. time for the rocket motors. Specific impulse is also calculated,

$$I_{sp} = \frac{\text{Thrust}}{\dot{m} g} \tag{30}$$

where g is the acceleration of gravity at sea level. Figure 23 shows I_{sp} vs. time for the rocket motors.

EXPERIMENTAL RESULTS

As mentioned before, the first rocket firing on May 19, 1993, resulted in some damage to the rocket motor assembly. The motor fired was a 3.0 inch long aluminized

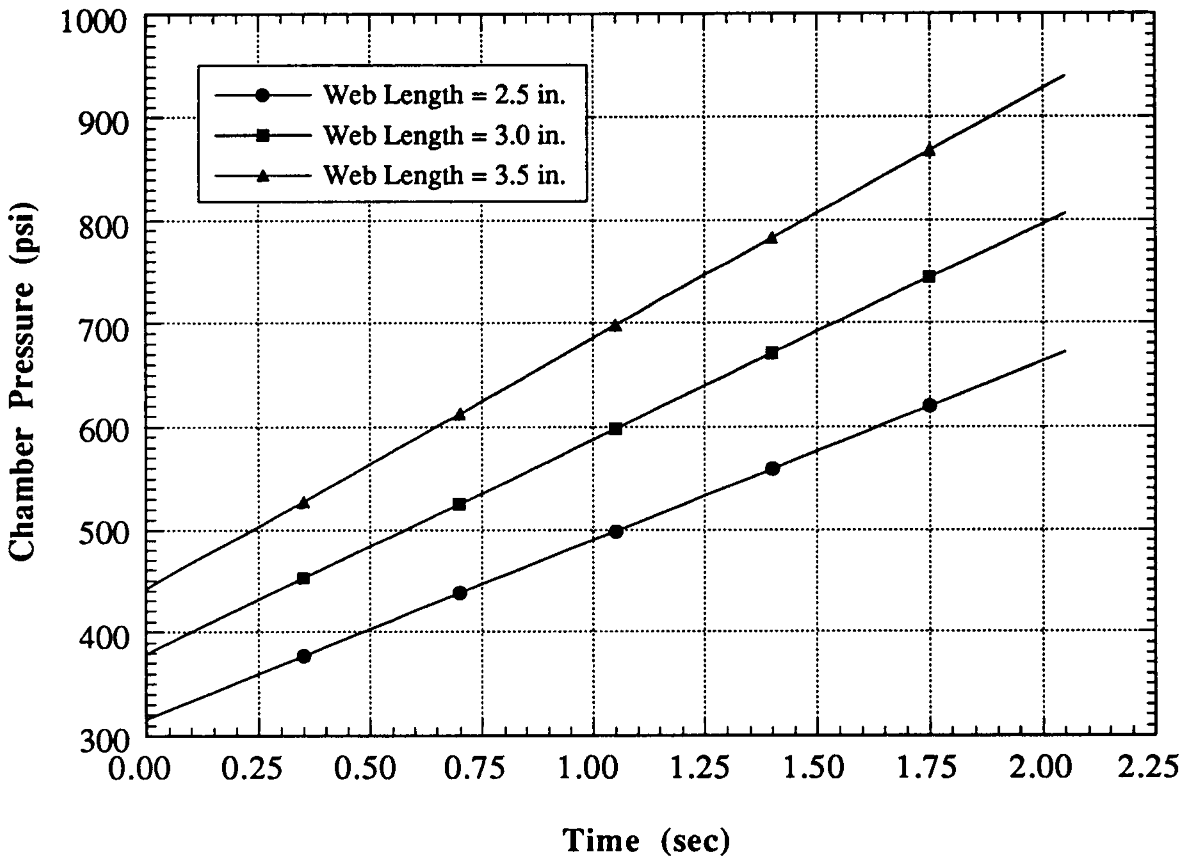

Figure 21. Chamber Pressure vs. Time

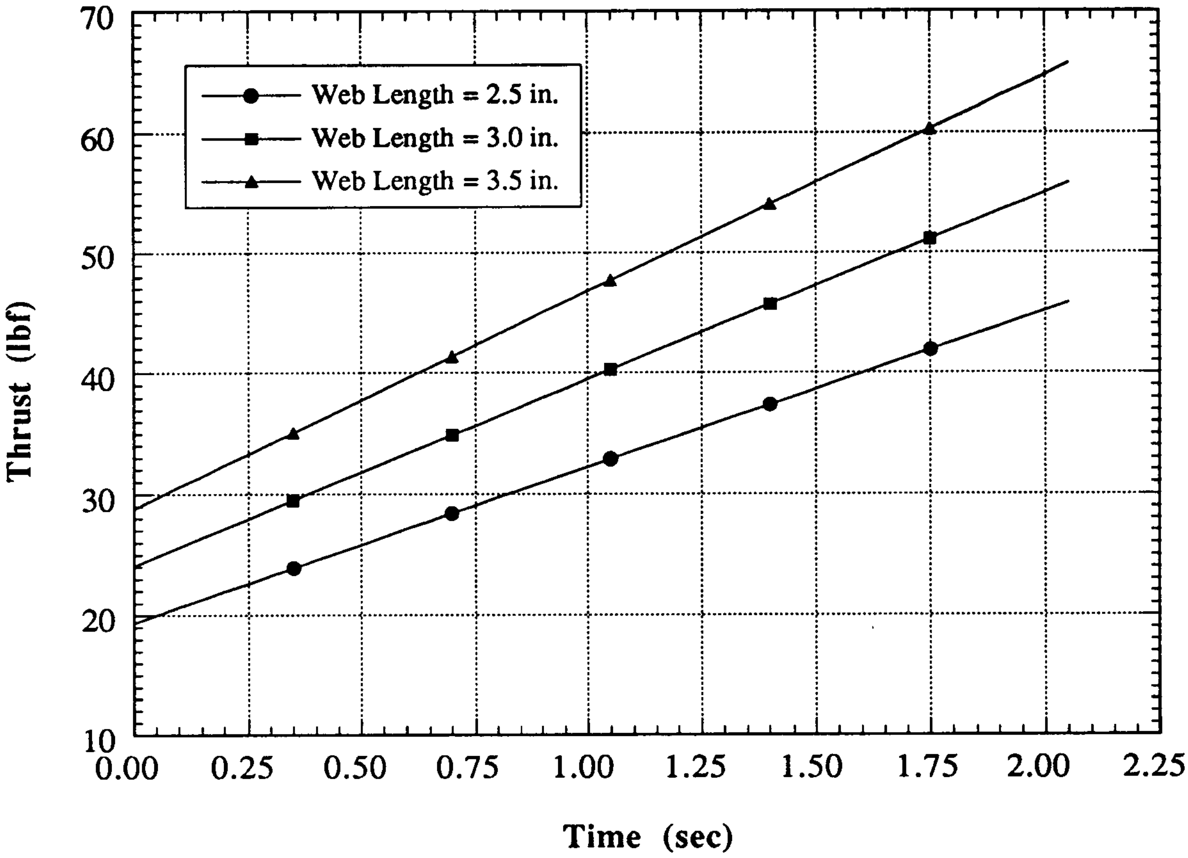

Figure 22. Thrust vs. Time

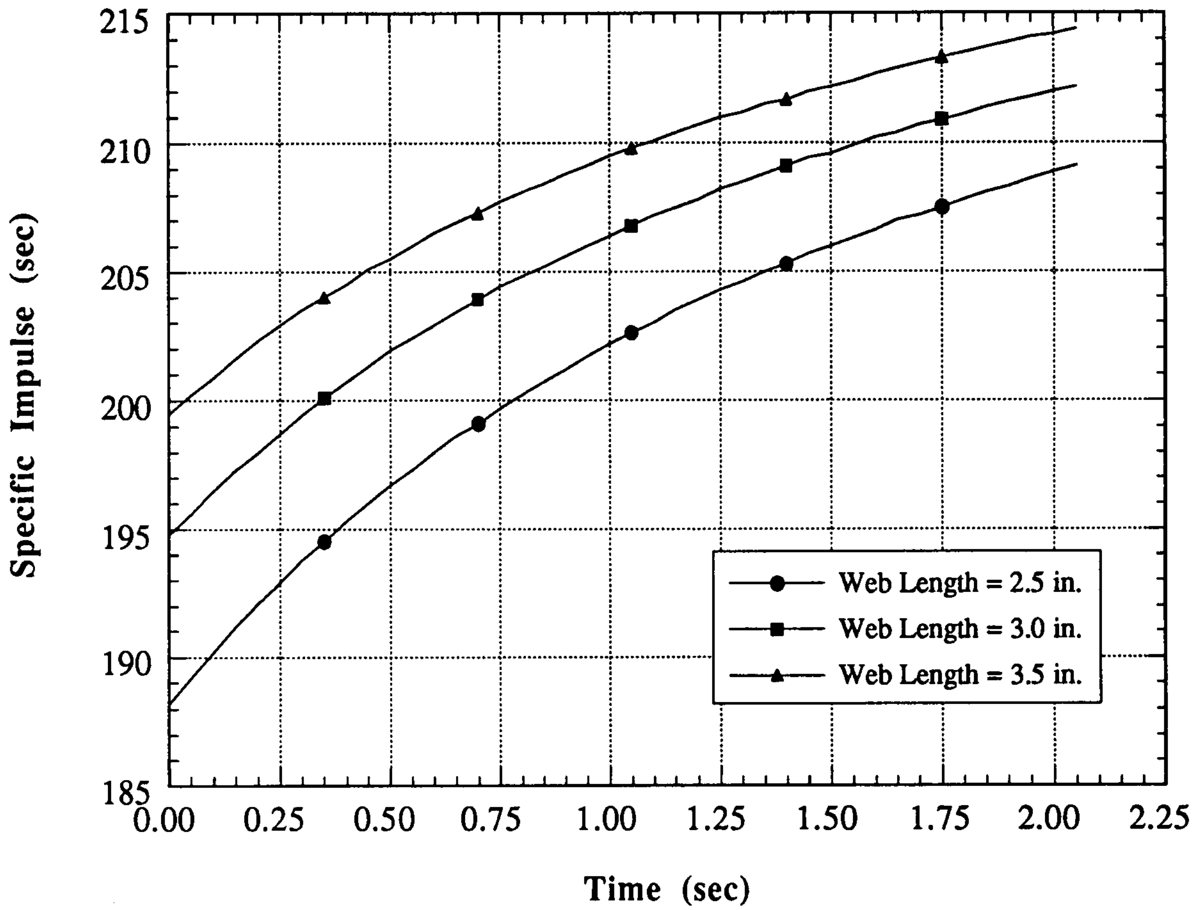

Figure 23. Specific Impulse vs. Time

propellant motor (Number E3111-08 S/N 9). The spin table was rotating at 300 rpm and the secondary electric motor was spinning at 1725 rpm. Approximately 1/2 second into the motor burn, exhaust gases could be seen blowing past the head end O-ring, becoming increasingly worse toward the end of the motor burn. The O-ring apparently failed as a result of overtightening of the motor assembly. This leakage of high pressure hot exhaust gas melted a portion of the stainless steel sleeve the rocket motor fits in, as well as the 0.5 inch spacer that sits on top of the motor and the head end piece that contains the O-ring. The first rocket firing can be seen in Figure 24. The damaged parts were replaced, but could not be readied in time to fire more rockets before the thesis deadline.

There was some difficulty igniting the rocket motor. The first attempt at ignition was using 1 gram of $BKNO_3$ in the baggie igniter. The exposed surface of the propellant was lightly scraped off prior to the ignition attempt. With both electric motors spinning at the desired speed, the ignition switch was turned on. The igniter appeared to perform properly, but the rocket motor did not ignite. The rocket motor assembly was then disassembled for a second attempt. This time 2 grams of $BKNO_3$ was used in the baggie igniter and more of the propellant surface was scraped off. This time the rocket motor ignited but with some difficulty. There was an approximately 3 second delay between the baggie ignition and the beginning of rocket motor ignition. The reason for this delay is unknown and has not occurred in testing of similar rockets before.

This long time delay also reduced the amount of useful data that was collected. SuperScope was configured to record for six seconds. The plan was to begin data acquisition, wait a second, and then ignite the rocket, which burns about two seconds. This leaves about three seconds of data acquisition after the anticipated end of the motor burn. With the long delay before the motor started, the data acquisition stopped before the rocket did.

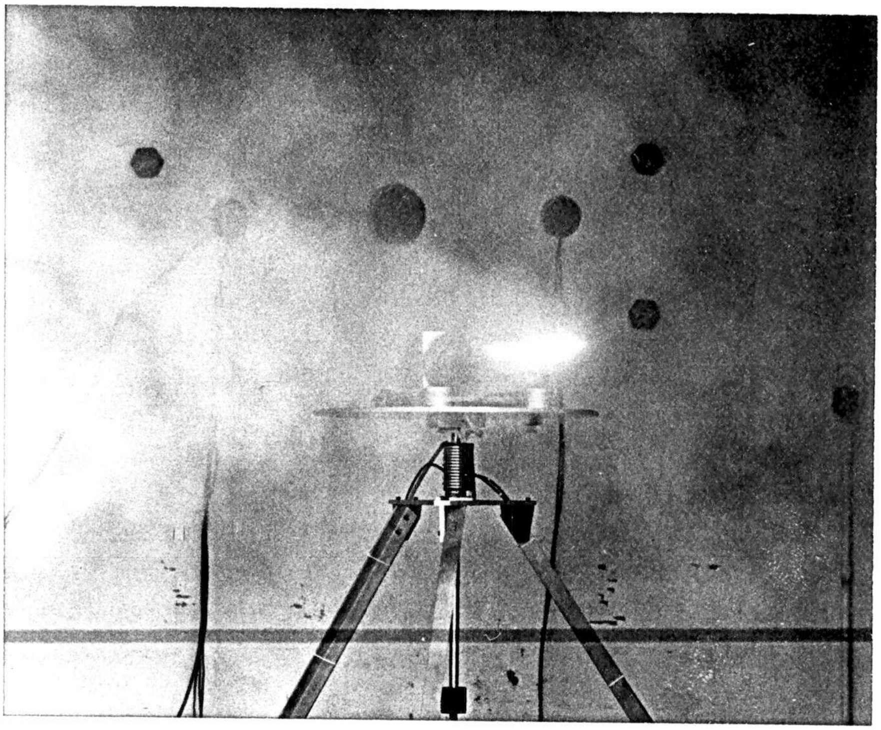

Figure 24. First Rocket Firing of Test Stand

Results From First Rocket Firing

As previously mentioned, each rocket firing takes place in two steps. The first step is to assemble the motor assembly as though it were going to fire (minus the igniter), spin it at the desired speeds and record some data. This data will be used to compare with when the rocket is actually firing. This was done for the first rocket test. Figure 25 shows three seconds of data acquisition from the strain gages that measure in the bending direction. The spin table is rotating at 300 rpm and the secondary electric motor is at 1725 rpm. Notice how the strain gages pick up a regularly reoccurring pattern. This sinusoidal like pattern has a large peak followed by a smaller peak followed by another large peak and so on. The period between two of the similar sized peaks is about 0.2 seconds, which is the time it takes the table to make one revolution at 300 rpm. These deflections are obviously from an unbalance in the table, or from structural flexibility. Even though the table has been balanced as well as possible, the sensitive strain gages pick up these movements in the flexure.

Figure 26 shows three seconds of data acquisition from the thrust channel without the rocket firing. Notice that this data is more chaotic than in the bending channel. Also notice that the voltage deflections for the thrust channel have a much lower magnitude than in the bending channel. The maximum peak to peak amplitude for the voltage values in the thrust channel is 0.117 Volts, whereas in the bending channel, the maximum peak to peak amplitude is 0.874 Volts. This makes sense because the axial strain gages are not sensitive to bending deflections due to imbalances.

With the O-ring failure, any results from the rocket firing pertaining to the jet damping or jet driving question are inconclusive. But an analysis of the data from the first test does show the events that took place. Figure 27 shows the first three seconds of data acquisition in the bending direction for the actual firing of the rocket motor. Notice

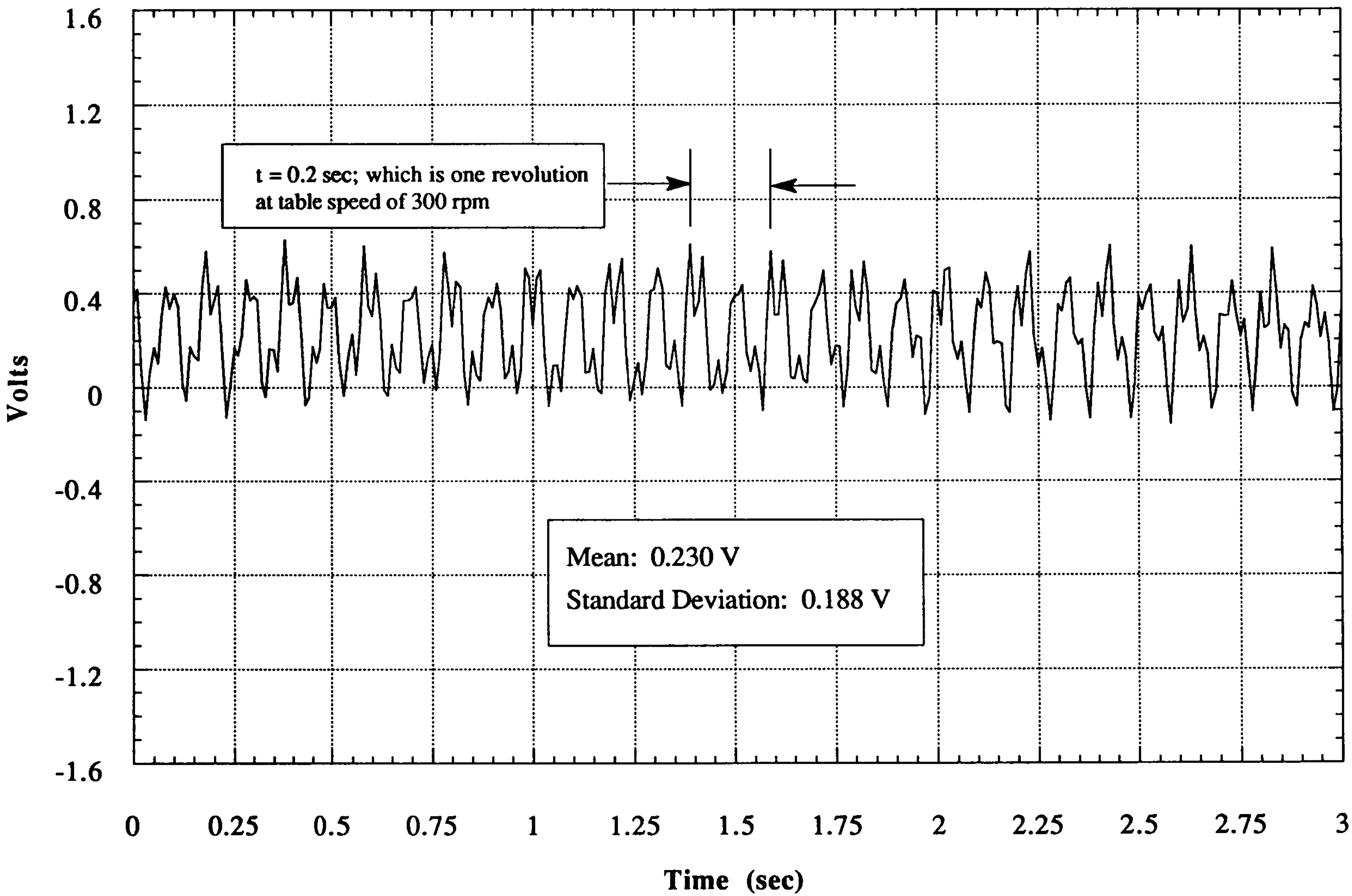

Figure 25. Output Voltage vs. Time (Bending - Before Ignition)

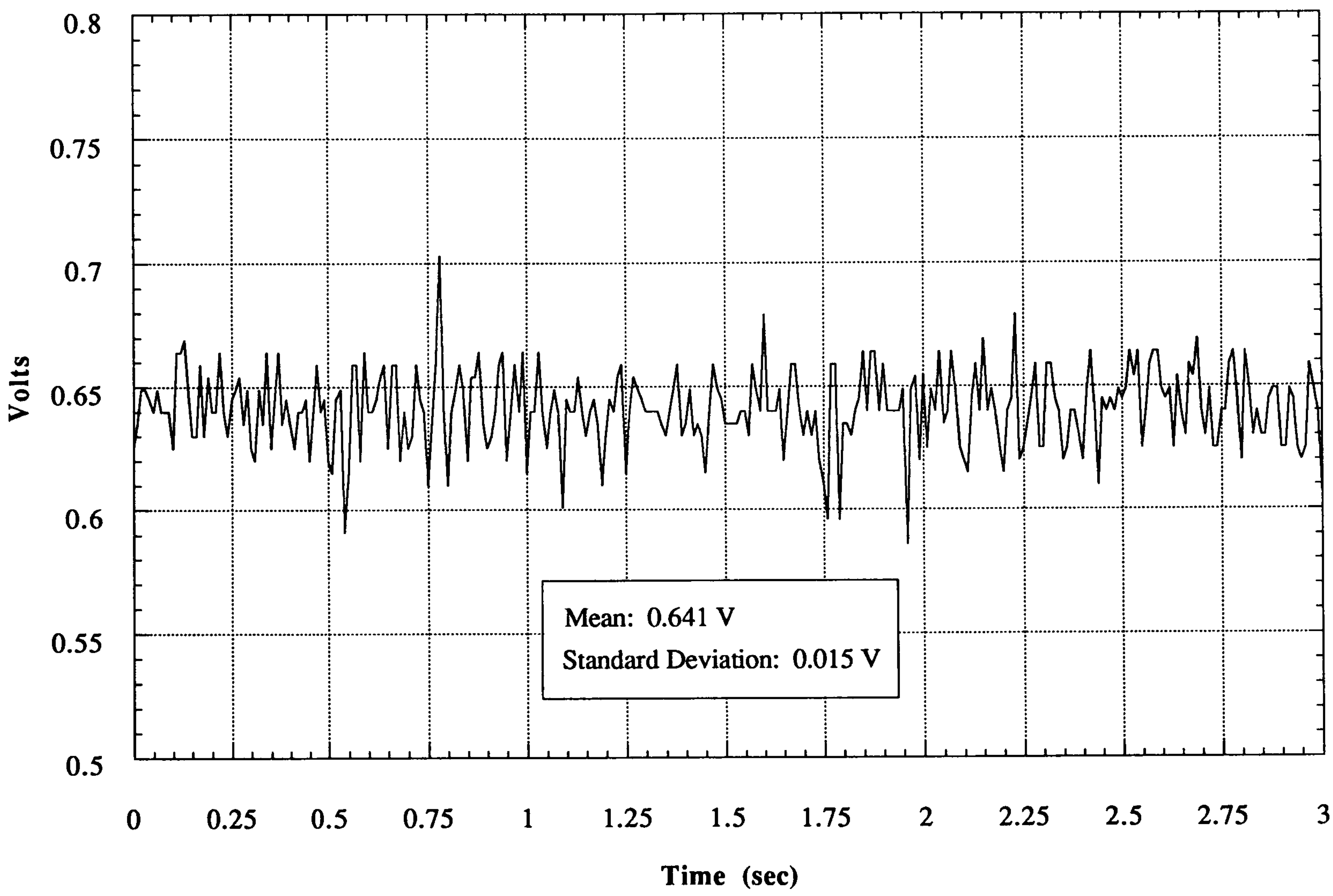

Figure 26. Output Voltage vs. Time (Thrust - Before Ignition)

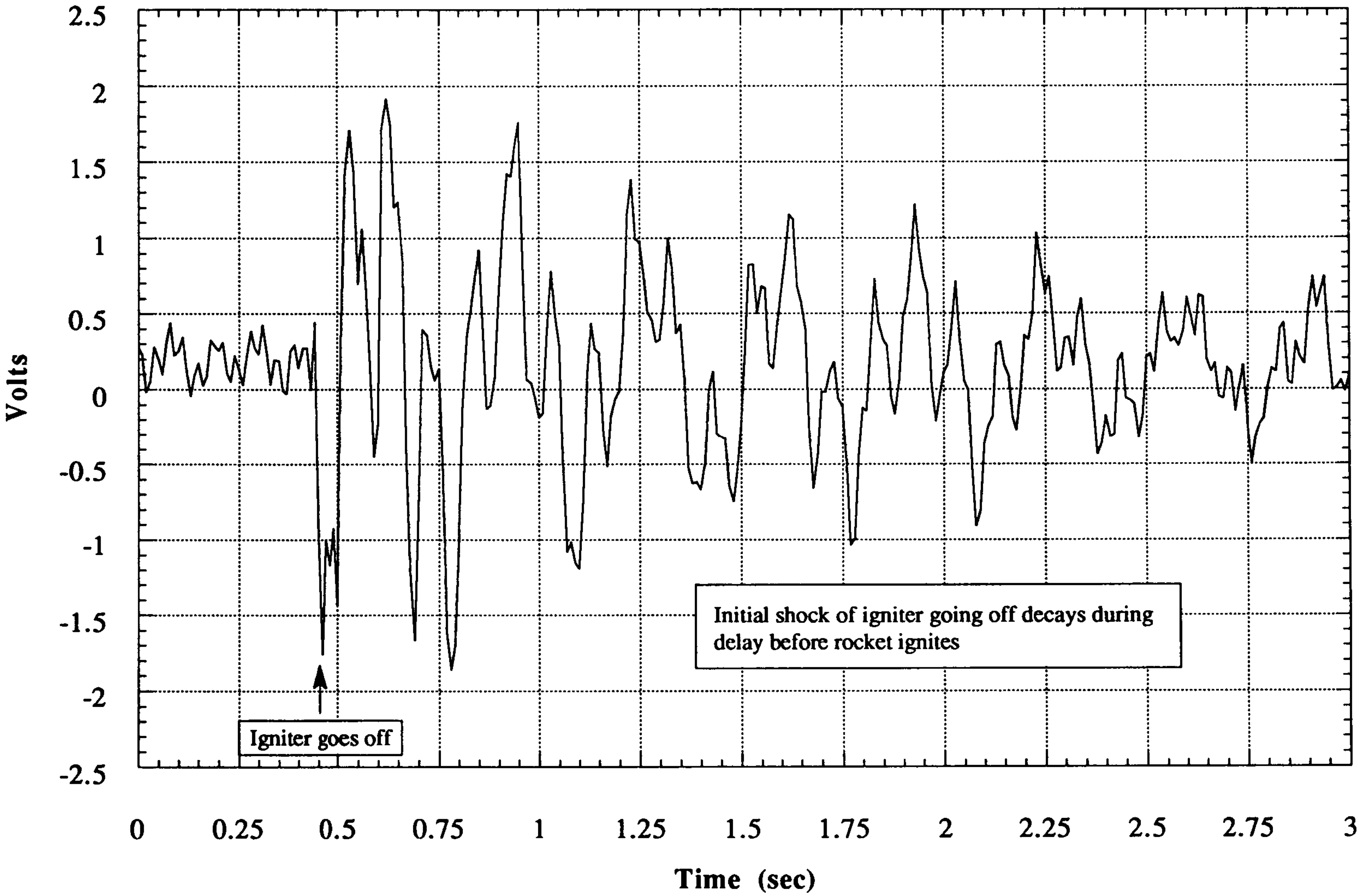

Figure 27. Output Voltage vs. Time for First Three Seconds of Data Acquisition (Bending)

that at about $t = 0.4$ seconds there is a large voltage jump. This is when the igniter goes off. The baggie igniter ignites with an energetic burst and is blown out of the nozzle. After the igniter went off, there was about a three second delay before the solid propellant ignited. Figure 27 shows that after the initial shock of the igniter going off, the deflections subside before the motor starts to fire. The magnitude of the deflections after the igniter went off is of some concern. If the rocket fired immediately after the igniter went off, as it is supposed to do, the residual effects of the igniter "explosion" may drown out the signals due to the side forces generated by the rocket motor.

Figure 28 shows the last three seconds of the six seconds of data acquisition. At about $t = 4$ seconds, the solid propellant begins to burn. At around $t = 4.5$ seconds, the exhaust gases are blowing past the O-ring, causing large side forces. These side forces are also likely due to the increasing unbalance of the table as propellant is consumed.

Figure 29 is the thrust channel for the first three seconds of the first rocket firing. Again the large voltage spikes at $t = 0.4$ seconds is the igniter going off. The rest of Figure 29 is the delay before the rocket ignites. Figure 30 shows the last three seconds of data recorded from the thrust strain gages. At about $t = 4.4$ seconds, the rocket motor is fully ignited and maximum thrust develops as can be seen in the downward shift of the data. The reason for the large voltage spike at about $t = 4.95$ seconds is unknown.

An examination of the rocket motor casing after the first run showed an accumulation of solidified aluminum oxide (Al_2O_3) around the nozzle end of the motor casing. It was desired to take a picture of the inside of the casing showing this accumulation, but this did not happen. Sitting over the weekend, the motor casing mysteriously split up the sides and the aluminum oxide cracked and became very brittle. Since it is doubtful if anyone tampered with the casing, the cracks may have formed as a result of the temperature and humidity of the room in which it was kept. The Al_2O_3 deposits were then carefully removed from the inside of the motor casing and examined.

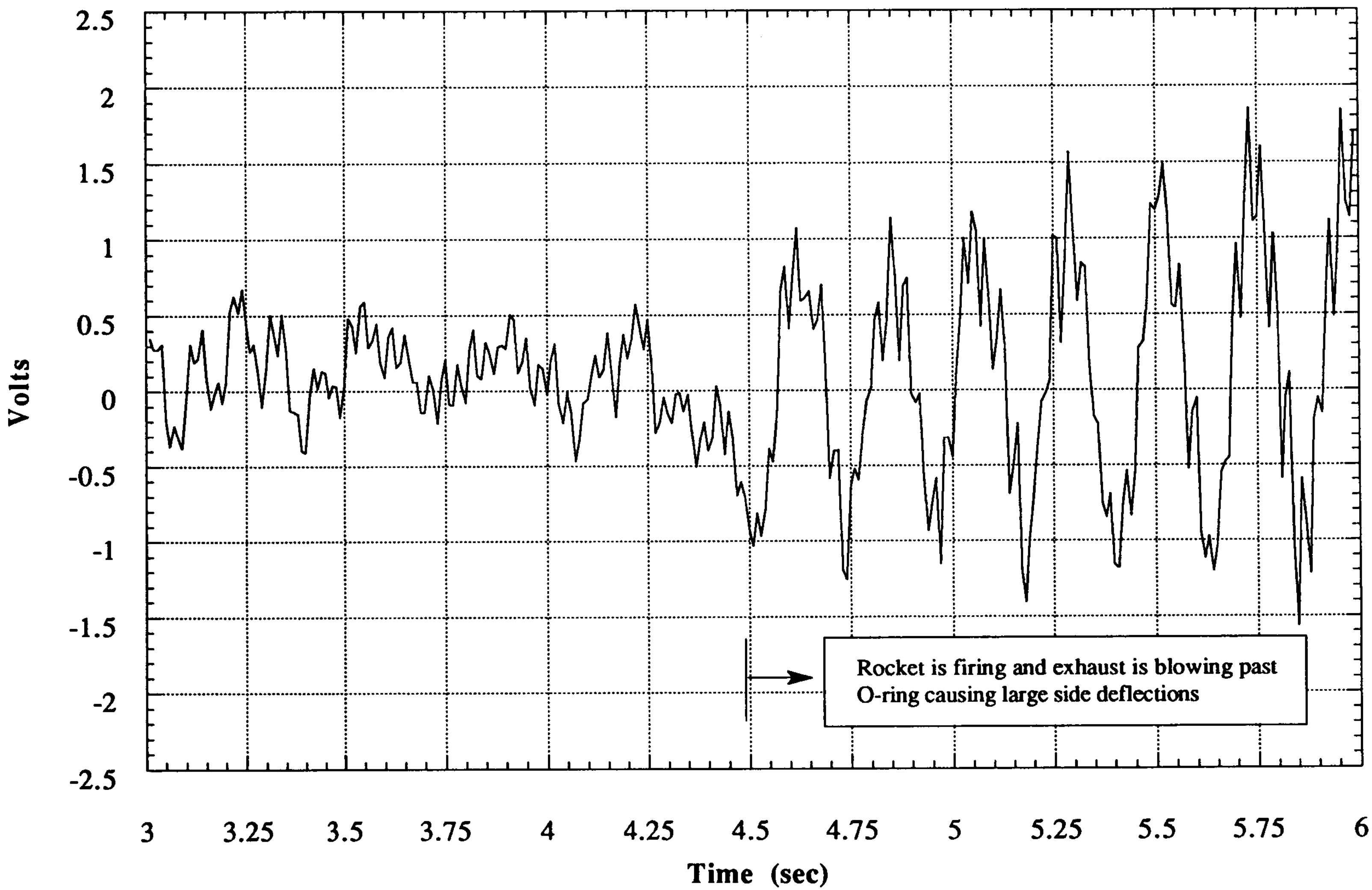

Figure 28. Output Voltage vs. Time for Last Three Seconds of Data Acquisition (Bending)

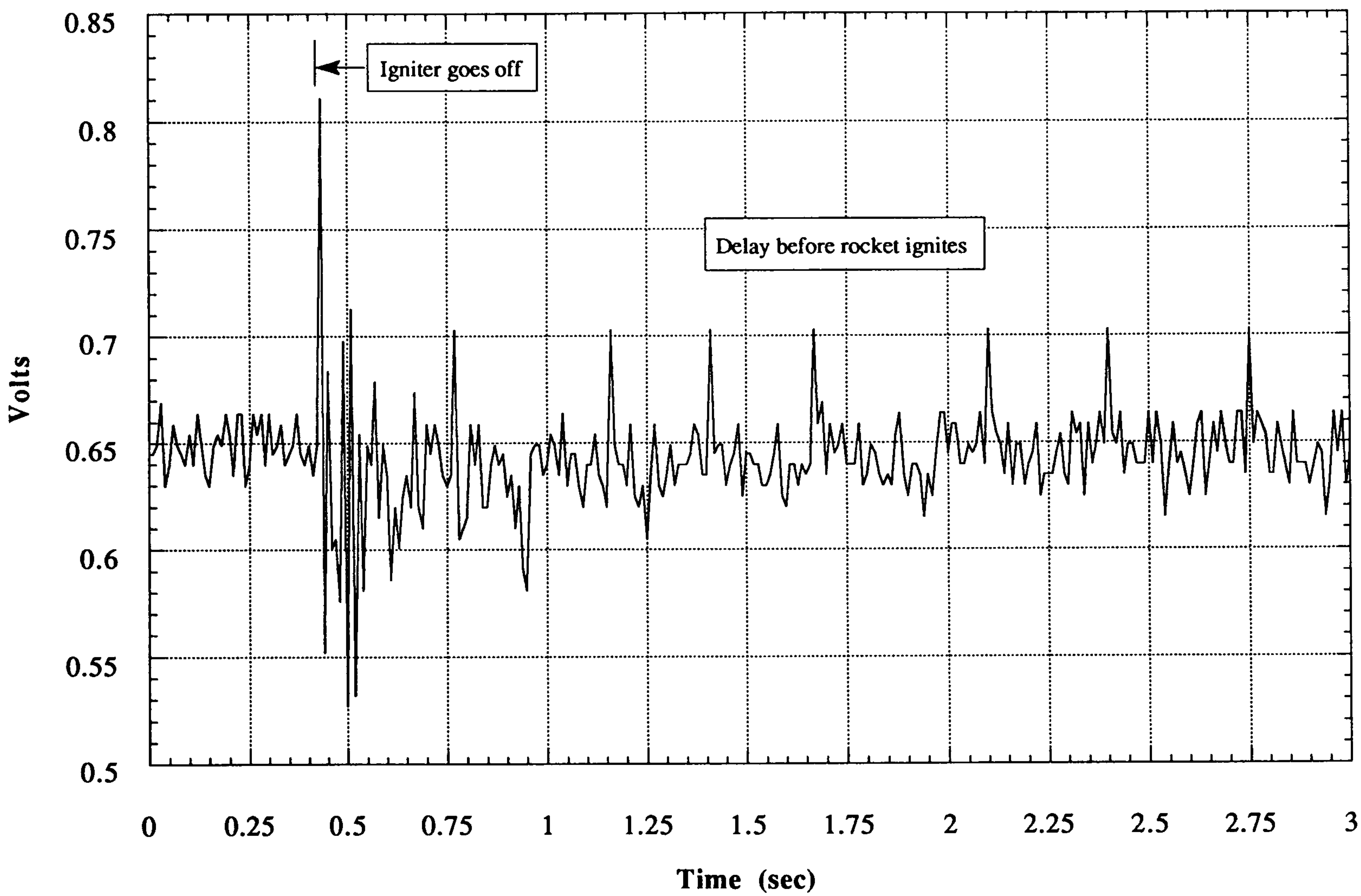

Figure 29. Output Voltage vs. Time for First Three Seconds of Data Acquisition (Thrust)

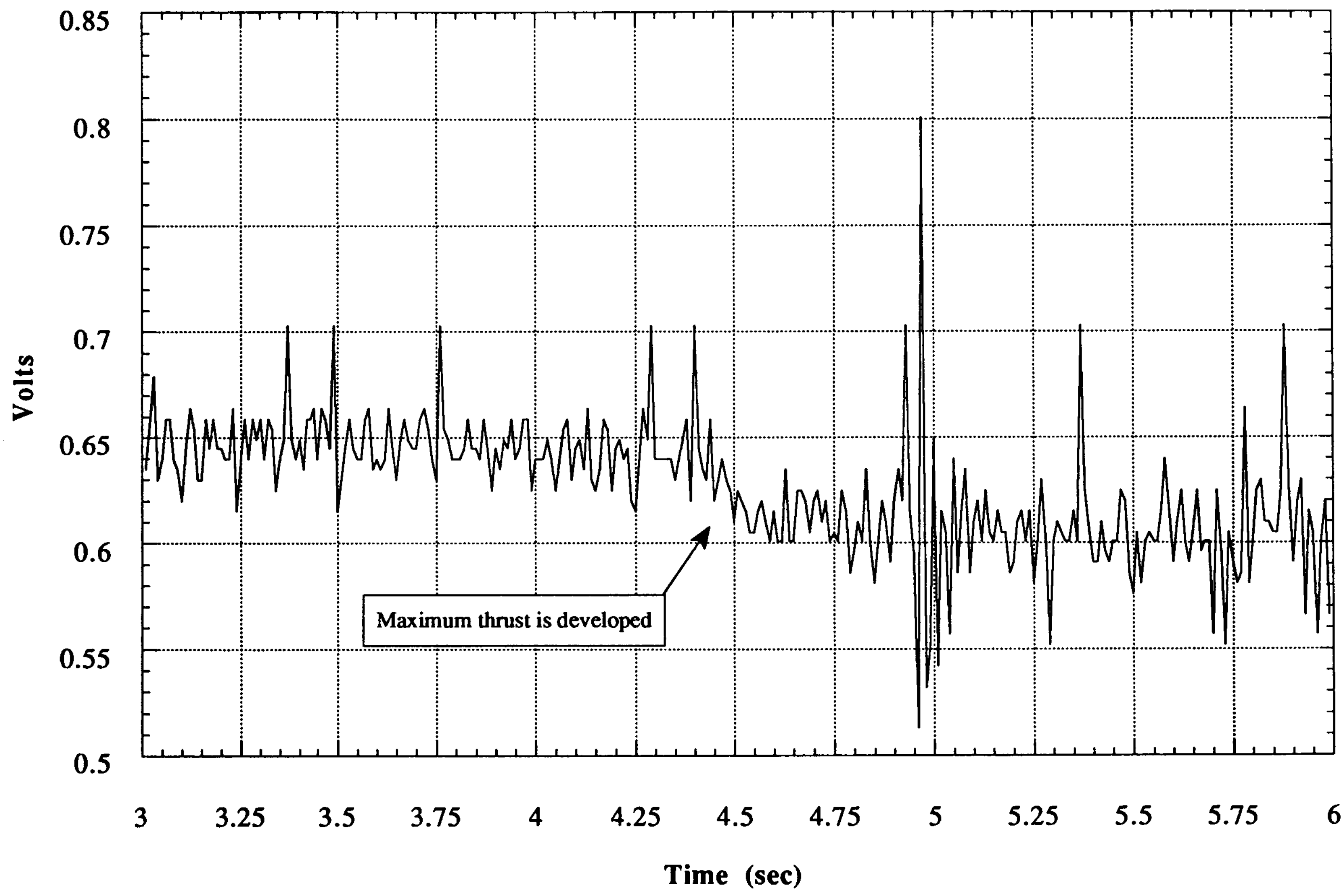

Figure 30. Output Voltage vs. Time for Last Three Seconds of Data Acquisition (Thrust)

The deposits came out in three main pieces and several smaller ones. The grayish colored Al_2O_3 recovered weighed 13 grams. The propellant weight before the motor burn was 190 grams. About 7% of total propellant weight was recovered in the form of Al_2O_3. More Al_2O_3 may have accumulated if all of the exhaust gases passed through the nozzle, instead of going out the head-end of the combustion chamber.

With a couple of large pieces of Al_2O_3 to examine, the distribution profile of the accumulation around the circumference of the casing could be seen. Figure 31 shows what this distribution looks like. The deposits extend from the nozzle end of the casing up to about the midlength of the casing. There is more accumulation near the nozzle end as expected and there are larger "chunks" in the deposits near the nozzle end. The Al_2O_3 is more porous further away from the nozzle end. The Al_2O_3 is evenly distributed around the circumference of the casing. There is no evidence of Al_2O_3 collecting in a pool around the submerged nozzle. With the table rotating at 300 rpm, the normal acceleration, $a_n = r\omega^2$, at the midlength of the rocket motor is 35 g's.

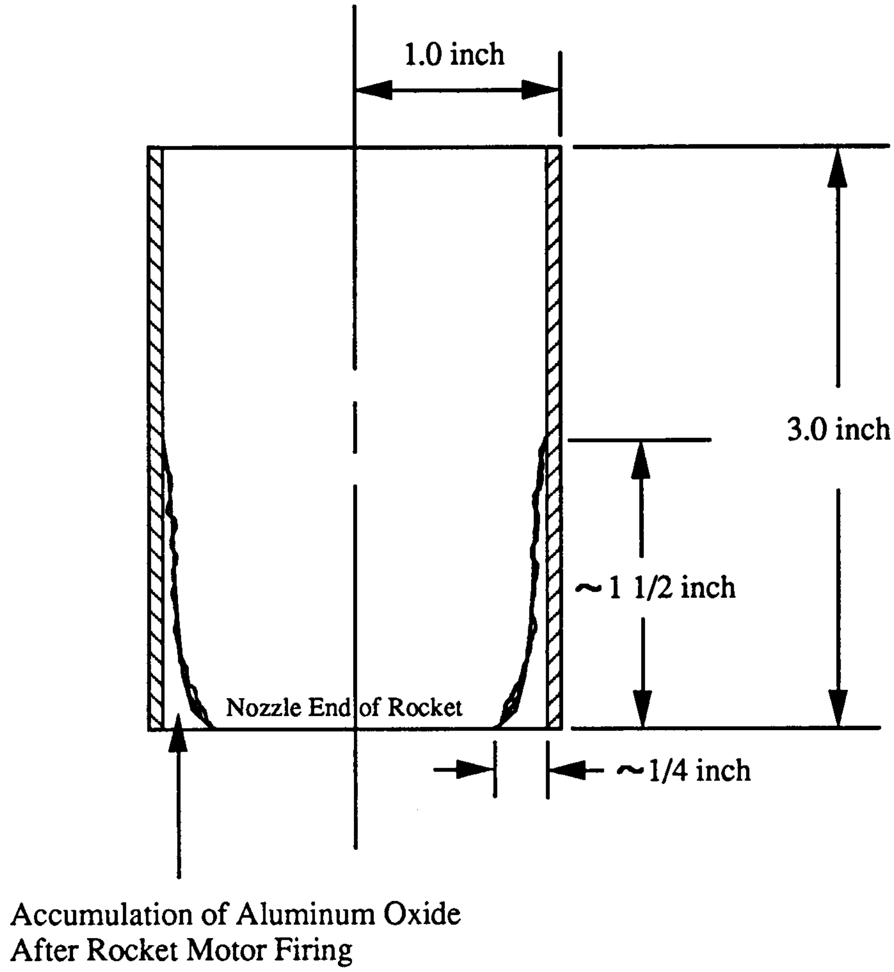

Figure 31. Drawing Showing the Accumulation of Aluminum Oxide on the Inside of the First Rocket Fired

V. CONCLUSIONS AND RECOMMENDATIONS

This test stand was built to investigate the interaction between the combustion gases and rocket motor dynamics. Even though to date only one rocket motor has been fired, the test apparatus promises to provide useful results in the investigation of jet damping and jet driving phenomenon. It is also useful in examining the accumulation of aluminum oxide in the combustion chamber of a spinning rocket motor rotating about a transverse axis.

Because of the O-ring failure on the first run, any results pertaining to the magnitude and direction of the moment generated by the solid rocket motor is inconclusive. The first run was useful in that it checked out the data acquisition system under actual operating conditions. It was also useful in examining the distribution of aluminum oxide slag inside the casing.

The testing program is expected to continue once the new parts are made ready. Here are some recommendations on conducting future tests:

- The initial tests should be conducted at lower spin table rpms to check out all the components and to identify any problems that will be compounded at higher rpms.
- Tests should be conducted with both the secondary electric motor (which spins the rocket about its longitudinal axis) running and not running. This will be useful in seeing what affect spin has on the jet damping forces.
- The data acquisition system should be configured to record for a longer time period and at a faster sampling rate.
- A careful dynamic data analysis should be performed on the experimental data to obtain the best results. The characteristic vibrations of the test stand need to be

identified so that they can be filtered out of the data. SuperScope can be useful in doing this. It is capable of performing Fast Fourier Transforms as well as other data analysis functions.

- Both the aluminized and nonaluminized propellant motors should be used. This should help clarify the effects of the accumulation of aluminum oxide in the combustion chamber.

Here are some suggestions for modifying the test stand to eliminate unwanted vibrational effects:

- A thicker shaft than the 3/4 inch shaft from the primary electric motor up to the spin table could be used. A sturdier shaft would help keep the table steady.
- To reduce structural flexibility, the test stand legs could be made from thicker material.
- Another way to keep the shaft from moving is to put another pilot bearing on the shaft just above the coupling between the primary electric motor and the 3/4 inch shaft. The pilot bearing needs to be attached to something sturdy, possibly fixed to the floor.
- To compensate for the mass being lost during the motor burn, a moveable weight located on the table on the same axis as the rocket motor could be used. As the motor burns, the weight would move outward on the table to try and maintain the same moment of inertia as when the motor begins to fire.

LIST OF REFERENCES

LIST OF REFERENCES

1. Thiokol Corporation Space Motor Catalog, Thiokol Corporation, Tactical Operations, Elkton Division, 1987.

2. Flandro, G.A., M. Leloudis, and R. Roach "Flow Induced Nutation Instability in Spinning Solid Propellant Rockets," AL-TR-89-084, Final Report, Astronautics Laboratory, Edwards Air Force Base, April 1990.

3. Flandro, G.A., "Characteristics of Nutation Instability of Intelsat VI Spin Stabilized Spacecraft During Perigee Propulsion Maneuver," Final Report, Submitted to Intelsat, Washington, D.C., August 1988.

4. Flandro, G.A., W.K. VanMoorhem, R. Shorthill, K. Chen, M. Woolsey, C. D. Clayton, and P. A. Findlayson, "Fluid Mechanics of Spinning Rockets," AFRPL TR-86-072, Final Report, Air Force Rocket Propulsion Laboratory, Edwards Air Force Base, January 1987.

5. Roach, R., V. Burnley, G. Flandro, and J. Burnette, "Internal Ballistics Interactions in Spinning Rocket Nutation Instability," AIAA Paper No. 90-0042, Presented at the 28th Aerospace Sciences Meeting, Reno, Nevada, January 8-11, 1990.

6. Misterek, D.L., J. W. Murdock, and S. Koshigoe, "Gas-Dynamic Flow in a Spinning, Coning Solid Rocket Motor," Journal of Propulsion and Power, Vol. 9, No. 1, Jan.-Feb. 1993, 35-42.

7. Mingori, D. L. and Y. Yam, "Nutational Instability of a Spinning Spacecraft with Internal Mass Motion and Axial Thrust," AIAA Paper No. 86-2271, Proceedings of AIAA/AAS Astrodynamics Conference, Williamsburg, VA, August 18-20, 1986, 367-375.

8. Patera, R.P., "The Analysis and Simulation of the PAM-S Coning Instability - Vol. 1. Summary," Report No. TOR-0091(6464-06)-1, The Aerospace Corporation, El Segundo, CA (30 October 1990).

9. Kang, J.Y. and J.E. Cochran, Jr., "Further Investigation of Anomalous Attitude Motion of a Spin-Stabilized Upper Stage," AAS Paper 91-480, 705-722.

10. Or, A. C., "Rotor-Pendulum Model for the Perigee Assist Module Nutation Anomaly," Journal of Guidance, Control, and Dynamics, Vol. 15, No. 2, March-April 1992, 297-303.

11. Greenspan, H.P., The Theory of Rotating Fluids, Cambridge University Press, 1968.

12. Rosser, J.B., R.R. Newton, and G.L. Gross, Mathematical Theory of Rocket Flight, McGraw-Hill Book Co., 1947, New York.

13. Davis, L.J., J.W.J. Follin, and L. Blitzer, Exterior Ballistics of Rockets, D. Van Nostrand Co., Princeton, New Jersey, 1958.

14. Thomson, W. T., Introduction to Space Dynamics, John Wiley and Sons, New York, 221-227, 1961.

15. Kolk, W. R., Modern Flight Dynamics, Prentice-Hall, Inc., Englewood Cliffs, N.J. 1961.

16. Rott, N. and L. Pottsepp, "Simplified Calculations of the Jet-Damping Effects," AIAA J.2, 764-766, April 1964.

17. Thomson, W. T. and G. S. Reiter, "Jet Damping of a Solid Rocket: Theory and Flight Results," AIAA J.3, 413-417, March 1965.

18. Breuer, D.W. and W.R. Southerland, "Jet-Damping Effects: Theory and Experiment," J. Spacecraft, Vol. 2, No. 4, 638-639, July-Aug. 1965.

APPENDIXES

APPENDIX A

Thiokol CORPORATION
TACTICAL OPERATIONS
Elkton Division

★ STAR 37XFP
TE-M-714-16/-17
66-KS-8,550
ORBIT INSERTION MOTOR

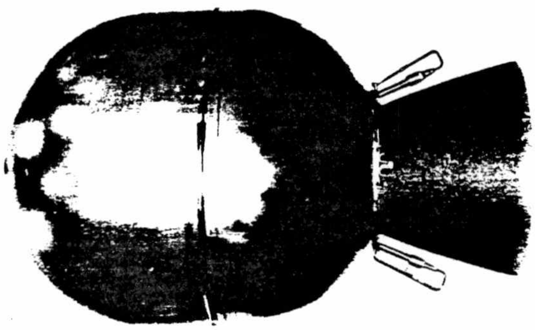

The STAR 37XFP TE-M-714-16 configuration has been qualified as the orbit insertion motor for Rockwell International's Global Positioning Satellite (GPS), and the TE-M-714-17 configuration has been qualified as the apogee motor for the RCA SATCOM KuBand satellite. The STAR 37XFP motor can be used as a replacement for the STAR 37F motor, which has been discontinued.

MOTOR PERFORMANCE (55°F Vacuum)

Burn Time/Action Time, sec	66/67
Ignition Delay Time, sec	0.12
Burn Time Average Chamber Pressure, psia	527
Action Time Average Chamber Pressure, psia	523
Maximum Chamber Pressure, psia	576
Total Impulse, lbf-sec	570,450
Propellant Specific Impulse, lbf-sec/lbm	292.6
Effective Specific Impulse, lbf-sec/lbm	290.0
Burn Time Average Thrust, lbf	8,550
Action Time Average Thrust, lbf	8,480
Maximum Thrust, lbf	9,550

SPIN CAPABILITY, rpm — 65 to 90

WEIGHTS, lbm (Excluding Remote S&A/ETA)

Total Loaded	2,107.1
Propellant (including igniter propellant)	1,948.2
Case Assembly	58.1
Nozzle Assembly (excluding igniter propellant)	70.0
Internal Insulation	26.8
Liner	1.2
Miscellaneous	2.8
Total Inert (excluding igniter propellant)	159.6
Burnout	140.3
Propellant Mass Fraction	0.925
S&A/ETA	4.2

TEMPERATURE LIMITS

Operation	32 to 100°F
Storage	40 to 90°F

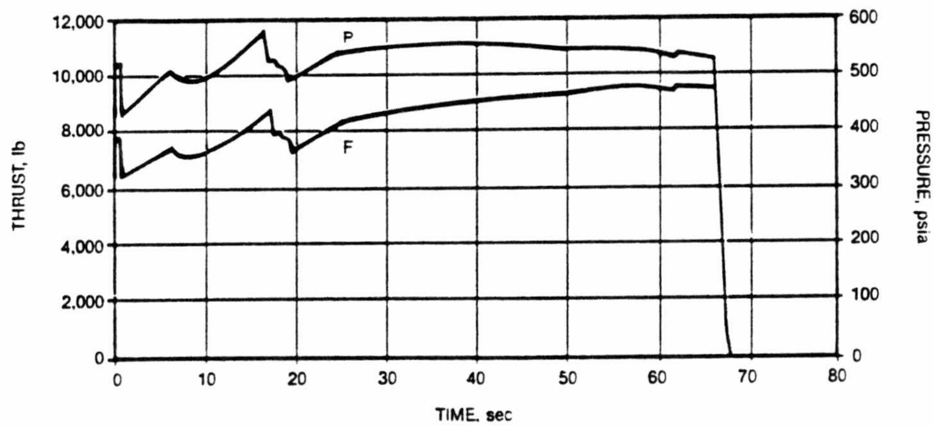

BC16370 4/91

★ **STAR 37XFP**
TE-M-714-16/-17
66-KS-8,550
ORBIT INSERTION MOTOR

Thiokol CORPORATION
TACTICAL OPERATIONS
Elkton Division

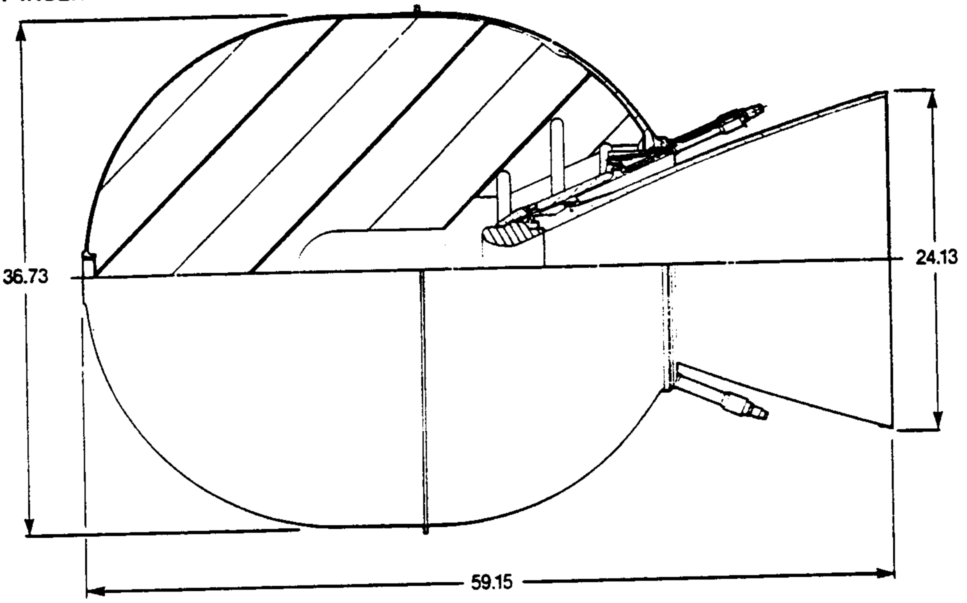

CASE

Material	6Al-4V Titanium
Minimum Ultimate Strength, psi	170,000
Minimum Yield Strength, psi	160,000
Hydrostatic Test Pressure, psi	763
Minimum Burst Pressure, psi	896
Hydrostatic Test Pressure/Maximum Pressure	1.05
Burst Pressure/Maximum Pressure	1.25
Nominal Thickness, in.	0.055

NOZZLE

Exit Cone Material	Carbon-Phenolic
Throat Insert Material	3D Carbon-Carbon
Initial Throat Diameter, in.	3.18
Exit Diameter, in.	23.51
Expansion Ratio, Initial/Average	54.8/48.7
Expansion Cone Half Angles, Exit/Eff, deg	15.2/16.8
Type	Fixed, Contoured
Number of Nozzles	1

LINER

Type	TL-H-318A
Density, lbm/in.^{3}	0.038

IGNITION TRAIN

Components	S&A/ETAs/TBI/flamestick initiator/ toroidal pyrogen
Minimum Firing Current per Detonator, amperes	5.0
Circuit Resistance per Detonator, ohms	1
No. of Detonators and TBIs	2

PROPELLANT

Propellant Designation and Formulation — TP-H-3340

- AP—71%
- Al—18%
- HTPB Binder—11%

PROPELLANT CONFIGURATION

Type	Internal-Burning, Radial-Slotted
Web, in.	15.36
Web Fraction, %	0.83
Sliver Fraction, %	0
Propellant Volume, in.^{3}	30,085
Volumetric Loading Density, %	96.7
Web Average Burning Surface Area, in.^{2}	1,940
Initial Surface to Throat Area Ratio	208

PROPELLANT CHARACTERISTICS

Burn Rate at 500 psia, in./sec	0.228
Burn Rate Exponent	0.30
Density, lbm/in.^{3}	0.0651
Temperature Coefficient of Pressure, %/°F	0.10
Characteristic Exhaust Velocity, ft/sec	5,100
Adiabatic Flame Temperature, °F	6,113
Effective Ratio of Specific Heats	(Chamber) 1.14
	(Nozzle Exit) 1.18

CURRENT STATUS

Production

Thiokol CORPORATION, *TACTICAL OPERATIONS, Elkton Division*
P.O. Box 241, 55 Thiokol Road, Elkton, MD 21922-0241 (301) 392-1000

Thiokol CORPORATION
TACTICAL OPERATIONS
Elkton Division

★ **STAR 48B**
TE-M-711-18
84.1-KS-15,430
LONG NOZZLE
UPPER-STAGE MOTOR
PAM DELTA

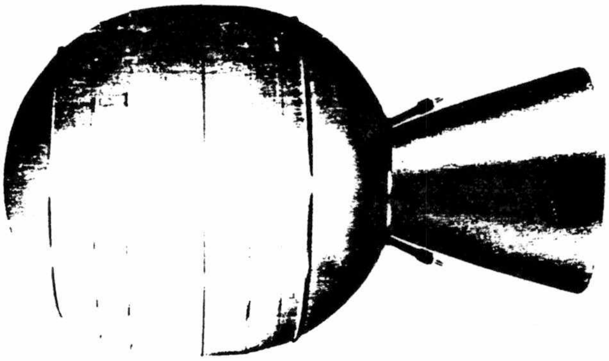

The STAR 48B motor is qualified for the McDonnell Douglas Payload Assist Module (PAM) Delta. The basic version for Delta-launched missions contains 4430 pounds of propellant (an increase of 25 pounds over STAR 48) and has the same 80-inch overall length as the Delta version of the STAR 48. The design incorporates the same high-energy propellant and high-strength case as the STAR 48. The semi-submerged nozzle uses a carbon-phenolic exit cone.

MOTOR PERFORMANCE (75°F Vacuum)

Burn Time/Action Time, sec	84.1/85.2
Ignition Delay Time, sec	0.099
Burn Time Average Chamber Pressure, psia	579
Action Time Average Chamber Pressure, psia	575
Maximum Chamber Pressure, psia	618
Total Impulse, lbf-sec	1,303,705
Propellant Specific Impulse,' lbf-sec/lbm	294.2
Effective Specific Impulse, lbf-sec/lbm	292.1
Burn Time Average Thrust, lbf	15,430
Action Time Average Thrust, lbf	15,370
Maximum Thrust, lbf	17,490

SPIN CAPABILITY, rpm

45 to 80

WEIGHTS, lbm

Total Loaded*	4,720.8
Propellant (including igniter propellant)	4,431.2
Case Assembly	128.5
Nozzle Assembly (excluding igniter propellant)	96.6
Internal Insulation	59.8
Liner	2.1
Miscellaneous	2.7
Total Inert (excluding igniter propellant)*	289.6
Burnout*	257.8
Propellant Mass Fraction*	0.939
S&A/ETA	3.7

*Excluding remote S&A/ETA

TEMPERATURE LIMITS

Operation	30 to 100°F
Storage	30 to 100°F

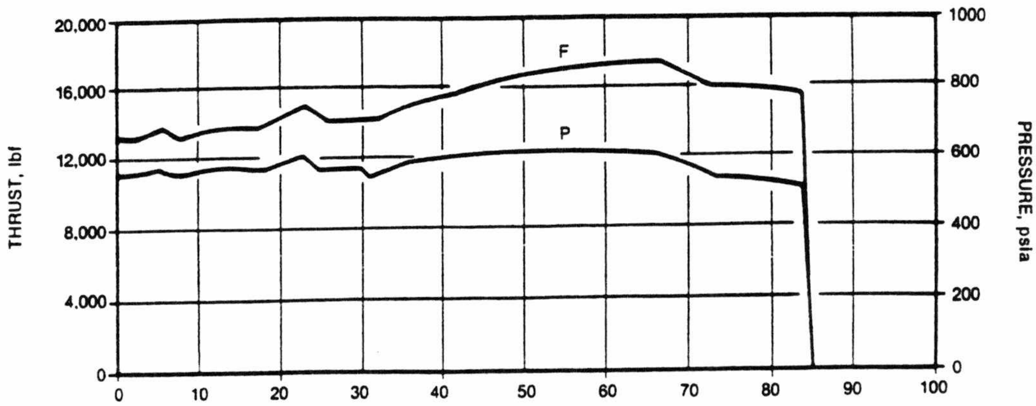

BC13561 4/91

★ **STAR 48B**
TE-M-711-18
84.1-KS-15,430
LONG NOZZLE
UPPER-STAGE MOTOR
PAM DELTA

Thiokol CORPORATION
TACTICAL OPERATIONS
Elkton Division

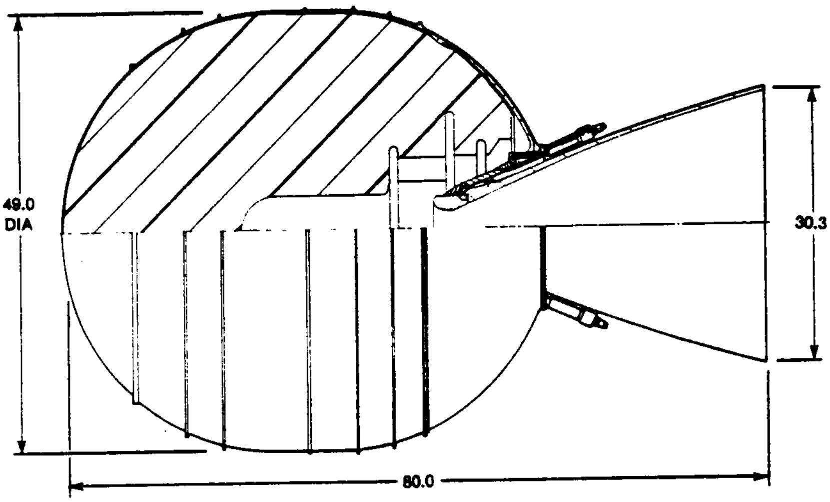

CASE

Material	6Al-4V Titanium
Minimum Ultimate Strength, psi	165,000
Minimum Yield Strength, psi	155,000
Hydrostatic Test Pressure, psi	732
Minimum Burst Pressure, psi	860
Hydrostatic Test Pressure/Maximum Pressure	1.05
Burst Pressure/Maximum Pressure	1.25
Nominal Thickness, in.	0.069

NOZZLE

Exit Cone Material	Carbon-phenolic
Throat Insert Material	3D carbon-carbon
Initial Throat Diameter, in.	3.98
Exit Diameter, in.	29.5
Expansion Ratio, Initial/Average	54.8/47.2
Expansion Cone Half Angles, Exit/Eff, deg	14.3/16.3
Type	Fixed, contoured
Number of Nozzles	1

LINER

Type	TL-H-318
Density, lbm/in.^{3}	0.038

IGNITION TRAIN

Components	S&A/ETA/TBI/flamestick initiator/ toroidal pyrogen
Minimum Firing Current per Detonator, amperes	5.0
Circuit Resistance per Detonator, ohms	1.1
No. of Detonators and TBI's	2

PROPELLANT

Propellant Designation and Formula	TP-H-3340
AP — 71%	
Al — 18%	
HTPB Binder — 11%	

PROPELLANT CONFIGURATION

Type	Internal-burning, radial-slotted star with head-end web
Web, in.	20.47
Web Fraction, %	84
Sliver Fraction, %	0
Propellant Volume, in.^{3}	68,050
Volumetric Loading Density, %	93.1
Web Average Burning Surface Area, in.^{2}	3,325
Initial Surface to Throat Area Ratio	225.9

PROPELLANT CHARACTERISTICS

Burn Rate at 500 psia and 60°F, in./sec	0.228
Burn Rate Exponent	0.30
Density, lbm/in.^{3}	0.0651
Temperature Coefficient of Pressure, %/°F	0.10
Characteristic Exhaust Velocity, ft/sec	5,010
Adiabatic Flame Temperature, °F	6,113
Effective Ratio of Specific Heats (Chamber)	1.14
(Nozzle Exit)	1.18

CURRENT STATUS

Production

Thiokol CORPORATION, TACTICAL OPERATIONS, Elkton Division
P.O. Box 241, 55 Thiokol Road, Elkton, MD 21922-0241 (301) 392-1000

Thiokol CORPORATION
TACTICAL OPERATIONS
Elkton Division

★ STAR 63D
TU-936
118-KS-19,050
PERIGEE MOTOR

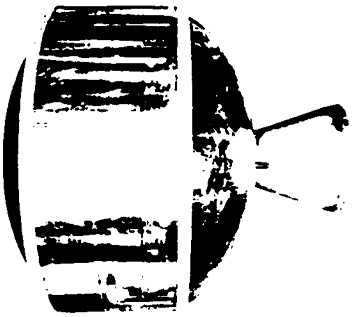

The STAR (IPSM) 63D has successfully delivered two payloads to elliptical transfer orbit, no failures. Given a range of propellant loads, the STAR 63D payload capability ranges from 3,080 to 4,588 lb at a constant velocity of 8,012 ft / sec. Motor components are of proven design features and materiel, thus maximizing reliability.

MOTOR PERFORMANCE (77°F Vacuum)

Action Time, sec	118
Ignition Delay Time, sec	0.300
Action Time Average Chamber Pressure, psia	607
Maximum Chamber Pressure, psia	957
Total Impulse, lbf-sec	2,033,000
Propellant Specific Impulse, lbf-sec/lbm	285
Effective Specific Impulse, lbf-sec/lbm	283
Action Time Average Thrust, lbf	19,050
Maximum Thrust, lbf	26,710

SPIN CAPABILITY, rpm 30-85

WEIGHTS, lbm (Excluding Remote S&A/ETA)

Total Loaded	7,716
Propellant (including igniter propellant)	7,166.5
Case Assembly	233.5
Nozzle Assembly	134
Forward Closure Assembly	0.9
Igniter Assembly	2.08
Internal Insulation	157.4
Liner	22.7
Miscellaneous	2.9
Total Inert	550.0
Burnout	508.0
Propellant Mass Fraction	0.929

TEMPERATURE LIMITS

Operation	30 to 100°F
Storage	30 to 100°F

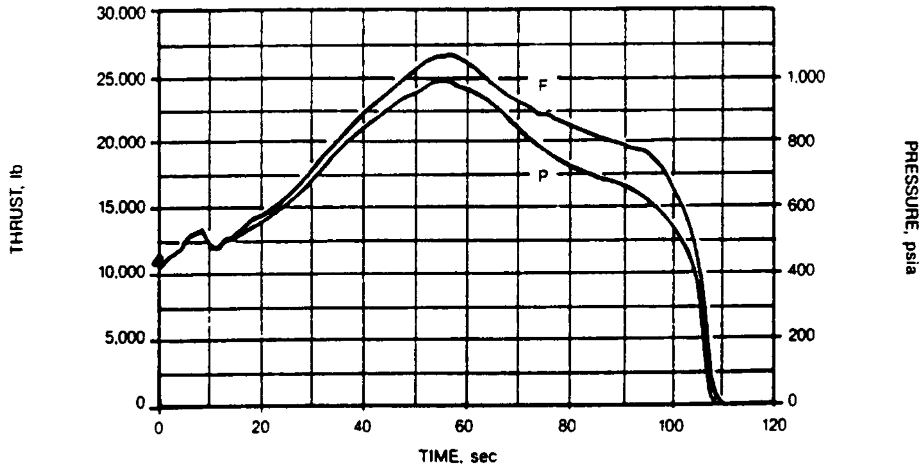

BC19162 4/91

★ **STAR 63D**
TU-936
118-KS-19,050
PERIGEE MOTOR

Thiokol CORPORATION
TACTICAL OPERATIONS
Elkton Division

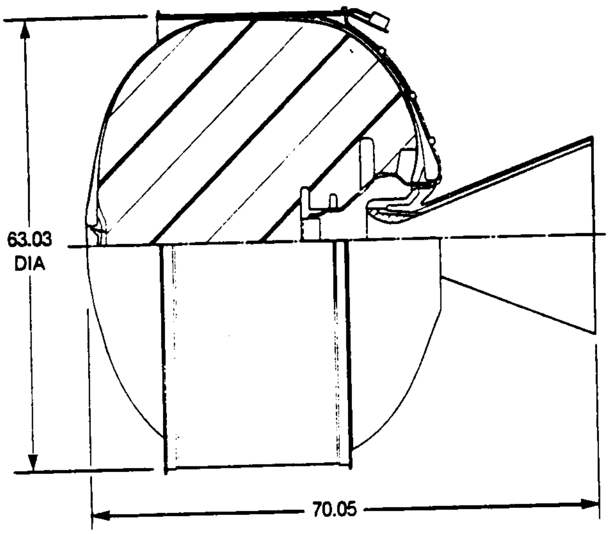

CASE

Material	Kevlar
Hydrostatic Test Pressure, psi	971
Minimum Burst Pressure, psi	1,406
Hydrostatic Test Pressure/Maximum Pressure	1.05
Burst Pressure/Maximum Pressure	1.5

NOZZLE

Exit Cone Material	Carbon Phenolic
Throat Insert Material	3D Carbon-Carbon
Initial Throat Diameter, in.	4.174
Exit Diameter, in.	21.82
Expansion Ratio, Initial/Average	27.3/25.8
Expansion Cone Half Angles, Exit/Eff, deg	19
Type	Fixed
Number of Nozzles	1

LINER

Type	HTPB UF-2155
Density, lbm/in.^{3}	0.038

IGNITION TRAIN

Components	S&A/ETA/TBI/ignition transfer line/wafer
Minimum Firing Current per Detonator, amperes	5.0
Circuit Resistance per Detonator, ohms	1.1
No. of Detonators and TBIs	2

PROPELLANT

Propellant Designation and Formulation	TP-H-1202
AP—57%	
Al—21%	
HTPB Binder—9.8%	
HMX—12%	

PROPELLANT CONFIGURATION

Type	Head-End Grain
Web, in.	30.3
Sliver Fraction, %	0
Propellant Volume, in.^{3}	107,600
Volumetric Loading Density, %	96
Web Average Burning Surface Area, in.^{2}	3,550
Initial Surface to Throat Area Ratio	40.9

PROPELLANT CHARACTERISTICS

Burn Rate at 625 psia and 60°F, in./sec	0.257
Burn Rate Exponent	0.31
Density, lbm/in.^{3}	0.0666
Temperature Coefficient of Pressure, %/°F	0.1
Characteristic Exhaust Velocity, ft/sec	5,056
Adiabatic Flame Temperature, °F	6,086
Effective Ratio of Specific Heats (Chamber)	1.123
(Nozzle Exit)	1.124

CURRENT STATUS

Production

Thiokol CORPORATION, *TACTICAL OPERATIONS, Elkton Division*
P.O. Box 241, 55 Thiokol Road, Elkton, MD 21922-0241 (301) 392-1000

APPENDIX B

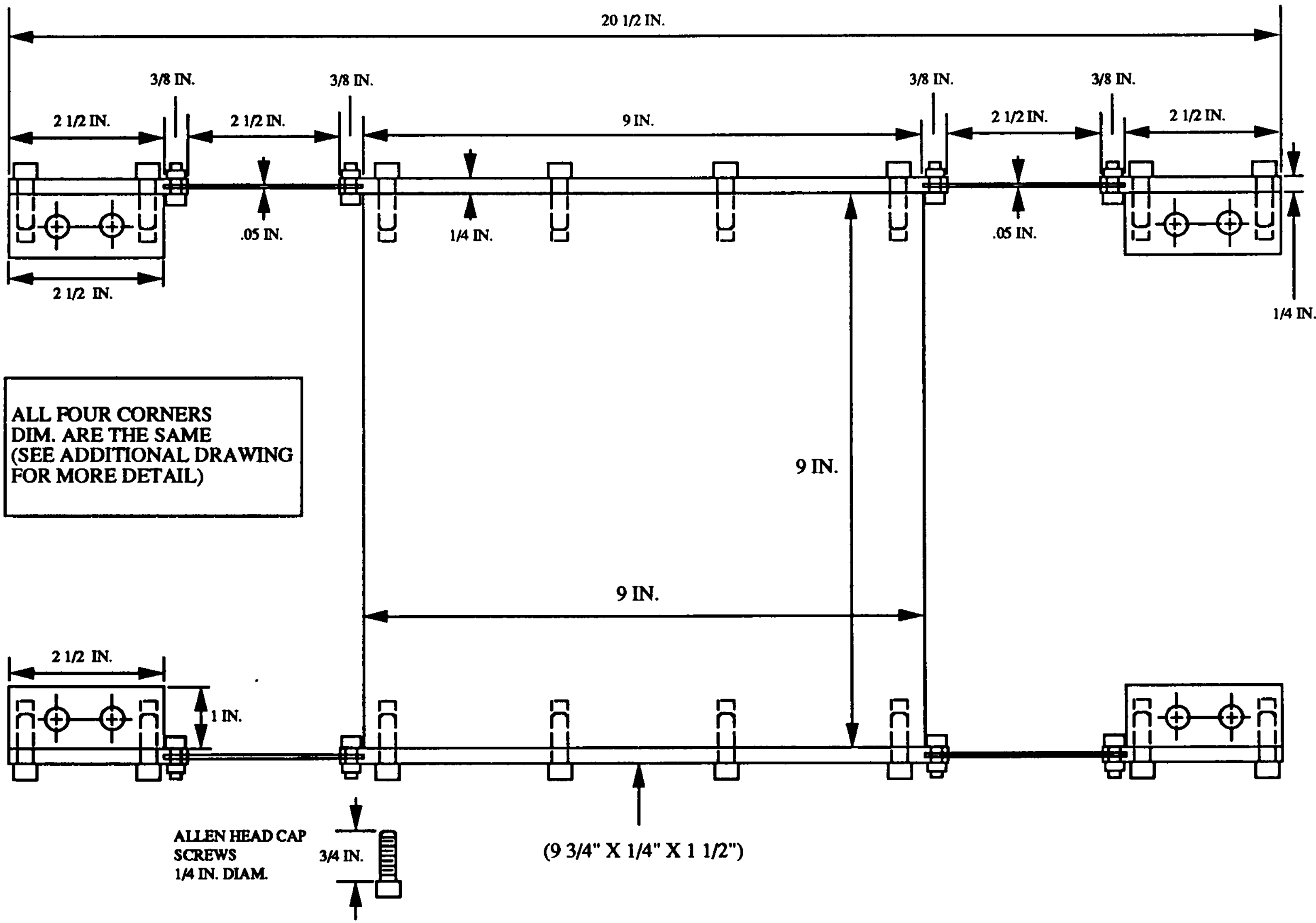

Drawing Showing Dimensions of Flexure Assembly (Top View)

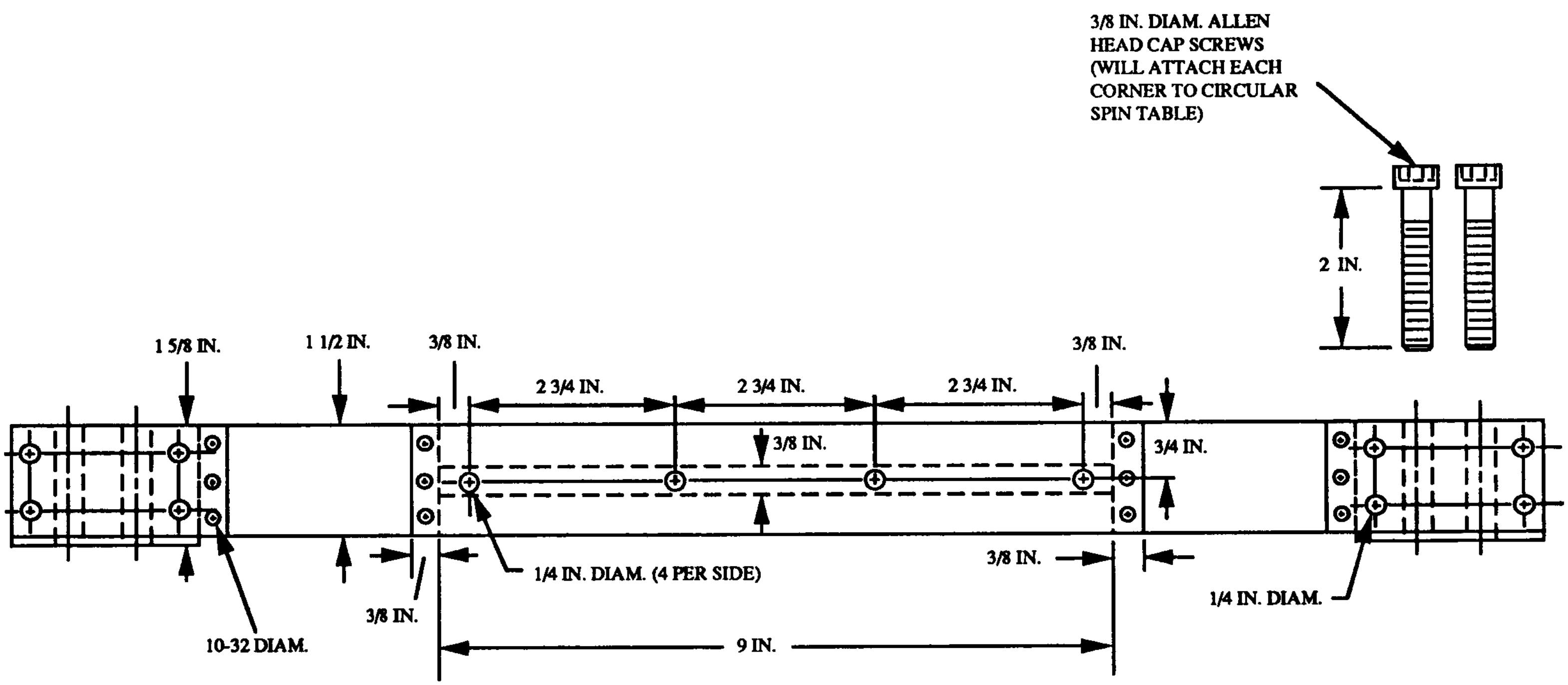

Drawing Showing Dimensions of Flexure Assembly (Side View)

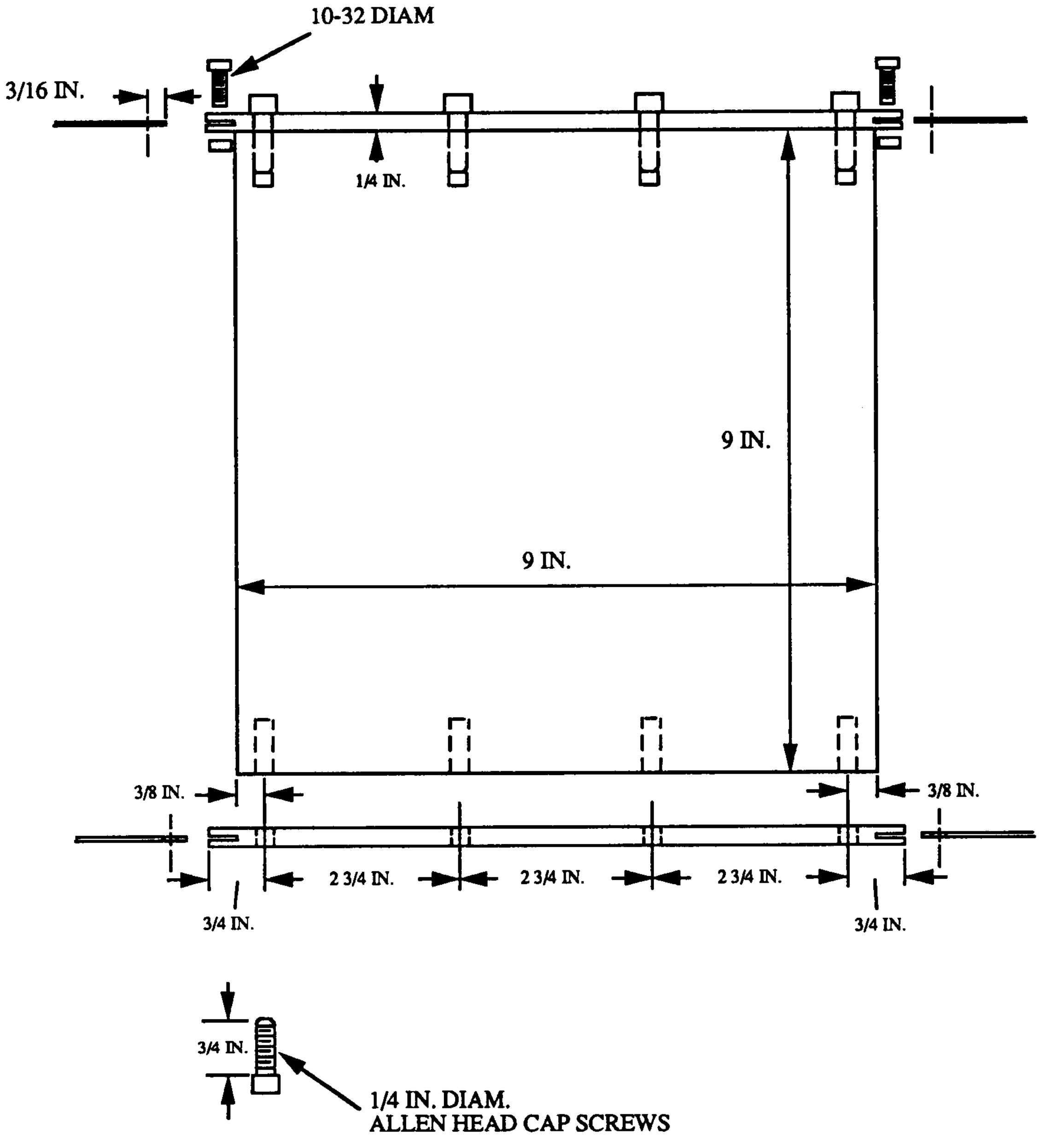

CLOSE UP VIEW OF MIDDLE SECTION

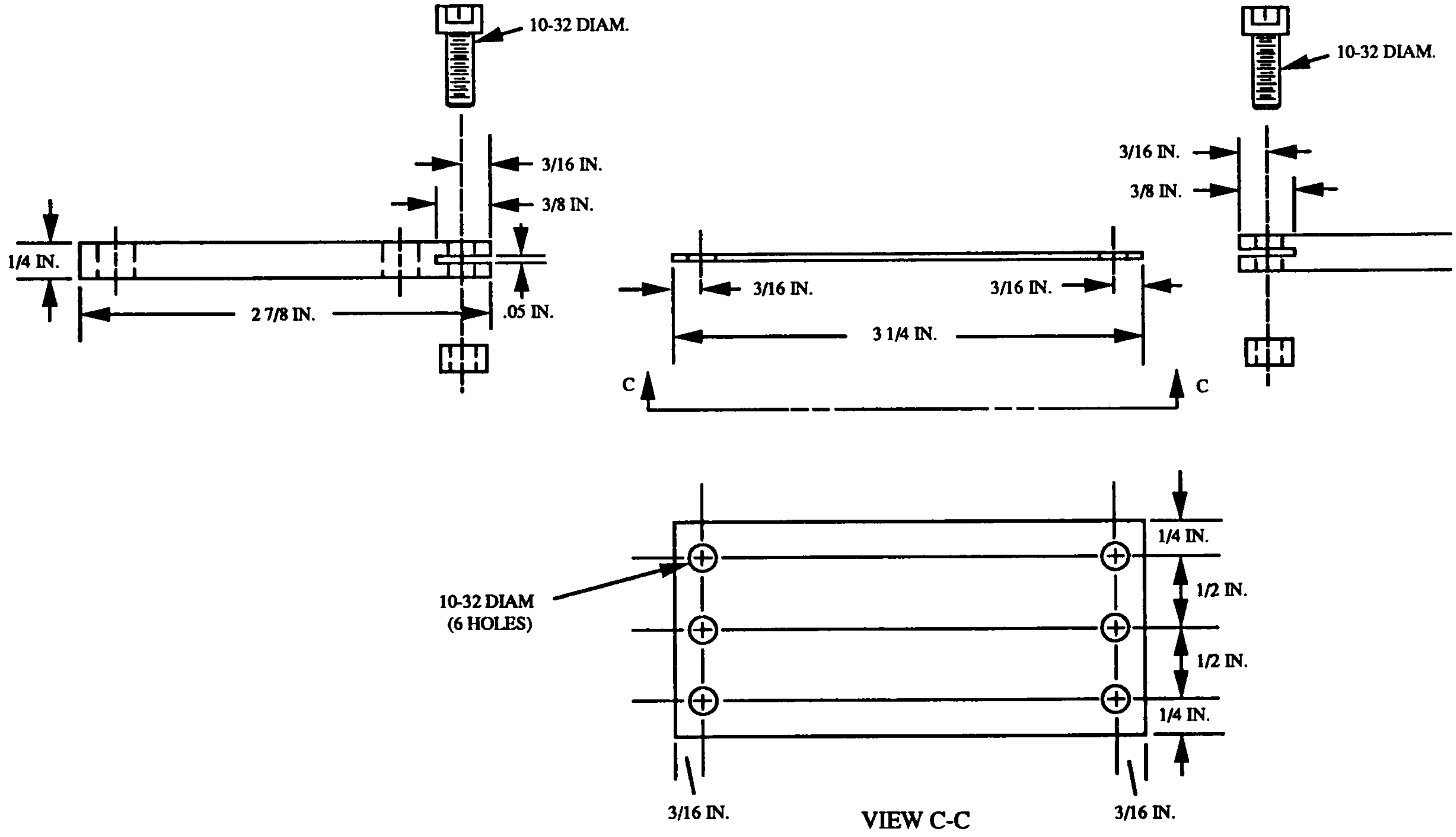

Drawing Showing Individual Flexure Dimensions

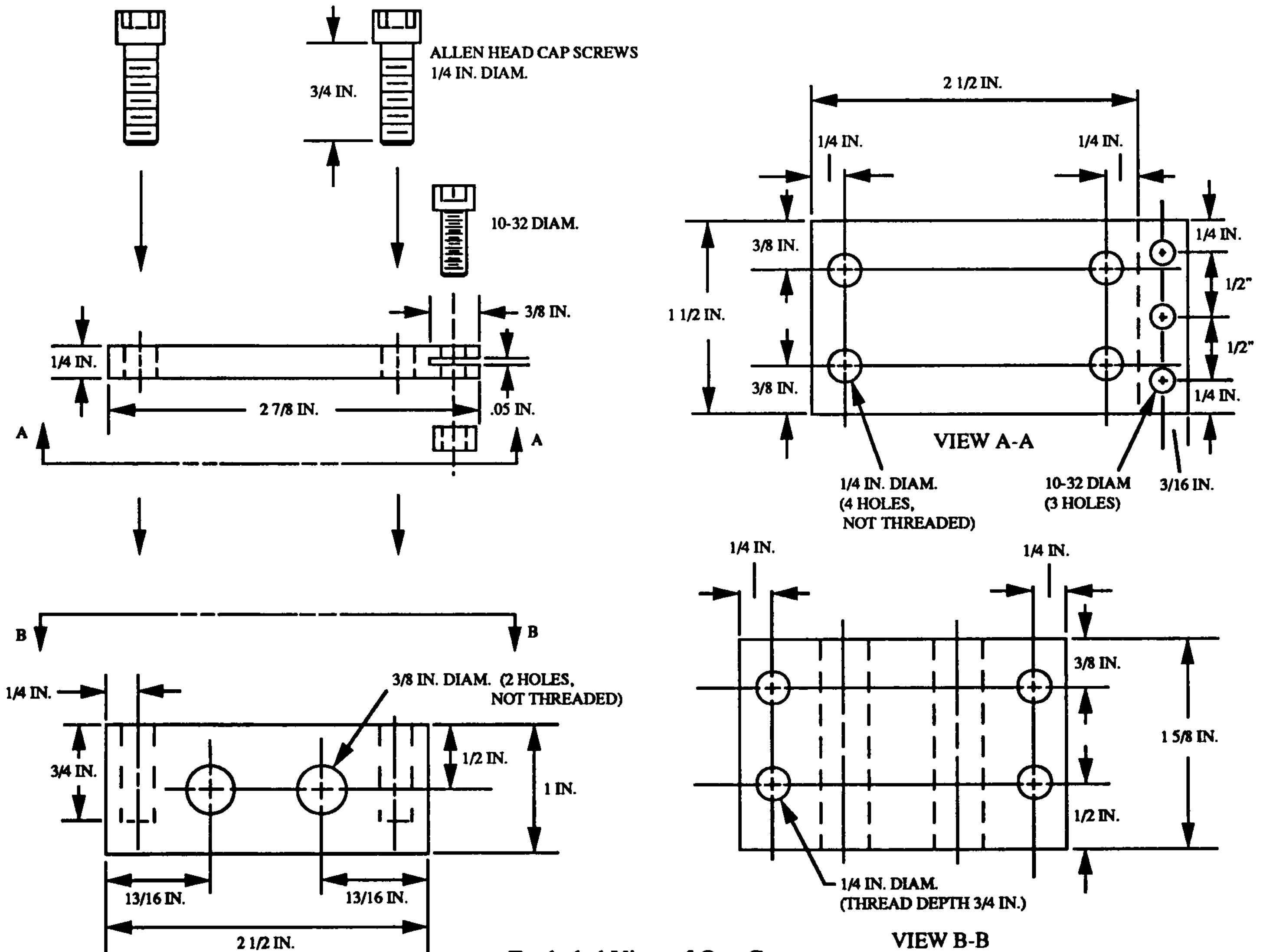

Exploded View of One Corner

APPENDIX C

5B38 Strain Gage Input Module

The 5B38 wide bandwidth strain gage input module accepts signals from full bridge and half bridge 300Ω to 10kΩ transducers. The 5B38 provides +10V excitation and produces an output of -5V to +5V. This module features a bandwidth of 10kHz.

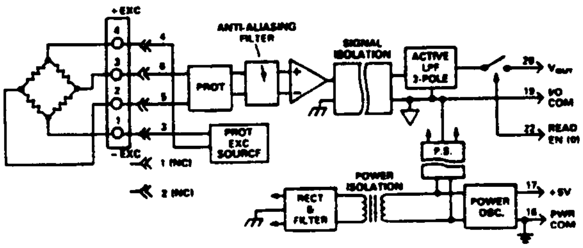

Figure 2.6. 5B38 Functional Block Diagram

Figure 2.6 is a functional block diagram of the 5B38. A protection circuit assures safe operation even if a 240V rms power line is connected to the input screw terminals. The excitation section provides +10V. Since the excitation lines are not sensed at the strain gage, care should be taken to minimize any IR loss in these wires. This can be accomplished by the use of heavy gage wires or the shortest length of wire possible. A one pole anti-aliasing filter is located at the module's input, while a three pole low pass filter in the output stage sets the bandwidth and yields optimum noise performance. A low drift amplifier provides the module's gain.

Signal isolation is provided by transformer coupling, using a proprietary modulation technique for linear, stable performance. A demodulator on the output side of the signal transformer recovers the original signal, which is then filtered and buffered to provide a clean, low-impedance output. A series output switch is included to eliminate the need for external multiplexing in many applications. This switch is controlled by an active-low enable input. In cases where the output switch is not used, the enable input should be grounded to power common to turn on the switch, as it is on the 5B01 backplane.

The single +5V supply powers a clock oscillator which drives power transformers for the input and output circuits. The input circuit is fully floating. In addition, the output section acts as a third floating port, eliminating many problems that might be created by ground loops and supply noise. The common-mode range of the output circuit is limited, however: output common must be kept within ±3V of power common.

The 5B38 can be used with half bridge transducers since the module contains bridge completion circuitry. The module can be factory configured for wide input ranges to accommodate the DC offset created by mismatches in the transducer. There is no provision for use with quarter or three quarter bridge strain gages. However, the user may complete the bridge to the half or full bridge level external to the module and use the 5B38 module.

Note: A current path must exist between power common and output common for proper operation of the demodulator and output switch. See Chapter 4 for details.

5B38 Ordering Information

Input Bridge Range and Excitation	Output Range	Model
Full Bridge, 10.0V excitation, @ 3mV/V Sensitivity, 300Ω to 10kΩ	-5V to +5V	5B38-02
Half Bridge, 10.0V excitation, @ 3mV/V Sensitivity, 300Ω to 10kΩ	-5V to +5V	5B38-04
Full Bridge, 10.0V excitation, @ 2mV/V Sensitivity, 300Ω to 10kΩ	-5V to +5V	5B38-05

5B38 Specifications (typical @ 25°C and +5V Power)

	Full Bridge	Half Bridge
Models	5B38-02, 5B38-05	5B38-04
Input Span Limits	±30mV @ 3mV/V Sensitivity ±20mV @ 2mV/V Sensitivity	±30mV @ 3mV/V Sensitivity
Output Range	-5Vto +5V	*
Accuracy[1]	±0.08% span ±10µV RTI	±0.08% span ± 1mV RTI
Nonlinearity	±0.02% span	*
Excitation Output[2]	+10V ± 3mV	*
Excitation Load Regulation	±5ppm/mA	*
Half Bridge Voltage Level	N/A	(Excitation Voltage/2) ±1mV
Stability vs. Ambient Temperature		
Input Offset	1µV/°C	*
Output Offset	±40µV/°C	*
Gain	±25ppm of reading/°C	*
Excitation Voltage	±15ppm/°C	*
Half Bridge	N/A	±15ppm/°C
Input Bias Current	±3nA	*
Input Resistance		
Normal	20MΩ minimum	*
Power Off	40kΩ minimum	*
Overload	40kΩ minimum	*
Noise		
Input, bandwidth = 10Hz	0.4µV rms RTI	±2µV rms RTI
Input, bandwidth = 10kHz	±70nV/√Hz RTI	±250nV/√Hz RTI
Output, bandwidth = 100kHz	10mV p-p RTO	*
Bandwidth, -3dB	10kHz	*
Rise Time, 10% to 90% Span	40µs	*
Settling Time (to 0.1%)	250µsec	7msec
CMV, Input to Output		
Continuous	1500V rms max	*
Transient	meets IEEE-STD 472 (SWC)	*
CMR (50 or 60Hz)	100dB	*
1kΩ in Either or Both Input Leads		
Input Protection		
Continuous	240V rms max continuous	*
Output Resistance	50Ω	*
Voltage Output Protection	Continuous Short to Ground	*
Output Selection Time	20µs	*
Output Selection Input		
Max Logic "0"	+1V	*
Min Logic "1"	+2.5V	*
Max Logic "1"	+36V	*
Input Current "0"	0.4mA	*
Power Supply Voltage	+5V ±5%	*
Power Supply Sensitivity	25ppm reading/% ± 2.5µV RTI/%	*
Power Consumption	1W full load, .6W no load	*
Size	2.25"x2.25"x0.60" (52mmx52mmx15mm)	*
Environmental		
Temperature Range, Rated Performance	-25°C to +85°C	*
Temperature Range, Storage	-40°C to +85°C	*
Temperature Range, Operating	-40°C to +85°C	*
Relative Humidity (MIL 202)	0 to 95% @ 60°C noncondensing	*
RFI Susceptibility	±0.5% span error @ 400MHz, 5W, 3'	*

Chapter 3
5B Series Subsystem Solutions

The 5B Series includes a number of backplanes which provide a complete signal conditioning solution. The two 5B Series 16 channel backplanes currently available, the 5B01 and 5B02, provide different system configuration options. The 5B03 and 5B04, one and two channel backplanes, allow an economical means to handle a few remote signals. A single channel socket, AC1360, is available for module evaluation. It is discussed in Chapter 4.

Both 16 channel 5B Series backplanes can be mounted in a 19" x 3.5" panel space. The one and two channel backplanes are DIN rail compatible. Each channel has four screw terminals for field connections. These connections satisfy all transducer inputs and process current outputs and provide sensor excitation when necessary. A cold junction sensor is supplied on each channel to accommodate thermocouple modules. All backplanes require an external +5V power supply.

This chapter describes each backplane and how they are used. Common topics – power requirements, field terminations, installation, and interface accessories – follow the backplane discussions.

5B01 Backplane

The 5B01, diagrammed in Figure 3.1, is a 16 channel backplane that provides single ended high level analog input/output pins on the system connector. It is pin compatible with Analog Devices' 3B Series applications. (Note, however, that 5B Series modules provide a ±5V output swing rather than the ±10V swing provided by 3B Series modules). Figure 3.2 is a schematic of the 5B01 backplane.

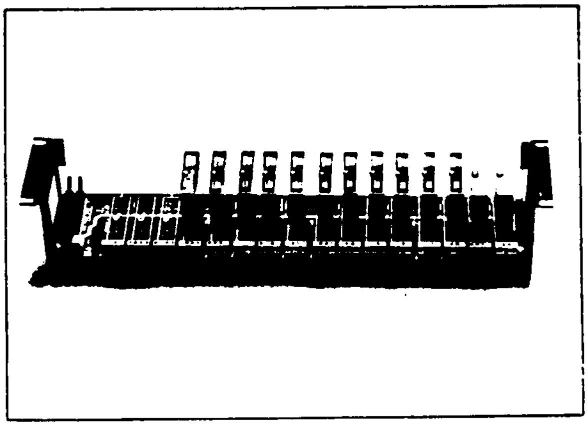

Connector Pin Usage

Signal connections between the 5B01 backplane and the associated measurement and control system are made at P1 and P2. These connectors are identical electrically. The redundant connector may be useful if a 5B01 is used for both analog input and analog output and the data acquisition system has separate input and output connectors. Figure 3.3 is a diagram of the voltage I/O provided on the P1 and P2 connectors of the 5B01 backplane.

A signal path is provided for each channel, and, in addition, a number of grounding pins are present in the connector pinout to provide interchannel shield conductors in the ribbon cable. In some cases, discussed below, the ground conductors will not provide an accurate signal reference, so a SENSE pin is also provided in the pinout.

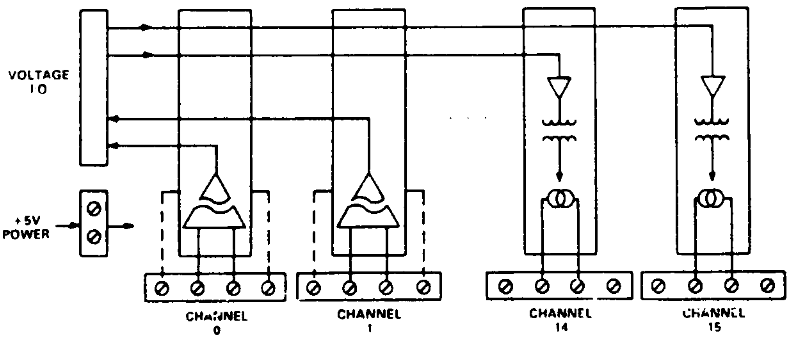

Figure 3.1. 5B01 Diagram

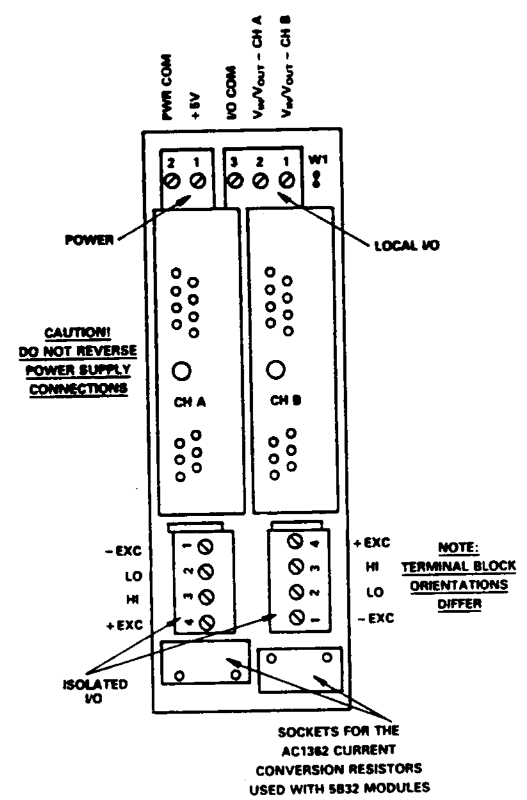

Figure 3.9. 5B04 Wiring Diagram

Power Requirements

All 5B Series backplanes require external +5V power. This is connected to TB17 on the 5B01 and TB16 on the 5B02.

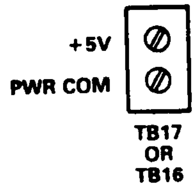

Figure 3.10. Power Connection - Terminal Block 17 (5B01), Terminal Block 16 (5B02)

The power supply is bused to all signal conditioners on the backplane. The total subsystem power requirement is a function of the modules that are used. Module power requirements are listed in Table 3.2. Chassis mounting 1A (model 955) and 3A (model 976) +5V power supplies are available.

Model	Current
5B30	30mA
5B31	30mA
5B32	30mA
5B34	30mA
5B37	30mA
5B38	200mA
5B39	170mA*
5B40	30mA
5B41	30mA
5B47	30mA

* Maximum output load resistance is 750Ω.

Table 3.2. Module Power Requirements

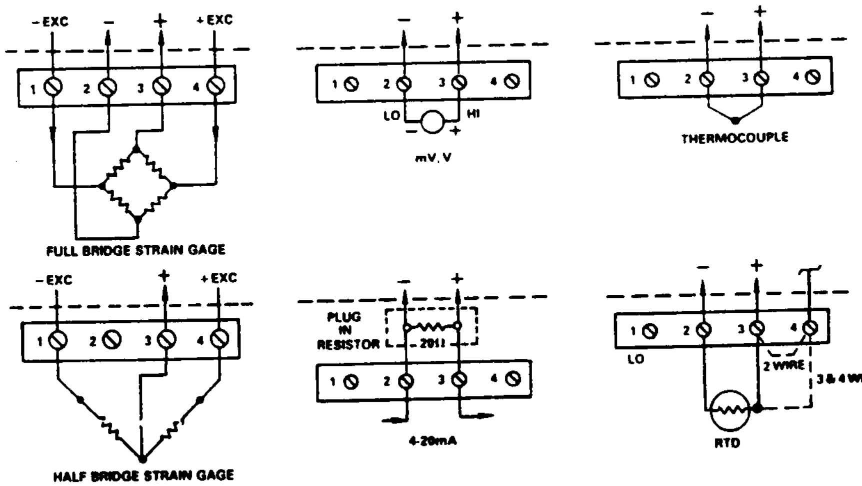

Figure 3.11. Input Field Connections

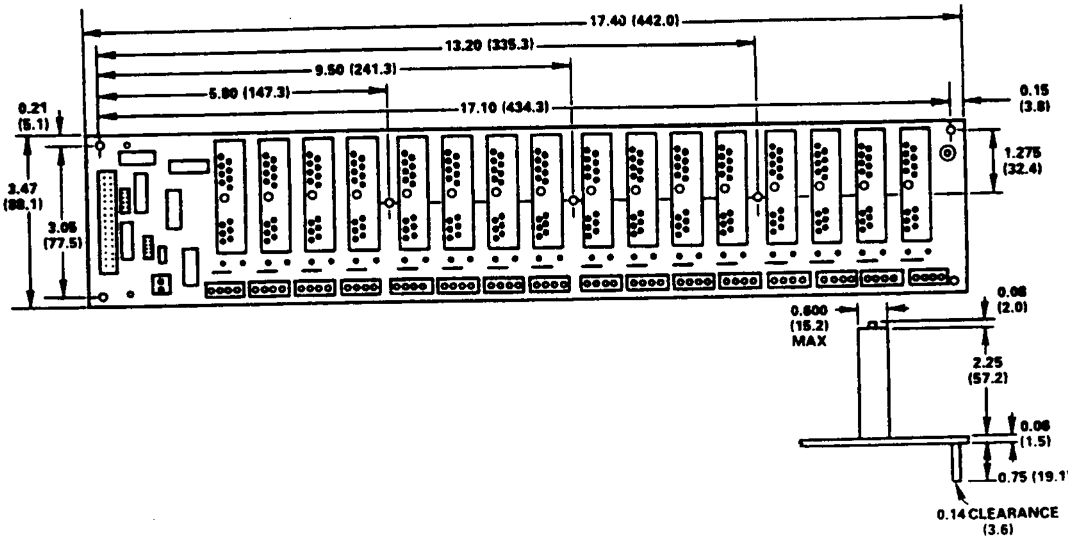

Figure 3.12. 5B01 and 5B02 Backplane Mounting Dimensions in Inches and (mm)

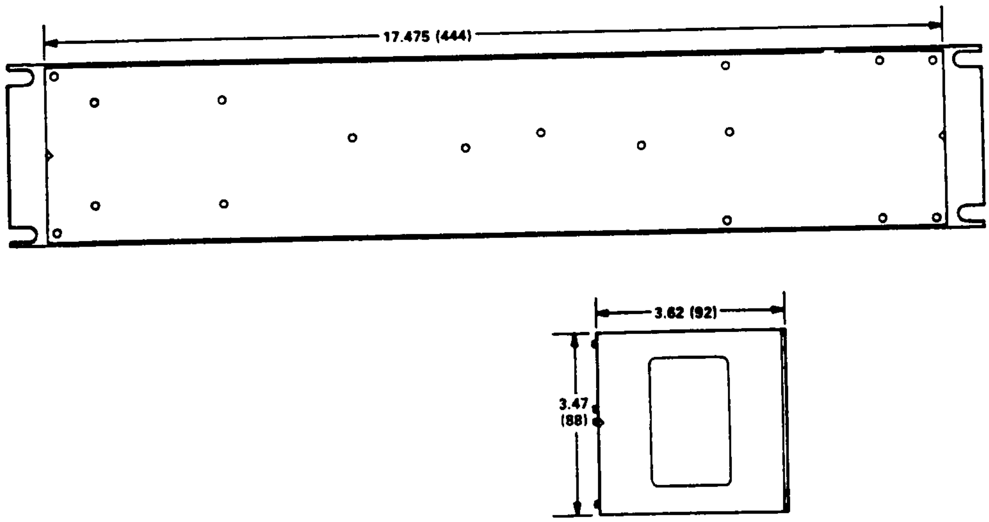

Figure 3.13. AC1363 Rack Mount Diagram (dimensions in inches and (mm))

Field Terminations

All field terminations are made at terminal blocks 1-16 of the 5B01 and terminal blocks 1-17 on the 5B02. Input screw terminal connections are indicated in Figure 3.11; the input screw terminals in the figure are numbered 1, 2, 3 and 4 to correspond to the markings on each backplane.

Output screw terminal connections are:

OUT LO	terminal 2
OUT HI	terminal 3

14-22 AWG wire may be used with these terminal blocks.

MacADIOS™ II

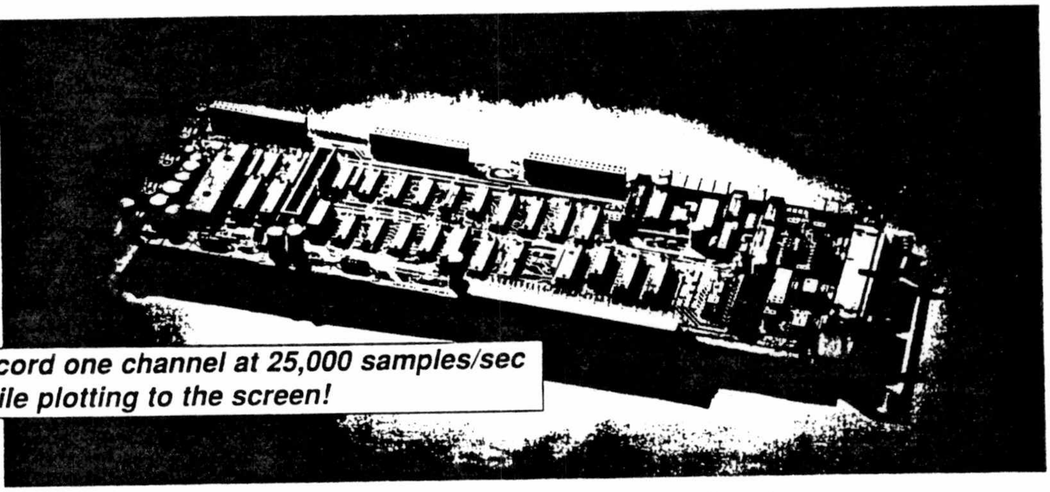

Overview

The MacADIOS II turns the 32-bit Macintosh II into a powerful and complete laboratory computer system with capabilities rivaling scientific/engineering "minicomputers" and "super microcomputers". This is made possible with an advanced multifunction analog and digital I/O board set, and powerful MacADIOS II software. With MacADIOS II, the Macintosh II interfaces directly with the real world for a variety of applications, including data acquisition, external measurement and control, and counter/timer operations.

Optional Software

- MacInstruments
- MacADIOS Manager II
- MacSpeech Lab II
- LabVIEW with TurboDrivers
- Parameter Manager Plus with TurboDrivers
- Labtech Notebook with TurboDrivers
- 33 data manipulation routines callable from Lightspeed C, MPW C, MPW Pascal, Turbo Pascal, absoft MacFortran, MPW FORTRAN, and Microsoft QuickBASIC.

Daughterboards

- GWI-MHz: 833kHz, 12-bit A/D
- GWI-ADC: 142kHz, 12-bit A/D
- GWI-HAD: 50kHz, 16-bit A/D
- GWI-GAD: 16kHz, 16-bit A/D
- GWI-DAC: 2 independent, 16-bit D/As
- GWI-AFS: 2 antialiasing filters
- GWI-TST: time stamper
- GWI-J2E: 16 additional analog inputs
- GWI-MUX: 32 additional analog inputs
- GWI-DIO: 16 digital I/O channels
- GWI-PRO: prototyping board

MacADIOS II Board

- 5μs A/D converter with throughput up to 142,000 samples/second
- 16 single-ended or 8 differential analog voltage input channels (expandable to 56 differential or 112 single-ended inputs with optional daughter-boards)
- 12-bit (4096 counts) A/D with ±10V or 0V to 10V input range and programmable gain of 1,10,or 100
- Two 12-bit (4096 counts) analog voltage output channels with a ±10V or 0V to 10V range
- 8 digital input channels
- 8 digital output channels
- 3 Counter/Timer channels
- 3 A/D trigger modes

TurboDrivers Software Features

- Emulate an oscilloscope, scrolling strip chart recorder, chart recorder or spectrum analyzer with unprecedented speed. For example, read one channel at 25,000 samples/second while simultaneously plotting to the screen.
- Acquire data in the background using interrupts
- Spool to hard disk

Software Performance

- Read one channel at 833,000 samples/sec
- Read/write 1 to 4 channels simultaneously at 100,000 samples/sec
- Digitize 1 to 8 multiplexed analog channels at 10μs per channel

Included Software

- TurboDrivers callable from Lightspeed C
- TurboDrivers callable from MPW C
- TurboDrivers callable from MPW Pascal
- TurboDrivers callable from Turbo Pascal
- TurboDrivers callable from absoft MacFortran
- TurboDrivers callable from MPW FORTRAN
- TurboDrivers callable from Microsoft QuickBASIC
- Calibration and test software
- Sample BASIC, FORTRAN, C and Pascal programs

HARDWARE MANUAL

MacADIOS II Hardware Manual, 225 pages
Part #GWI-Demo-Hd II

SOFTWARE MANUAL

MacADIOS Software Series Manual, 400 pages
Part #GWI-Demo-Sft

Complete Hardware Solutions

The MacADIOS II card plugs into one of the Macintosh II expansion slots, or into the GW Instruments Macintosh SE Expansion box (pages 19-20), and provides 16 analog input channels, 2 analog output channels, 8 digital input channels, 8 digital output channels and 3 counter timer channels. There are also eleven daughterboards; up to three can be connected to the MacADIOS II at one time. These daughterboards perform such tasks as high-speed sampling and multichannel input and output. A master clock synchronizes all MacADIOS II activity, so the user can obtain state information from several I/O channels simultaneously. The card and daughterboards are powered from a DC/DC converter which converts the Nubus ±12V to the required ±15V.

The MacADIOS II card comes with TurboDrivers, a set of I/O routines which can be called from BASIC, Pascal, FORTRAN, or C. Daughterboards, signal conditioning modules, relay modules, cables, termination panels, and application software are sold separately.

Powerful Laboratory Software

The MacADIOS II card includes powerful TurboDriver software, a complete set of MacADIOS II I/O routines which can be called from Lightspeed C, MPW C, MPW Pascal, Turbo Pascal, absoft MacFortran, MPW FORTRAN, and Microsoft QuickBASIC. These routines input and output both analog and digital values, digitize waveforms, output waveforms, and perform counter/timer operations. TurboDrivers perform oscilloscope, strip chart recorder, and scan line recorder emulations. With TurboDrivers, data can be simultaneously recorded from one channel at 25,000 samples/second while being plotted to the screen.

MacInstruments, MacADIOS Manager II, MacSpeech Lab II, Labtech Notebook with TurboDrivers, LabVIEW with TurboDrivers, and Parameter Manager Plus with TurboDrivers are compatible with MacADIOS II hardware and are sold separately.

- MacInstruments (page 43) provides high-performance 4-channel oscilloscope, scrolling strip chart recorder, chart recorder, and scan line recorder emulations.
- MacADIOS Manager II (page 45) is a powerful, waveform-oriented application program.
- Labtech Notebook (page 47) uses a spreadsheet to control, acquire, and analyze laboratory data.
- Parameter Manager Plus (page 54) is a powerful technical spreadsheet with the ability to record, analyze, and present data.
- LabVIEW (page 53) is an icon-based programming language which enables the user to design an instrument panel on the Macintosh II screen.

Taken together, these programs offer complete laboratory computing capability formerly costing 5-10 times more. They are sufficient for almost all laboratory computing projects.

Timer & Interrupts

For time-related digital I/O applications, the AM9513A Counter/Timer chip provides the MacADIOS II card with three independent channels which can be used for tasks such as event counting, frequency measurement, pulse-width measurement, single-pulse output, and time-proportional output. Each channel has its own source input, output, and gate input. In addition, the Counter/Timer chip offers a dedicated 4-bit programmable frequency output channel. Two additional channels in the AM9513A are reserved for pacer control (continuous and gated operation). This pacer clock produces a timed series of pulses which initiate A/D conversions. The MacADIOS card is also capable of generating interrupts (Nubus NMRQ) at fixed intervals. This enables the user to set up a data-taking sequence which operates as a background task.

Daughterboards

With the GW Instruments Daughterboard Series, it is possible to add any of the following features: 16-bit A/D converters, 16-bit D/A converters, 833kHz A/D sample rates, anti-aliasing filters, time stamping, additional analog I/O channels, and additional digital I/O channels. Up to 3 daughterboards can be installed on one MacADIOS II card. Choosing from 11 available daughterboards, the user can customize the board for specific applications. This system has two advantages:

1) Cost is minimized since the user need not purchase unnecessary features.

2) As research requirements change with time, the user can easily and efficiently expand the system.

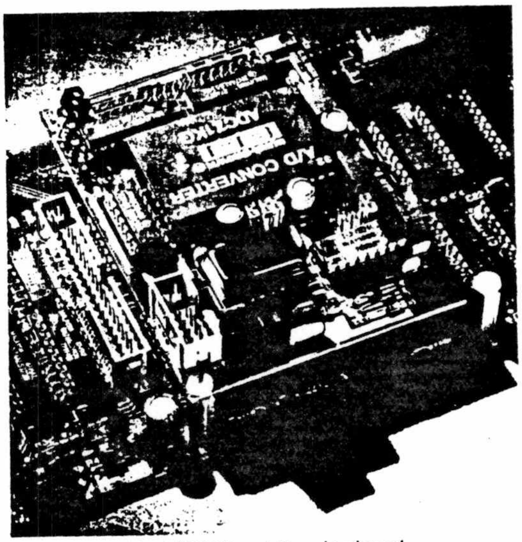

MacADIOS II and Daughterboard

GW Instruments, Inc.
35 Medford Street • Somerville, MA 02143
Phone: (617) 625-4096 • FAX: (617) 625-1322

Technical Specifications[1]

Analog Input

A/D Conversion Time	5.0µs
A/D Resolution	12-bit (4096 counts)
A/D Input Codes[2]	Binary or two's complement
A/D Ranges[2]	0 to +10V, ±10V (gain = 1)
Instrumentation Amplifier Gain	1, 10, 100V/V (software-selectable)
Number of Input Channels[2]	16 single-ended or 8 differential inputs
System Throughput	142kHz (gain = 1, 10) 125kHz (gain = 100)

Measurement Accuracy

G=1, ±10V Range	± 0.02% of 20V FSR
G=10, ±1V Range	± 0.06% of 2V FSR
G=100, ±0.1V Range	± 0.09% of 0.2V FSR
Noise	± 0.03% FSR RMS
Linearity	± 1LSB
Input Overvoltage Protection	± 35V (powered), ± 20V (unpowered)
Input Impedance	>100MΩ, 5pf
Common Mode Voltage (CMV)	± 10V min.
Common Mode Rejection (CMR)	80dB
Gain Drift	± 30ppm/°C of 10V FSR
Offset Drift	± 10ppm/°C of 10V FSR

Analog Output

D/A Resolution	12-bit (4096 counts)
Number of Output Channels	2
Output Voltage Ranges[2]	0 to +10V, ±10V @ 2mA
D/A Input Codes[2]	Binary or two's complement
Output Protection	Short-to-ground, continuous
Output Setting Time	9µs (to ±1/2LSB, +20V step)
Analog Output Accuracy	±0.02%
Noise	0.03% FSR RMS
Gain Drift	±5ppm/°C of full-scale range
Offset Drift	±25µV/°C

Digital I/O

Digital Output Port	8 latching output bits
Digital Input Port	8 non-latching input bits
Input/Output Configuration	TTL-compatible
Input Signal Levels	V_{IH} = 2.0V min V_{IL} = 0.8V max I_{IH} = 20µA, V_I = 2.7V I_{IL} = -0.1mA max
Output Signal Levels	V_{OH} = 2.7V min V_{OL} = 0.5V max I_{OH} = -0.4µA max I_{OL} = 8mA max

Counter/Timer

Number of Channels	3
Modes of Operation	Event counting, frequency measurement, pulse measurement, pulse output, time-proportional outputs
Event Counting	
Maximum Count Rate	7MHz
Minimum Pulse	70nsec
Range	32,767 (15-bit)
Frequency Measurement	
Frequency Range	0 to 7MHz
Minimum Pulse	70nsec
Gate Time	0.001sec to 10sec (programmable)
Resolution	15-bit
Pulse Output (Single pulse)	
Pulse Range	0.4µsec to 65.5sec (programmable)
Time-proportional Outputs	
Duty Cycle Range	0 to 100%
Period Range	0.8µsec to 131sec (programmable)
Time Base Accuracy	±0.01%
Input/Output Signals	TTL-compatible

Convert Command Clock

Resolution	5 decades of 16-bit resolution
Period Range	0.8µsec to 65.5sec

Computer Interface

Bus Resource Utilization	Occupies one long slot in Apple Macintosh II expansion bus, Nubus
Data Acquisition Modes	Supports 16-bit read and 16-bit write Nubus transfers
Interrupt Capability	Performs interrupts via Nubus NMRQ
Compatibility	Apple Computer Macintosh II

Physical/Environmental

I/O Connector	
Digital I/O (J1)	34-pin male ribbon connector
Analog I/O (J2)	34-pin male ribbon connector
AFS (J3)	7-pin male ribbon connector
Dimensions	4.0in. x 12.85in. x 0.8in.
Operating Temperature Range	0 to +70°C
Storage Temperature Range	-25 to +85°C
Relative Humidity	Up to 90% (non-condensing)

Power

Power Consumption	+5V @ 1A max[3] +12V @ 800mA max -12V @ 250mA max

[1] Specifications typically at +25°C and nominal power supply voltage unless otherwise noted. Specifications subject to change without notice.
[2] Jumper-selectable
[3] No daughterboards installed

Product Compatibility

The MacADIOS II card plugs into a Macintosh II expansion slot. It can also be connected to a Macintosh SE via the Macintosh SE Expansion System (pages 19-20). MacADIOS II daughterboards mount directly on the MacADIOS II card. Analog and Digital I/O Modules (pages 37-40) attach to the MacADIOS II via ribbon cables. The MacADIOS ABO and MacADIOS DBO Breakout Units (pages 33-36) also attach to the MacADIOS II via ribbon cables.

MacADIOS II is compatible with MacInstruments (page 43), MacADIOS Manager II (page 45), Parameter Manager Plus with TurboDrivers (page 54), LabVIEW with TurboDrivers (page 53), , Labtech Notebook with TurboDrivers (page 47), and the Data Manipulation Library (page 49).

Ordering Information

MacADIOS II Card

MacADIOS II analog/digital I/O board, TurboDrivers callable from Lightspeed C, MPW C, MPW Pascal, Turbo Pascal, absoft MacFortran, MPW FORTRAN, Microsoft QuickBASIC, calibration software, test software, and full documentation.
Part #GWI-625

VITA

Michael Thomas Lugten was born on June 25, 1968 in Hamilton, Michigan. At the age of 10 he moved to Nashville, Tennessee where he attended Ezell Harding Elementary and Middle Schools. His family then moved to Brentwood, Tennessee and Mike graduated from Page High School in 1986. After high school he attended Tennessee Tech University his freshman year in college and the University of Tennessee, Martin his sophomore year. He then attended the University of Tennessee, Knoxville where he received his Bachelor of Science in Aerospace Engineering in 1991. He then pursued a Master's degree in Aerospace Engineering at the University of Tennessee Space Institute in Tullahoma, Tennessee. He received his MS degree in August, 1993.